CANADIAN THESES ON MICROFICHE

I.S.B.N.

THESES CANADIENNES SUR MICROFICHE

National Library of Canada
Collections Development Branch

Canadian Theses on
Microfiche Service

Ottawa, Canada
K1A 0N4

Bibliothèque nationale du Canada
Direction du développement des collections

Service des thèses canadiennes
sur microfiche

NOTICE

The quality of this microfiche is heavily dependent upon the quality of the original thesis submitted for microfilming. Every effort has been made to ensure the highest quality of reproduction possible.

If pages are missing, contact the university which granted the degree.

Some pages may have indistinct print especially if the original pages were typed with a poor typewriter ribbon or if the university sent us a poor photocopy.

Previously copyrighted materials (journal articles, published tests, etc.) are not filmed.

Reproduction in full or in part of this film is governed by the Canadian Copyright Act, R.S.C. 1970, c. C-30. Please read the authorization forms which accompany this thesis.

AVIS

La qualité de cette microfiche dépend grandement de la qualité de la thèse soumise au microfilmage. Nous avons tout fait pour assurer une qualité supérieure de reproduction.

S'il manque des pages, veuillez communiquer avec l'université qui a conféré le grade.

La qualité d'impression de certaines pages peut laisser à désirer, surtout si les pages originales ont été dactylographiées à l'aide d'un ruban usé ou si l'université nous a fait parvenir une photocopie de mauvaise qualité.

Les documents qui font déjà l'objet d'un droit d'auteur (articles de revue, examens publiés, etc.) ne sont pas microfilmés.

La reproduction, même partielle, de ce microfilm est soumise à la Loi canadienne sur le droit d'auteur, SRC 1970, c. C-30. Veuillez prendre connaissance des formules d'autorisation qui accompagnent cette thèse.

THIS DISSERTATION
HAS BEEN MICROFILMED
EXACTLY AS RECEIVED

LA THÈSE A ÉTÉ
MICROFILMÉE TELLE QUE
NOUS L'AVONS REÇUE

NL-339 (r. 82/08)

Canada

CRYSTALLOGRAPHY AND OPTICAL PROPERTIES OF THE $(Cu_{1-x}Ag_x)(Ga_{1-y}In_y)(Se_{1-z}Te_z)_2$ ALLOYS

by

Julie Elizabeth Avon

A thesis
presented to the University of Ottawa
in partial fulfillment of the
requirements for the degree of
Master of Science
in
Physics

Department of Physics

Faculty of Science and Engineering
University of Ottawa

STATEMENT OF ORIGINALITY

The work described in this thesis has been carried out in collaboration with Kajornyod Yoodee at the University of Ottawa. Lattice parameter and optical energy gap measurements for the copper face were made by Kajornyod Yoodee, as well as the least squares fitting of the lattice parameter and energy gap data to the nine term powers series expression. All remaining measurements and analyses were carried out by the present author.

ACKNOWLEDGEMENTS

Many thanks to Dr. O.H. Hughes for his collaboration in preparing for photoacoustic measurements.

Thanks also to Jennifer Majid, Sharon Taylor and Jennifer Callard for helping in the preparation of several of the samples; Kajornyod Yoodee for his friendship and many valuable discussions; and Mrs. Lorraine Johnston for the typing of the thesis.

Most of all, deepest appreciation to Dr. J.C. Woolley for countless hours of assistance, encouragement, and unlimited patience throughout the course of this work.

TABLE OF CONTENTS

LIST OF FIGURES

Page

CHAPTER IV

CHAPTER V

LIST OF TABLES

CHAPTER V

CHAPTER VI

CHAPTER I - INTRODUCTION

1.1 Structural Analysis

The diamond structure is one of the simplest and most symmetrical arrangements of atoms known in crystallography. Two important semiconducting elements, silicon and germanium, habitually crystallize in this structure as a result of sp^3 hybridized bonds giving tetrahedral coordination. Figure 1.1 shows a perspective drawing of the diamond structure with the tapered arrows indicating the tetrahedral bonding. The development of further semiconducting materials can be achieved by the retention of the diamond structure and the sp^3 hybridized condition. This is possible for various compounds, collectively referred to as adamantine materials, provided there is an average of four electrons per atomic site and an equal number of anions and cations (64P1). For defect structures, the latter condition requires that there be an equal number of anion and cation sites.

The first compounds developed satisfying these conditions are the well known III-V compounds. With these compounds, new properties such as a wider choice of energy gaps and band structure, and higher mobilities, became available for study and exploitation.

Many of the II-VI compounds also have the same ordered structure. Both these and the III-V compounds maintain the cubic symmetry with the cations located on one sublattice and the anions on the other (figure 1.1).

Further development of the adamantine structure was accomplished by mixing cations - for example $CdSnAs_2$ and $CuGaSe_2$ derived from III-V and II-VI compounds respectively. In both of these cases

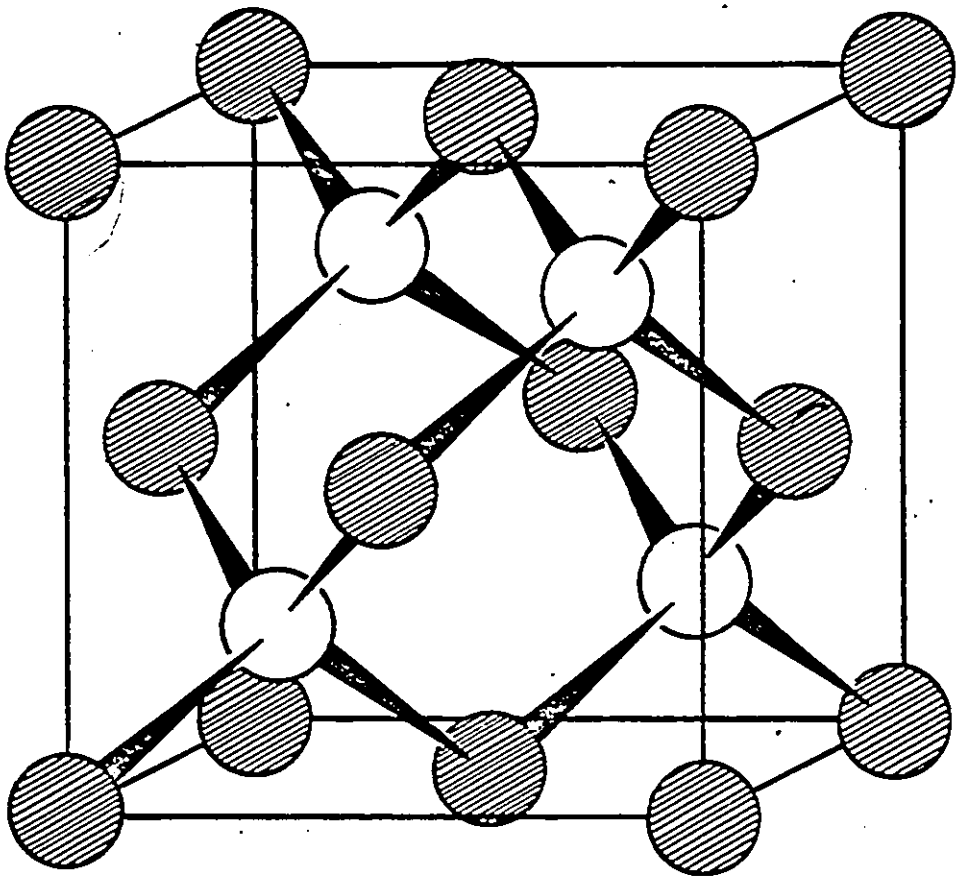

Figure 1.1 Perspective drawing of the diamond structure. Shaded atoms differentiate the two inter-penetrating sub-lattices.

the electron to atom ratio is maintained at four and there is an equal number of cations and anions. Thus the adamantine structure is also maintained. However, the two cations are now ordered giving two cation sublattices and one anion sublattice. The result of this ordering is that the structure is no longer cubic but tetragonal, with the c/a ratio equal to, or slightly less than two. This is the chalcopyrite structure and is shown in figure 1.2.

As discussed above, the development of many different adamantine compounds provides new properties, perhaps the most important being a wider range of energy gaps. At a given temperature, however, each compound has only one energy gap value and thus only a limited number of values can be obtained. In device applications, specific energy gap values are frequently required and often these are unobtainable from the compounds. This problem has been overcome by the use of alloys such as the $Ga_xIn_{1-x}As$ and $InAs_{1-y}P_y$ III-V alloys. These examples have been shown to exist over the whole composition range with single phase solid solution occurring throughout. The energy gap, therefore, varies continuously over the composition range and any energy gap within the range between the compound values can be obtained by choosing the appropriate alloy composition. Alternatively, the energy gap value can be useful in determining the composition of an alloy sample within the composition range.

In modern technological applications the variation of both the energy gap and the lattice parameters are important. As a result, alloy systems containing two variable parameters have become of interest. One such system are the $Ga_xAl_{1-x}P_yAs_{1-y}$ alloys. Alloys with two variable composition parameters allow both the energy gap and the

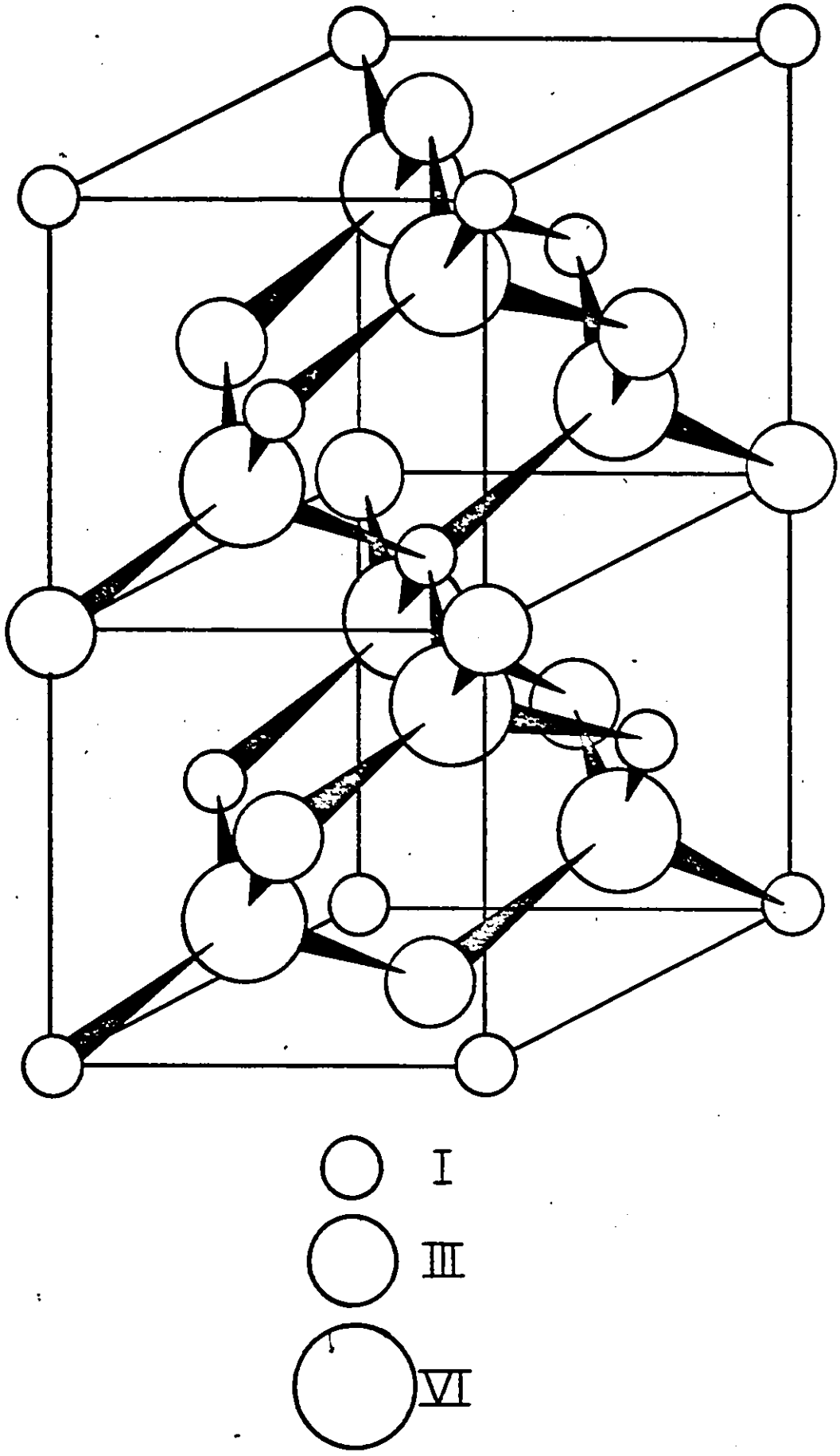

Figure 1.2 The tetragonal chalcopyrite structure illustrated for the I-III-VI_2 compounds.

lattice parameter to be chosen independently.

1.2 Applications

Considerable interest has been shown recently (75S1, 79C1, 79C2, 79P1, 80S1) in the ternary I-III-VI_2 chalcopyrite compounds and their alloys because of their possible technological applications. Promise has been shown in the areas of visible and infrared light-emitting diodes, infrared detectors, optical parametric oscillators, and far infrared generation. It has been found that two ternary compounds, $CuGaS_2$ and $CuAlS_2$, can be uniquely made p-type and have direct band gap in the visible and ultraviolet respectively. These compounds have generated activity in the area of heterojunctions with large band gap II-VI compounds, which can only be obtained n-type. Infrared light-emitting diodes have been prepared by epitaxial growth of $CdSnP_2$ on InP.

Since these ternary compounds are tetragonal, they are optically birefringent, and therefore can have applications in non-linear optics. Since these compounds are covalently bonded to a large extent, their nonlinear coefficients are large. This is a measure of their usefulness as nonlinear optical materials. More recently, the I-III-VI_2 compounds and alloys have been studied with respect to their applications in solar energy conversion.

1.3 Previous Investigations of I-III-VI_2 Alloys

The I-III-VI_2 compounds have been studied in considerable detail with lattice parameter and energy gap results quoted in standard texts (75S1 chapter 2, 79P1). Information regarding the phase relationships and lattice parameters in several mixed I-III-VI_2 alloys systems with one composition variable have been reported by Robbins

et al (73R1). Single phase solid solution was found throughout the composition range in the $Cu_{1-x}Ag_xInX_2$ selenide and sulphide systems (75S1, p. 27). However, only limited solid solubility was found for the $Cu_{1-x}Ag_xGaS_2$ and $Cu_{1-x}Ag_xGaSe_2$ systems, with miscibility gaps occurring at interior compositions. Until the present work, no alloys containing tellurium had been discussed in the literature.

Very little work has been carried out on alloys with two composition variables for these I-III-VI_2 compounds. Chapman et al (79C1, 79C2) have studied in some detail the crystallographic properties and optical energy gap values of the $(Cu_{1-x}Ag_x)In(Se_{1-z}S_z)_2$ alloys. The only other investigations in this area were made by the present author for $(Cu_{1-x}Ag_x)(In_{1-y}Ga_y)Te_2$ alloys (81A1) where lattice parameter and optical energy gap values were determined.

1.4 Description of Alloys

The present work is part of a programme being carried out at the University of Ottawa, Physics Department, to investigate the range of solid solution, and lattice parameter and energy gap values for a number of I-III-VI_2 alloys. The alloys are part of the general system $(Cu_{1-x}Ag_x)(Ga_{1-y}In_y)(Se_{1-z}Te_z)_2$. This alloy system can be conveniently represented by a cube as shown in figure 1.3, with a ternary compound located at each of the corners. Lattice parameter data on the $(Cu_{1-x}Ag_x)(Ga_{1-y}In_y)Te_2$ section, or z = 1 face, has recently been published (81A1). The present work extends the investigation throughout the entire cube, the six faces as well as many interior compositions being studied. Samples were prepared having values of x, y, and z of 0, 0.25, 0.50, 0.75 and 1.0 giving a total of 125 different alloy compositions with 98 of these being on the surface of the cube.

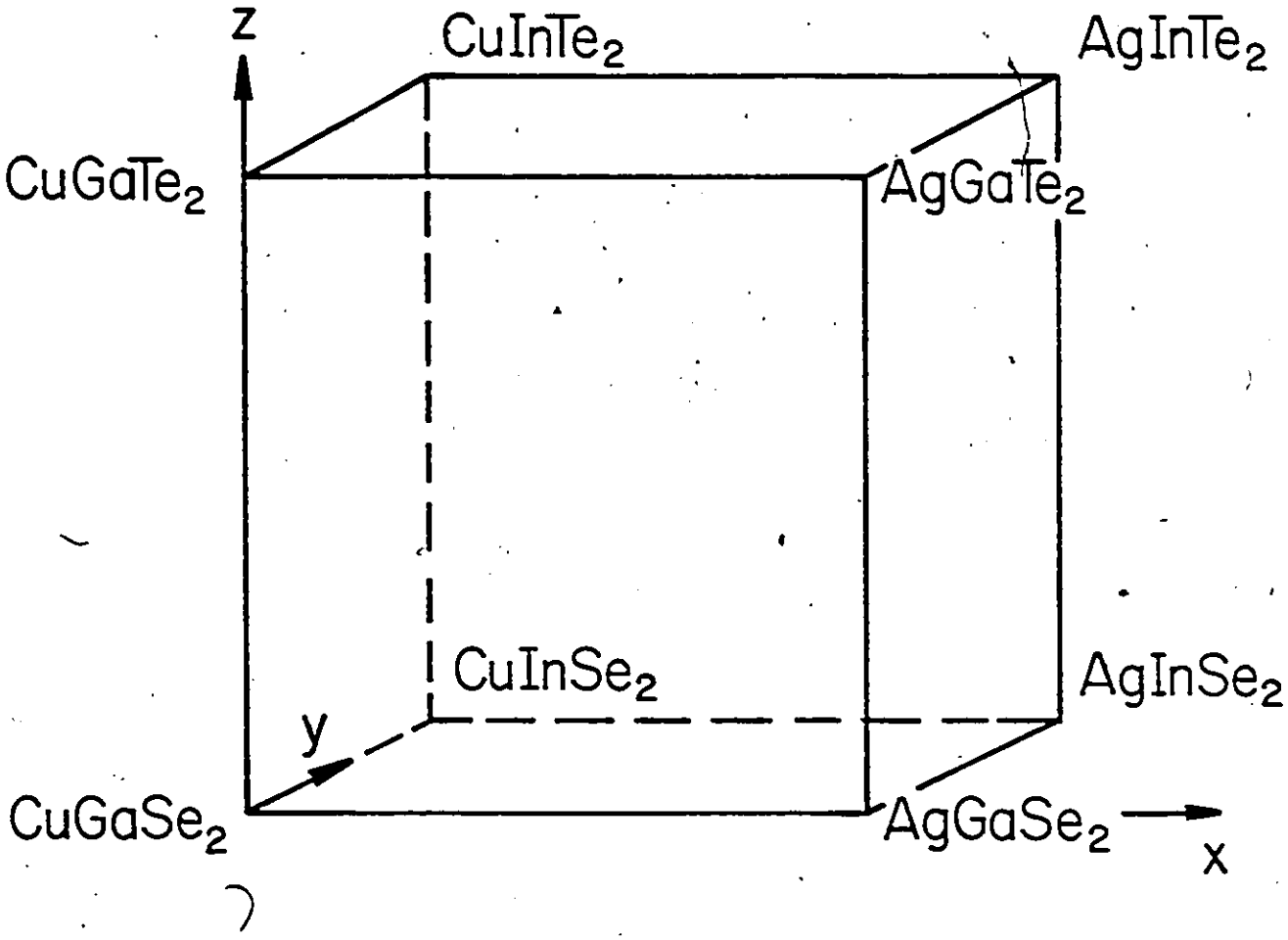

Figure 1.3 The $(Cu_{1-x}Ag_x)(Ga_{1-y}In_y)(Se_{1-z}Te_z)_2$ alloys may be conveniently represented by a cube having a ternary compound at each of the corners.

The work on the $(Cu_{1-x}Ag_x)(Ga_{1-y}In_y)(Se_{1-z}Te_z)_2$ has effectively been divided between Kajornyod Yoodee and the present author. Kajornyod Yoodee has been concerned with the crystallography and optical work on the copper face alloys ($x = 0$) and also with some of the fitting analysis. All of the other work contained in this thesis is the work of the present author.

CHAPTER II - CRYSTALLOGRAPHY AND METHODS OF PREPARATION AND GROWTH

2.1 Methods of Preparation and Growth

Polycrystalline samples of the alloy system $(Cu_{1-x}Ag_x)(Ga_{1-y}In_y)(Se_{1-z}Te_z)_2$ were prepared from the elements by the standard melt and anneal technique. The components of 1 gram samples were sealed in small segments of quartz tubing under vacuum. Care was taken to minimize the length of the sealed tube in order to eliminate losses up the sides of the tube. During all preparations, careful procedures were followed to ensure that the final alloy composition was in accordance with the initially measured quantity of elements. The samples were placed in a melting furnace at room temperature and heated to 1100°C at an average rate of about 350°C per hour. This temperature was maintained for an hour, during which time the tubes were shaken periodically in order to obtain a thorough mixing of the elements. Cooling to room temperature proceeded for approximately 5 hours. This rate was sufficiently slow to avoid breakage of the quartz upon solidification of the alloys. The samples were then placed in a furnace to anneal at temperatures in the range of 600-800°C. The choice of the annealing temperatures was guided by the melting point values of the ternary compounds (75S1, p. 12).

Debye-Scherrer x-ray powder photographs (see section 2.2) were taken using small pieces of alloy to check for homogenenity, the criterion being resolution of the $K\alpha_1$, $K\alpha_2$ doublet. Preliminary photographs indicated that annealing times of 2-3 months were necessary for reasonable equilibrium conditions to be obtained. In some cases, however, samples annealed for up to 5 months before reaching equilibrium.

2.2 Crystallography

Debye-Scherrer x-ray powder photographs were obtained for each of the alloys using 114.6mm diameter cameras and CuKα radiation. Each specimen was ground into a smooth, fine powder and mounted in the camera by means of a spindle and thin glass fibre arrangement (see figure 2.1). The fibre was coated with powder using, as an adhesive, a grease known to give little absorption. Care was taken to keep the fibre and powder in cylindrical form in order to minimize unsystematic absorption corrections (see below). Two typical x-ray photographs obtained in this manner are shown in figure 2.4. The position of the diffraction lines were measured using a travelling microscope and, after allowing for absorption effects, the Bragg angle of each line was calculated. The absorption effects mentioned above result from the specimen having finite width and high absorption so that scattering is obtained from a limited region of sample. In figure 2.2(a) the effect of absorption will be greater in the centre of the specimen compared to the edges, since the incident rays have travelled a greater distance within the sample. The resulting intensity distribution across the powder line is shown in figure 2.2(b). For low Bragg angles this has the affect of doubling the diffraction lines. As θ increases, however, the weaker component becomes smaller and disappears, resulting in diffraction lines being shifted to higher angle positions.

In some cases, when absorption is high, only part of the specimen is irradiated. This is shown in figure 2.2(c) where x-rays have penetrated throughout the shaded region only. Again, the effect is to double the diffraction lines for low θ and shift to higher positions for high θ. However, in both cases, it should be noted that

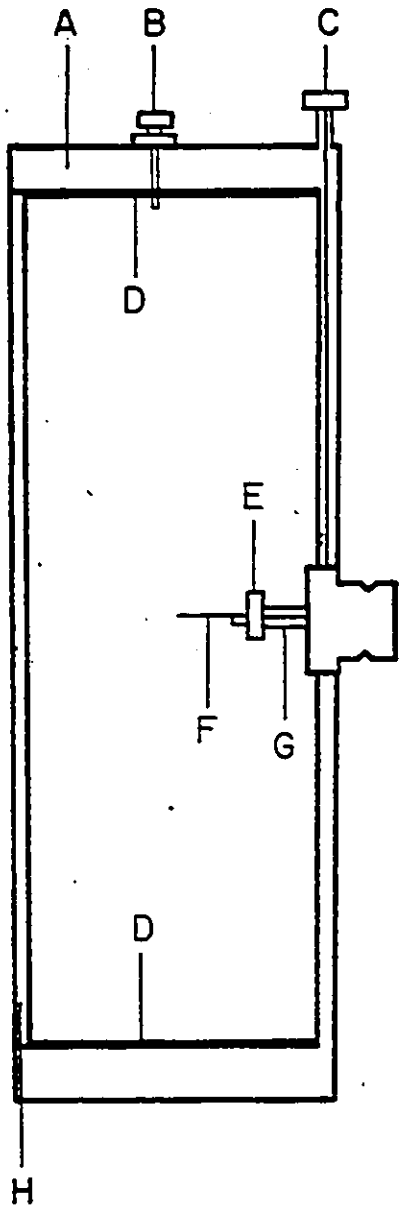

Figure 2.1 The powder camera and spindle-fibre arrangement used to take Debye-Scherrer x-ray photographs. The camera is shown in actual size with a radius of 114.6mm. The part labelled A is the cylindrical camera body, B, are movable pins with a locking screw to hold the film in position, C, is a plugger to centre the specimen holder, E, in the x-ray beam. F is the fibre onto which the specimen is adhered, G, a drive spindle from a detachable motor, H a detachable lid, and D the film.

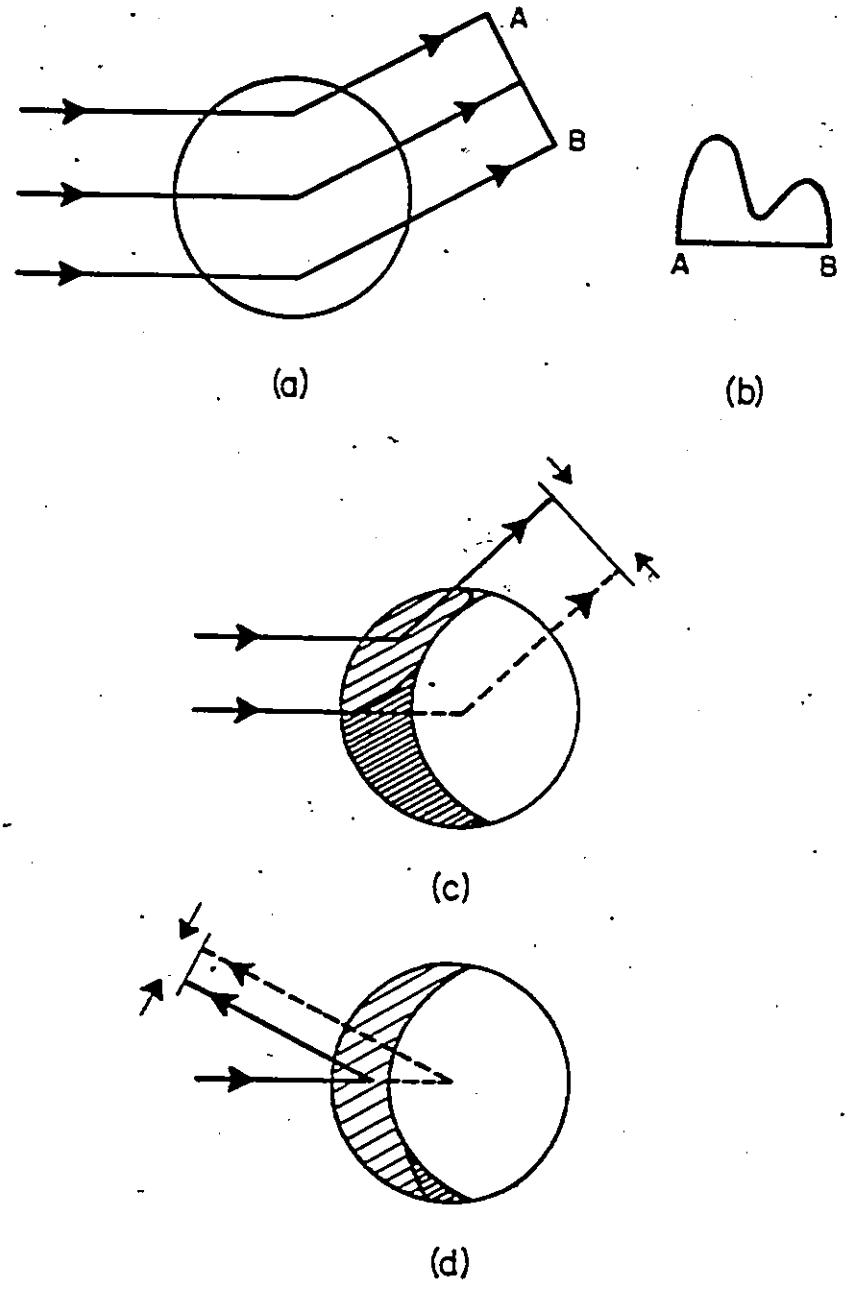

Figure 2.2 The effect of absorption in an x-ray specimen. An x-ray beam is diffracted as it passes through the specimen (a). The resulting intensity distribution is shown in (b). The diffraction line appears to be doubled. If absorption is high only part of the sample is irradiated. This region is shown by the shaded areas in (c) and (d). X-rays in the darkly shaded areas are absorbed within the sample after being diffracted. The effect of high absorption is to shift the diffraction line to a higher angle. The shift is greater for lower Bragg angles (c) and decreases as θ approaches 90° (d).

this shifting of lines occurs to a lesser extent at θ increases (figure 2.2(d)), until in the limiting case of $\theta = 90^{\circ}$, no shift occurs at all.

Two methods were used to correct for absorption effects, these being the Nelson-Riley extrapolation (45N1), and internal calibration techniques. In the tetragonal case, which is the only case considered in this work, the Nelson-Riley technique becomes a method of continuous approximation whereby the a and c parameters are plotted against an error function and adjusted until the resulting lines are parallel. Although this method was used to determine a and c parameters for the tellurium face, it proved too tedious and was dropped in favour of the internal calibration method for all of the remaining compositions.

The internal calibration method involves intimately mixing an internal standard of accurately known lattice parameter, with the sample being x-rayed. If the correct values of Bragg angle are known and the effects of absorption in the calibration material are determined from these, a correction curve may be plotted showing the change in the Bragg angle θ, due to absorption as a function of θ, or more conveniently, changes in $\sin^2\theta$ as a function of $\sin^2\theta$. A typical correction curve is shown in figure 2.3. Deviations from this general form will occur if the sample is not circular in cross section.

2.3 Analysis of Results

Analysis of the x-ray photographs was approached by directly relating the chalcopyrite structure of the alloys to the well understood, cubic zinc blende structure. As can be seen from figures 1.1 and 1.2, the same atomic sites are occupied in both structures, but due to ordering, c is doubled in the chalcopyrite case. This in turn doubles

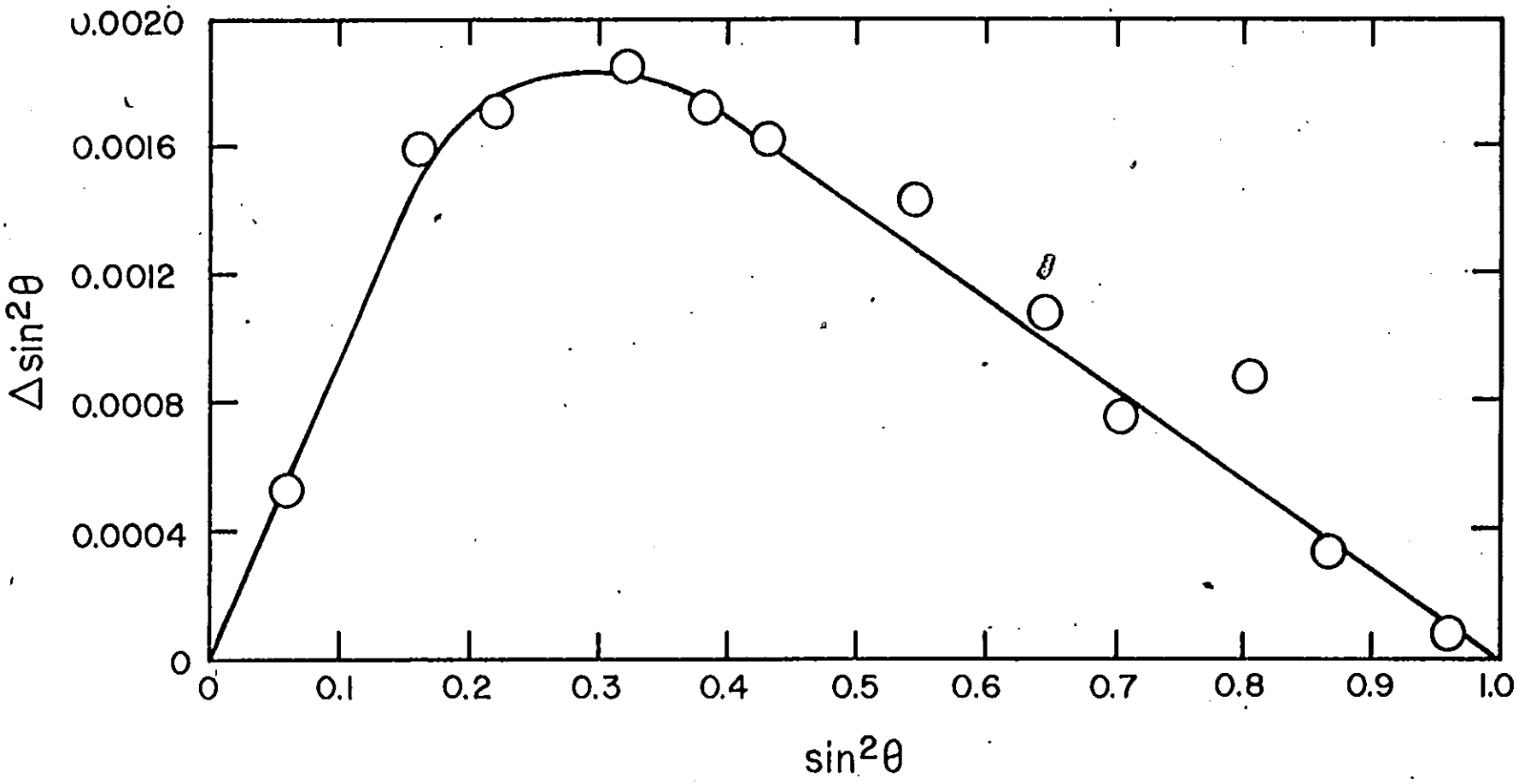

Figure 2.3 A typical silicon correction curve showing the change in $\sin^2\theta$, where θ is the Bragg angle, as a function of $\sin\theta$. The change in $\sin^2\theta$, ($\Delta\sin^2\theta$), results from absorption of x-rays in the specimen.

the Miller index ℓ and the Bragg condition is no longer given by

$$\sin^2\theta = \frac{\lambda^2}{4}\left(\frac{h^2 + k^2 + \ell^2}{a^2}\right) \qquad (2.1)$$

as in the case of zinc blende, but by

$$\sin^2\theta = \frac{\lambda^2}{4}\left(\frac{h^2 + k^2}{a^2} + \frac{\ell^2}{c^2}\right) \qquad (2.2)$$

for the tetragonal lattice. Furthermore, since the same atomic sites are occupied in both structures, all zinc blende diffraction lines must occur in the chalcopyrite diffraction pattern. In addition, it is known that because zinc blende is face centred cubic only reflections satisfying the conditions

$$\begin{aligned} h + k + \ell &= 4n \\ h + k + \ell &= 4n + 2 \\ h + k + \ell &= 2n + 1; \quad n : \text{integer} \end{aligned} \qquad (2.3)$$

will occur. These conditions give strong lines for $N = h^2 + k^2 + \ell^2 = 3$, 8, 11, 16, 19, 24 etc. and weak lines for N = 4, 12, 20, etc. Thus these reflections will also occur in the chalcopyrite case, with $\ell_{\text{chalco.}} = 2\ell_{\text{zinc blende}}$. Possible combinations of the values of h, k, and ℓ are listed in table 2.1 for zinc blende and the chalcopyrite alloys. Consider now, for example, reflections for which N = 8. Providing c = 2a the 220 and 204 diffraction lines will occur at exactly the same angle, θ. However, due to compression of the lattice,

N	hkℓ	
	zinc blende	chalcopyrite
3	111	112
4	200	200 004
8	220	220 204
11	311	312 116
12	222	224
16	400	400 008
19	331	332 316
20	420	420 404 208
24	422	424 228
27	511 333	512 336 1110
32	440	440 408
35	531	532 516 3110
36	600	600 0012
40	620	620 604 2012
43	533	536 3310
44	622	624 2212
48	444	448
51	551 711	552 712 5110 1114
56	642	644 628 4212
59	553 731	732 556 716 5310 3114

Table 2.1 Possible combinations of h, k, ℓ for zinc blende and chalcopyrite alloys.

this is not always the case, and in most cases c will be less than 2a. Under such conditions, in the present example, the 220 and 204 lines will split showing two diffraction lines rather than only one in the case c = 2a. Figure 2.4(a) shows an indexed x-ray photograph of an alloy internally calibrated with silicon. This alloy (251000) has c = 2a. The material used for the photograph in figure 2.4(b) has c < 2a. (The Nelson-Riley extrapolation technique was used in this case, i.e. no silicon, see section 2.2). In addition to the lines expected from the zinc blende analysis, extra lines due to the ordering of the cations occur but at much lower intensity. These were not needed for the present analysis of determining a and c and so were not included. The ordering lines are important if it is necessary to show that c = 2a, but this is clearly known from previous results in the literature for the cases of ternary compounds.

Once the effects of absorption were determined and the Bragg angle correspondingly adjusted, $\sin^2\theta$ was calculated and the Miller indices of the diffraction lines were determined. The indexing of the lines was clear for low angle reflections and thus using these lines only, a and c were calculated using a least squares fit (see appendix) to equation (2.4),

$$\sin^2\theta = \frac{\lambda^2}{4}\left(\frac{h^2 + k^2}{a^2} + \frac{\ell^2}{c^2}\right). \qquad (2.4)$$

The values of a and c determined in this manner were then used to establish the indices of the higher angle reflections. Once all diffraction lines were indexed, a and c in equation (2.4) were recalculated using all of the diffraction lines. As a final check, values

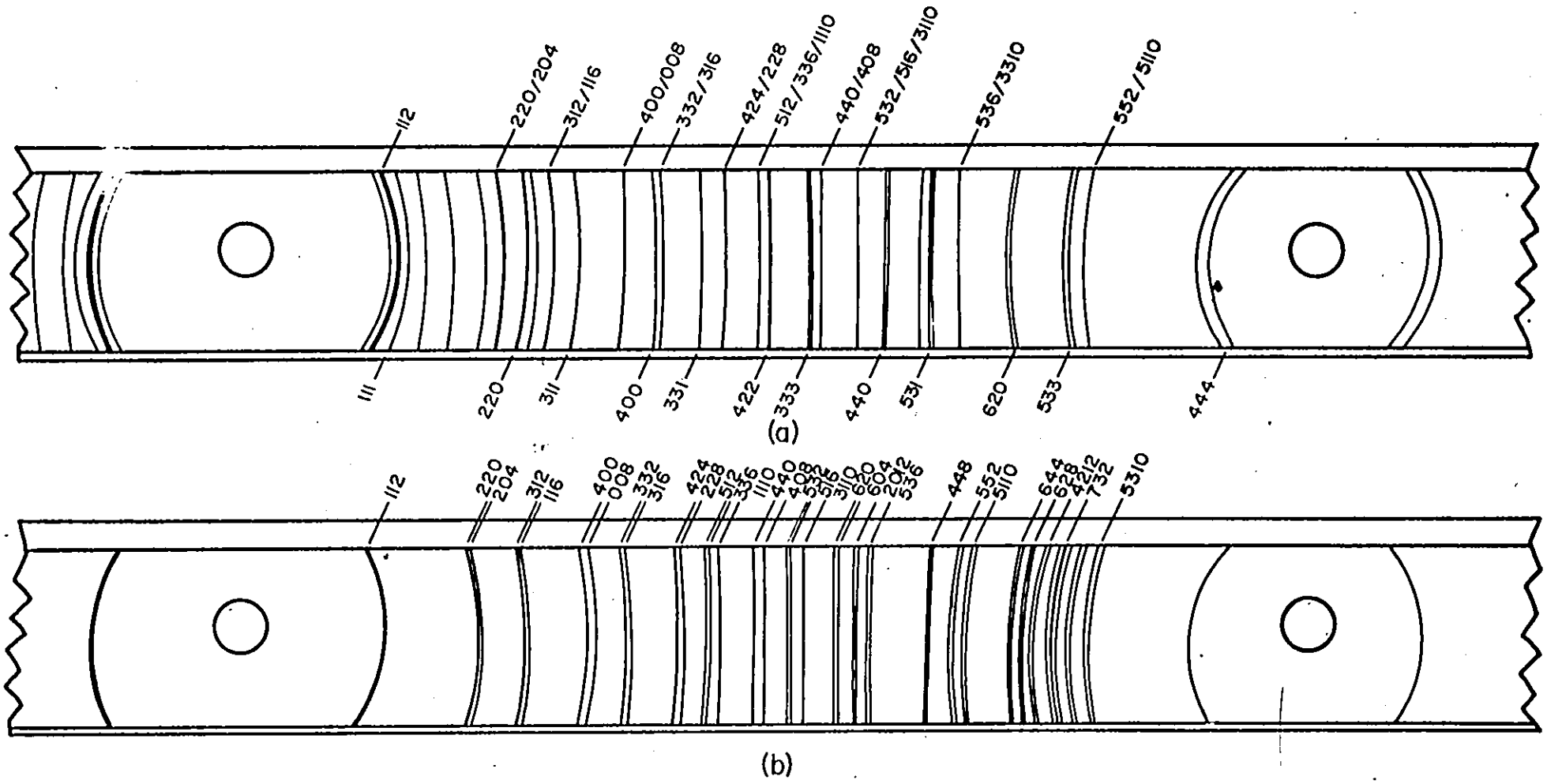

Figure 2.4 (a) X-ray photograph of $(Cu_{0.75}Ag_{0.25})InSe_2$. The sample has $\frac{c}{a} \approx 2.0$ and has been internally calibrated with silicon. Si diffraction lines are indexed at the bottom of the film. Ordering lines are present. (b) X-ray photograph of $Ag(Ga_{0.25}In_{0.75})Te_2$ with $\frac{c}{a} < 2$. The $K\alpha_1$ and $K\alpha_2$ doublets are clearly split at high angles.

of $\sin^2\theta$ were recalculated using the determined values of a and c and compared to the measured a and c values to establish the accuracy. Typically the values of $\sin^2\theta$ agreed within ± 0.0007 nm or better.

CHAPTER III - OPTICAL MEASUREMENTS

A - OPTICAL ABSORPTION

3.1 Introduction

One of the most common techniques for studying optical properties of semiconductors is that of absorption spectroscopy. Optical absorption can be used to measure a number of parameters characteristic of semiconductors, not the least of which is the fundamental energy gap E_g. The fundamental energy gap of a material involves a transition from the highest valence band to the lowest conduction band. This transition is either of a direct or indirect nature. Since it is known from the literature that the transition is direct in the case of the compounds involved in the present alloy system, ($AgInTe_2$, $CuInTe_2$, etc.), it was expected that the transition is also direct in the case of the alloys. This was in fact found to be the case as will be discussed later in Chapter V.

3.2 Theory of Optical Absorption

The fundamental energy gap, E_g, may be determined from absorption measurements by observing the change in absorption of the material as a function of the energy of radiation incident at its surface. As this incident energy reaches a threshold corresponding to the band gap energy, interband absorption occurs whereby photons excite electrons from the valence band to the conduction band. The result is the observation of an absorption edge in the absorption spectrum corresponding to a sharp rise in the value of the absorption coefficient above the background.

Consider a beam of light of intensity I_0 incident normally on the surface of a sample of thickness d. If a portion I_R is reflected and a portion I_T is transmitted, and if interference effects are ignored, then from standard electromagnetic theory it can be shown that the transmitted intensity is given by

$$I_T = \frac{I_0 (1- R)^2 (1 + k^2/n^2) \exp (-\alpha d)}{1 - R^2 \exp (-2\alpha d)} \qquad (3.1)$$

where R is the reflection coefficient, α is the absorption coefficient, and n and k are the refractive index and the extinction coefficient of the material respectively. An interference term in the denominator of equation (3.1) will arise when α is small enough to allow multiple traverses of the material by the incident radiation. However as aforementioned, interference effects were ignored owing to the thicknesses of the samples used in the present work (see below) and equation (3.1) was considered in this simpler form. Equation (3.1) may be simplified further if d is large enough to ensure that $R^2 e^{-2\alpha d}$ is much less than unity and if k is much less than n. The latter condition is true of energies near the absorption edge so that, to a good approximation, equation (3.1) may be written as

$$I_T = I_0 (1 - R^2) \exp (-\alpha d) \qquad (3.2)$$

In addition, R is a slow varying function of photon energy and varies very little in the wavelength range concerned. Thus the $(1 - R^2)$ term may be treated as a constant to a good approximation, and hence by taking the natural log of both sides of (3.2),

$$\ell n \left(\frac{I_0}{I_T}\right) = \alpha d - \text{constant} . \qquad (3.3)$$

Thus the reflected portion of the incident beam need not be considered since calculations of α from the $\frac{I_0}{I_T}$ ratio will give values which are too large by a constant amount for a given sample. However, it is well known that other effects such as absorption by impurities and scattering due to impurities and free carriers will contribute to the measured value of α, and thus must be accounted for in the background value of a sample. In the case of scattering by free carriers or impurities, contributions to α can take the form

$$\alpha = \alpha_o (h\nu)^{-m} , \qquad (3.4)$$

the scattering effect increases as the photon energy is decreased (82G1). Thus this effect, if present, can easily be observed at energies below the absorption edge, and must be considered when calculating E_g from the absorption spectrum.

The theory of interband optical absorption (67J1) shows that at the absorption edge the absorption coefficient, α, varies with the photon energy, $h\nu$, as

$$\alpha h\nu = A (h\nu - E_g)^n \qquad (3.5)$$

where A is a constant and n is a number which characterizes the transition process, taking a value of $\frac{1}{2}$ for direct allowed transitions, $\frac{3}{2}$ for direct forbidden, 2 for indirect allowed, and 3 for indirect forbidden transitions. The method used to determine the value of E_g

involved plotting a graph of $(\alpha h\nu)^{\frac{1}{n}}$ against $h\nu$. Since it is known from literature that the transition is direct in the case of the compounds involved in the present alloy system, n was initially chosen as $\frac{1}{2}$ and the graphs were plotted. These graphs yielded straight lines indicating that the appropriate value of n had been used. The value of E_g was then given by the intercept on the $h\nu$ axis. Typical curves showing the variation of $\frac{1}{d} \ell n \frac{I_0}{T}$ with photon energy $h\nu$ are shown in figures 5.3(a) and 5.4(a) (Chapter V) and the corresponding variation of $(\alpha h\nu)^2$ vs $h\nu$ are shown in figures 5.3(b) and 5.4(b) (Chapter V). Figure 5.4(a) shows that at low energies, scattering effects are observed with $\frac{1}{d} \ell n (\frac{I_0}{I_T})$ increasing as $h\nu$ decreases. In this range, the experimental values of $\frac{1}{d} \ell n (\frac{I_0}{I_T})$ can be fitted to an expression of the form of equation (3.4). Values extrapolated from this can then be subtracted from the experimental data at the absorption edge to obtain values of α due to interband transitions. In figure 5.3(a), however, scattering effects are negligible and the background absorption considerably smaller than in figure 5.4(a). In this case a straight line extrapolation of the background absorption region can be subtracted from the measured value of $\frac{1}{d} \ell n (\frac{I_0}{I_T})$ to give the required values of α in both cases, the resulting graphs of $(\alpha h\nu)^2$ vs $h\nu$ should give good straight lines. The treatment of background absorption will be discussed further in section 5.1 with the presentation of experimental results.

3.3 Preparation of Samples

All samples were sliced into thin discs of thicknesses between 0.5mm and 1.0mm using a tungsten wire saw and a mixture of oil and silicon carbide grit (320 mesh size) as the cutting slurry,

or a mechanical cutting machine using a 4" diameter carborundum cutting blade. The slices were reduced in thickness as much as possible by lapping on a glass plate covered with a slurry of methanol and alumina powder of varying mesh size. The mesh size was decreased to 1μm as the sample became thin, and in most cases, very fragile. This occurred when the lapped discs were typically 200μm in thickness. However, with some more robust samples, it was possible to obtain thicknesses as little as 90μm.

The decision to lap with methanol as opposed to water was made for two reasons. Firstly, methanol evaporates rapidly and completely from the slices. Water, alternatively, would have to be removed before any transmission measurements were made, entailing further handling of the fragile discs and risking damage. Secondly, this avoided any possibility of the alloys reacting with water. However, samples that were polished with water showed no signs of reaction.

The method of lapping was used for the initial group of samples prepared for absorption measurements (Te, In faces). However it was found that thinner slices could be obtained with less risk of breakage using a polishing machine. With this method it was possible to achieve thicknesses of about 50μm in most cases. Here, the coarsely cut discs were mounted at the end of a brass rod using molten paraffin wax. The rod was then placed on end, with the sample in contact with a rapidly rotating polishing disc (figure 3.1). A slurry of water and 1μm mesh alumina powder was used as the polishing agent and was continually replenished on top of the rotating disc. After the sample had polished for a time on one side, being conti-

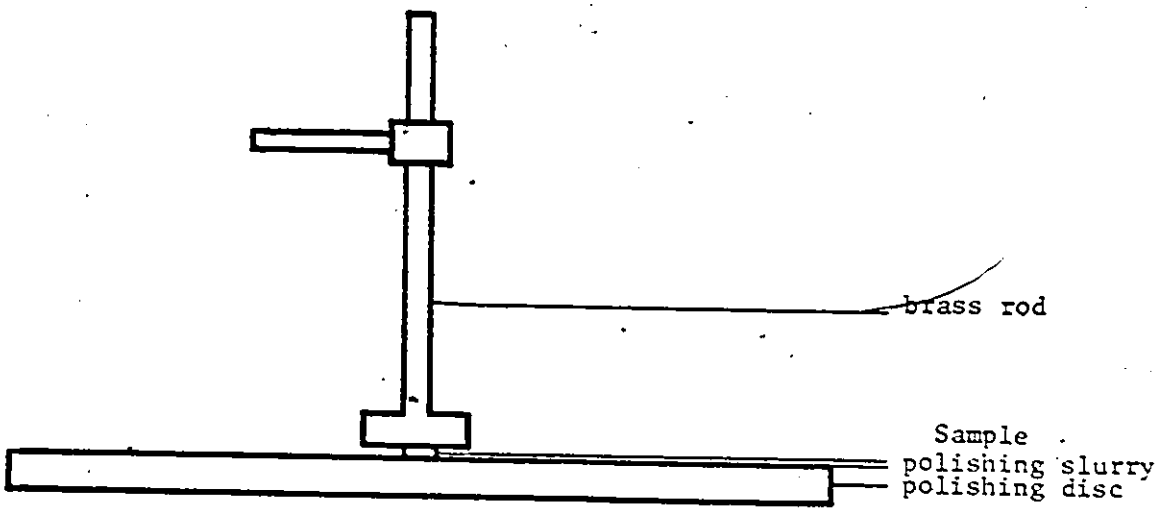

Figure 3.1 Schematic diagram illustrating the polishing equipment used to prepare samples for optical absorption.

nually rotated to achieve a smooth, uniform surface, the sample was removed and remounted so that its other side could also be polished. This was done by heating the brass rod in a Bunsen flame until the wax melted and the sample easily slid off. When the sample had reached the desired thickness, the brass rod was placed in a beaker of boiling acetone to remove the sample from the rod and all wax from the sample. This was done with great care so that the sample would not break, although several times such was the case and the procedure had to be repeated. The advantage of obtaining thinner slices, however, far outweighed any disadvantages of the method and, as a result, this procedure was used for all of the remaining samples.

Whether the samples were polished by lapping or using the polishing machine, the next step was to mount the samples on small tin plate slides. The centres of these slides were drilled out to as large an aperture as could be covered by the prepared slice. The sample was affixed to the slide by a small amount of silver print (G.C. electronics cat. no. 21-1) applied to the edge of the aperture. The silver print was allowed to thicken slightly to ensure that the solvent (n - Butyl acetate) did not penetrate into the slice and also that the fluid did not flow on to the slice. The slide and sample were next placed in front of an intense light in order to detect the presence of any small pinholes in the sample. If present, these were plugged with small droplets of the opaque silver print. At this point the sample was prepared for mounting on an appropriate detector and for transmission measurements to be made.

3.4 Experimental Details

The transmission measurements were made using the experimental arrangement depicted in figure 3.2. The light source used was a 30W tungsten filament light bulb. The light beam from this source was collected by mirror, and focussed on the entrance slit of a Czerner-Turner scanning spectrometer. Here the light was chopped at about 175Hz. The monochromatic light from the exit slit was refocussed onto the sample and the transmitted portion detected using a PbS cell biased at 67.5 volts. The square wave output signal of the detector was sent to a PAR-219 lock-in amplifier through a PAR-213 pre-amplifier. The wavelength of the incident light was continuously varied and the output from the lock-in traced on a roll-off chart recorder. Since the monochromator output and the sensitivity of the detector varied considerably over the wavelength range, a reference spectrum was made by removing the sample and observing the signal directly from the monochromator. The signal variation obtained in this manner was taken as I_0.

B - PHOTOACOUSTIC DETERMINATION OF ENERGY GAPS

3.5 Introduction

Although optical spectroscopy has proven to be important in determining optical properties of semiconductors, there are, however, several instances where conventional transmission spectroscopy is inadequate. Such a situation, for example, arises when attempting to measure very weak or very strong absorption, or when samples are only available in powder form. The first situation involves the measurement of a very small change in the intensity of a strong

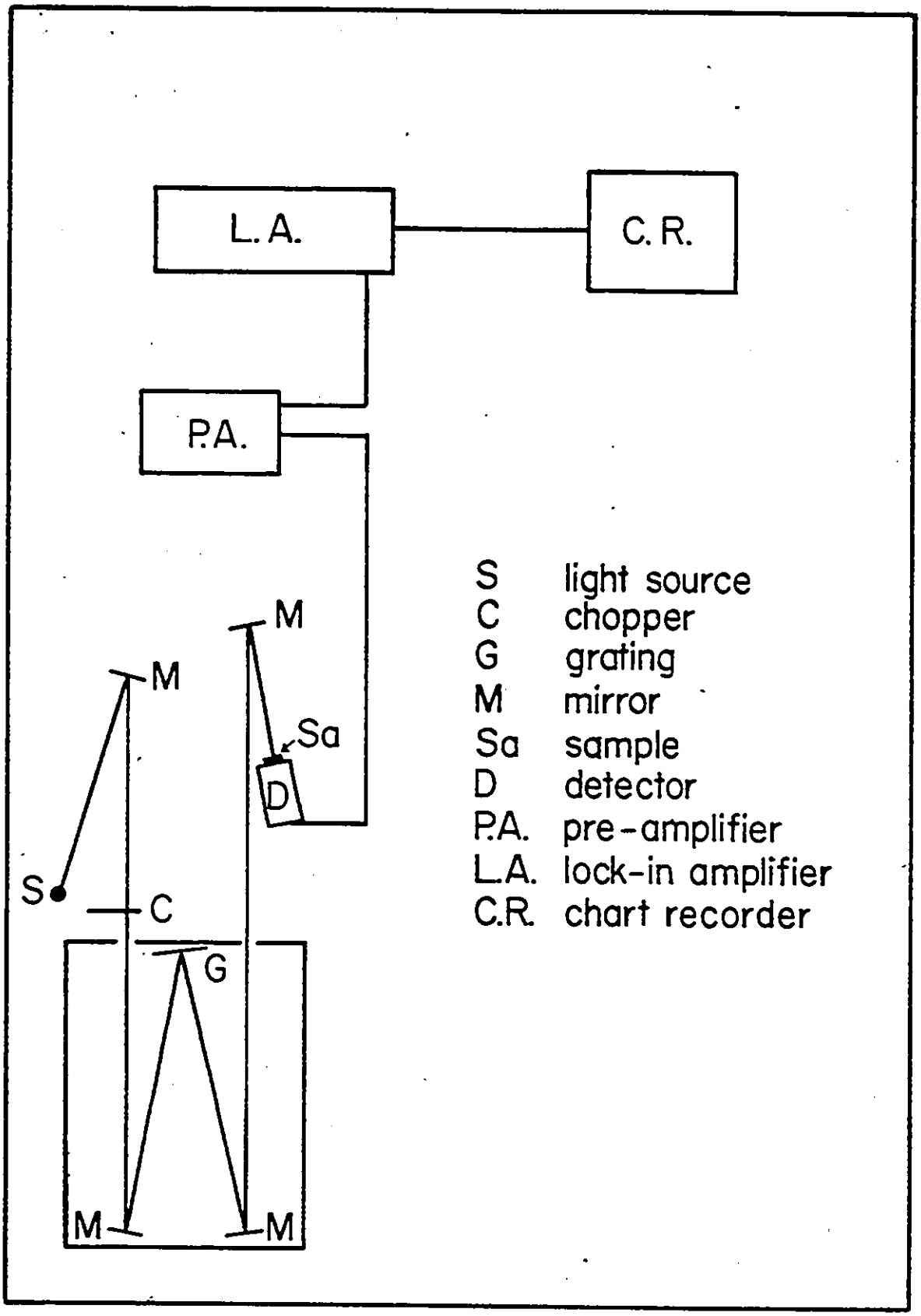

Figure 3.2 Block diagram of optical absorp . . . perimental arrangement.

transmitted signal or the inability to detect the transmitted signal at all. Transmission measurements, as discussed in section 3.3, also require that a very thin slice of the material under investigation be available. This is, in some cases, very difficult to obtain for several reasons. Firstly, many samples are characterized by large voids throughout the ingot so that even coarse slicing is difficult. In other cases, samples may crumble when polishing before reaching a thickness suitable for transmission measurements. Others, still, may crumble upon solidification excluding any attempts whatsoever for absorption measurements.

To overcome these difficulties, another optical technique has recently been developed to study materials that are unsuitable for conventional transmission or reflection investigations. This technique, referred to as photoacoustic spectroscopy or PAS, involves a direct measurement of the incident energy absorbed by some material as a result of its interaction with the photon beam.

In photoacoustic spectroscopy, the sample to be studied is enclosed in a cell or chamber and is illuminated with monochromatic light, intensity modulated by an electromechanical chopper. Since the incident radiation is intensity modulated, the internal heating due to absorption in the sample is also modulated. This periodic heating results in a periodic heat flow from the sample to a non-absorption gas in the cell, and, in turn, produces pressure and volume changes in the gas which can be detected using a microphone. The amplitude of the acoustic signal depends upon the amount of optical power absorbed by the sample.

The first attempt at a modern quantitative theory describing

the photoacoustic effect in solids was made in 1973 by J.G. Parker (73P3). In 1975, a more general theory was formulated by A. Rosencwaig and A. Gersho (80R1, Chapter 9) for the photoacoustic effect in condensed media (RG theory). Bennett and Forman (76B1), Aamodt et al (77A1), and Fretsel and McDonald (77W1, 77W2) refined the theory by treating the transport of the acoustic disturbance in the gas more exactly, and by including contributions to the signal from thermally-induced vibrations in the sample.

The RG theory is a one-dimensional analysis of the production of a photoacoustic signal in a simple cylindrical cell of length L (see figure 3.3). The sample is considered to be in the form of a disc of thickness, ℓ, mounted against a poor thermal conductor of thickness ℓ''. The length of the gas column in the cell is $\ell' = L - \ell - \ell''$. The RG theory further assumes that the gas and backing material are not light absorbing. The light source, of wavelength λ, is chopped sinusoidally at a frequency ω and the incident intensity on the solid is I_0. This incident radiation is absorbed in the sample to an extent determined by the absorption coefficient, α. As a result, the surface layers of the sample are heated periodically, and re-emission from the sample periodically heats adjacent layers of the gas in the cell.

As mentioned in the introduction, the RG theory contends that this heating is the main source of the acoustic signal. Because of the rapid damping of the temperature fluctuations away from the sample, only a limited boundary layer of the gas shows a periodic temperature variation. The effective thickness of this layer is $2\pi\mu'$, where μ' is the thermal diffusion length in the gas. The periodic heating causes the boundary layer to expand and contract periodically and thus act as

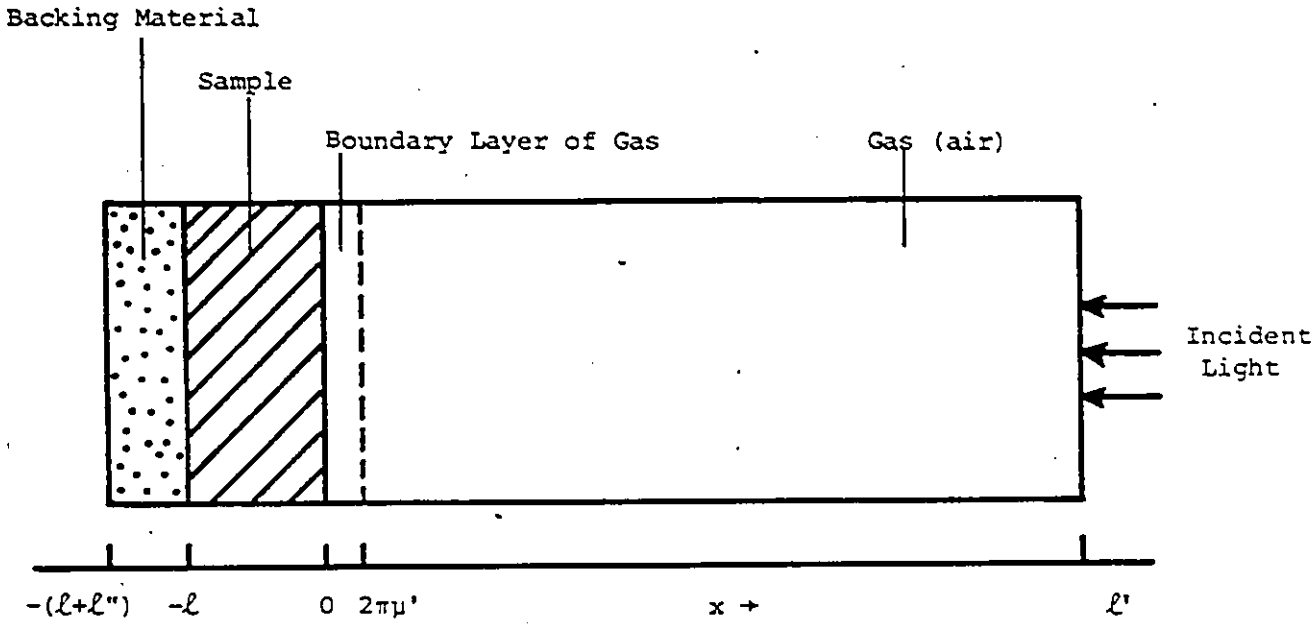

Figure 3.3 Cross-sectional view of a simple cylindrical photoacoustic cell.

an acoustic piston on the rest of the gas column. This produces an acoustic pressure signal that travels throughout the entire gas column.

By analysis of this effect in terms of standard gas laws, a complex expression, Q, can be developed, the real part of which gives the actual pressure variation. In general, this expression is very complicated, but several special cases exist where physical insight may be obtained from relatively simple expressions for Q. These cases may be grouped into two categories, defined by the optical opaqueness or transparency of the solids concerned.

Optically transparent samples have light absorbed throughout the length of the sample and some light transmitted. In this case, the optical path length, ℓ_α, defined as

$$\ell_\alpha = \frac{1}{\alpha} , \tag{3.7}$$

is larger than the length of the solid, i.e. $\ell_\alpha > \ell$. Although several cases may be encountered in this category, they are unimportant in the present work, and will thus not be further considered.

Optically opaque solids have most of the light absorbed within a distance that is small compared to the length of the sample, and essentially no light is transmitted, i.e. $\ell_\alpha << \ell$. Three cases may now be considered which are defined according to the relative magnitude of the thermal diffusion length μ, as compared to ℓ and ℓ_α.

Case A: Thermally Thin Solids – $\mu >> \ell$ and $\mu >> \ell_\alpha$

In this case the expression for Q simplifies to

$$Q \approx \frac{(1 - i)}{2a'} \left(\frac{\mu''}{K}\right) Y \tag{3.8}$$

where K represents thermal conductivity, a is the thermal diffusion coefficient, and Y is a parameter depending on the ambient temperature and pressure, etc., and is proportional to the incident light intensity, I_0. The primed and double primed notation represents parameters characteristic of the gas and backing respectively.

In this case Q is independent of α. This condition would be met for a very black absorber such as carbon black

Case B: Thermally Thick Solids - $\mu < \ell$ and $\mu > \ell_\alpha$

Under these conditions

$$Q = \frac{(1 - i)}{2a'} \left(\frac{\mu}{K}\right) Y. \tag{3.9}$$

This expression for Q is similar to (3.8) in that the acoustic signal is again independent of α, and the thermal parameters of the backing are now replaced by those of the solid.

Case C: Thermally Thick Solids - $\mu << \ell$ and $\mu << \ell_\alpha$

In this case

$$Q = \frac{i\alpha\mu}{2a'} \left(\frac{\mu}{K}\right) Y. \tag{3.10}$$

This is a very interesting and important case in that the photoacoustic signal is porportional to α. Only the light within the first thermal diffusion length, μ, contributes to the acoustic signal since $\mu < \ell_\alpha$.

3.6 Experimental Application of the RG Theory for Determining Energy Gaps

For semiconductors, both direct and indirect band transitions

can be observed from the photoacoustic signal, and thus energy gap values can be determined. Figure 3.4 shows the PA spectrum for three direct-band semiconductors, all in the form of powders. The band gaps derived from these spectra are also indicated in figure 3.4. To understand the nature of the signal variation, both the RG theory and the dependence of the absorption coefficient, α, on the energy of the incident radiation are needed.

Returning to the RG theory and Cases A and B, it is important to note that the only parameter in equations (3.8) and (3.9) that is dependent upon the wavelength of the incident radiation is the light source intensity, I_0. Thus it is clear that the photoacoustic spectrum of a photoacoustically opaque sample ($\mu > \ell_\alpha$), such as carbon black, is simply the power spectrum of the light source. With Case C however, the PA signal is also dependent upon α, which, in turn, is dependent upon the incident wavelength of radiation. Now it is known, and discussed in section 3.2, that the general form of the absorption coefficient, α, plotted against the incident energy of radiation, $h\nu$, is similar to the curves illustrated in figures 5.3(a) and 5.4(a) (Chapter V). At small wavelengths or high energies, α is large, and $\mu > \ell_\alpha$. Thus condition B is satisfied. At larger wavelengths or lower energies, α is small, $\mu < \ell_\alpha$, and condition C is satisfied. Thus, as the wavelength of the incident radiation increases, the PA signal from the sample changes from one which is independent of α to one which depends on α. At small wavelengths then, the PA signal from the sample is the same as that of carbon black, since both are independent of α. As the wavelength is increased, the signal from the sample decreases in comparison to the carbon black signal. Thus, if

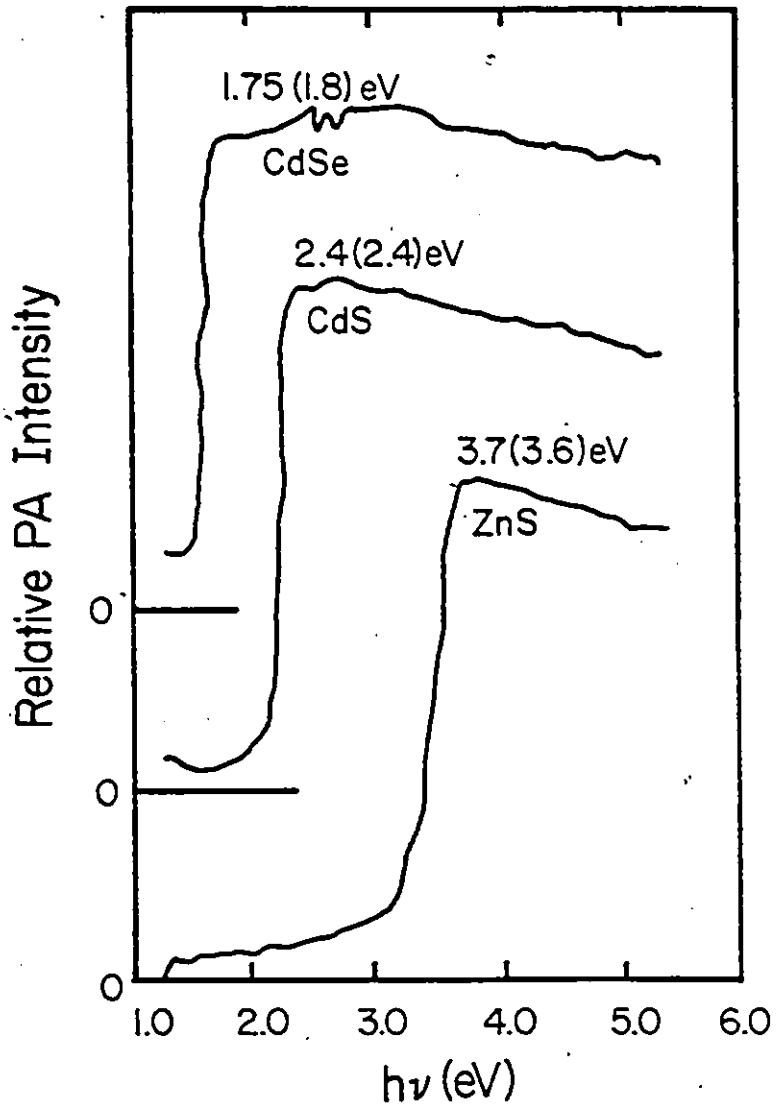

Figure 3.4 Photoacoustic spectra of three direct-band semiconductors. For each compound, the energy gap was taken as the energy, $h\nu$, corresponding to the value for which the PA spectra peaked. These PA energy gap values can be compared to the standard values obtained using other techniques (values in brackets).

the ratio of intensities of the sample and carbon black signals is plotted as a function of hν, curves similar to those of figure 3.4 are obtained.

No satisfactory single criterion for determining the band gap values from the photoacoustic spectra such as those in figure 3.4 is presently available. For CdSe, CdS, and ZnS (figure 3.4), the energy corresponding to the peak value of the relative photoacoustic signals is in close agreement with the value obtained from literature. With the present system of alloys, energy gap values were investigated using both absorption and PA methods for the compounds and several of the alloys. Comparison of the results obtained from the two methods suggested that the energy gap is obtained in the PAS case, when the relative PA signal reaches somewhere between 50% and 70% of its peak value. Within this range the actual percentage value varies from sample to sample. In the present work, the criterion used for any particular section of alloys was that required to satisfy the compounds in the section.

3.7 Preparation of Samples, the Photoacoustic Cell, and Experimental Details

All the samples were prepared from the elements by the standard melt and anneal technique outlined in section 2.1. Homogenenity was checked using the Debye-Scherrer method (section 2.2) and, once obtained, samples were ground into fine powders. The choice of powdered samples gives several advantages. Firstly, condition C (section 3.5) is best satisfied for optically opaque solids by effectively reducing the thermal diffusion length, μ. Secondly, the choice

of powders allows for dilution with white powder thereby increasing ℓ_α to further satisfy condition C. And finally, powders conform to the vessel in which they are placed thus allowing equivalent reproducible samples to be made.

Once in a powdered form the alloys were placed in a sample holder and mounted within the photoacoustic cell. The gas - microphone cell for the PA system contains the sample and microphone, with its preamplifier, and an acoustically resonant section (figure 3.5). The following criteria governing the actual design of the cell were considered.

1. Acoustic Insulation: This was not a difficult problem since lock-in detection methods were used in analyzing the microphone signal. However, to ensure that environmental noise was limited, the microphone was well packed within the cell with foam insulation. The cell design also included walls of sufficient thickness to form a good acoustic barrier ($\sim$1.5mm).
2. Minimization of photoacoustic signal arising from interactions with the walls, windows, and microphone in the cell: This was achieved by employing windows as optically transparent as possible over the wavelength range. Since wavelengths in the visible region were of interest (see results), glass was a suitable material. The body of the cell was constructed of brushed stainless steel in order to minimize absorption of the incident and scattered radiation.

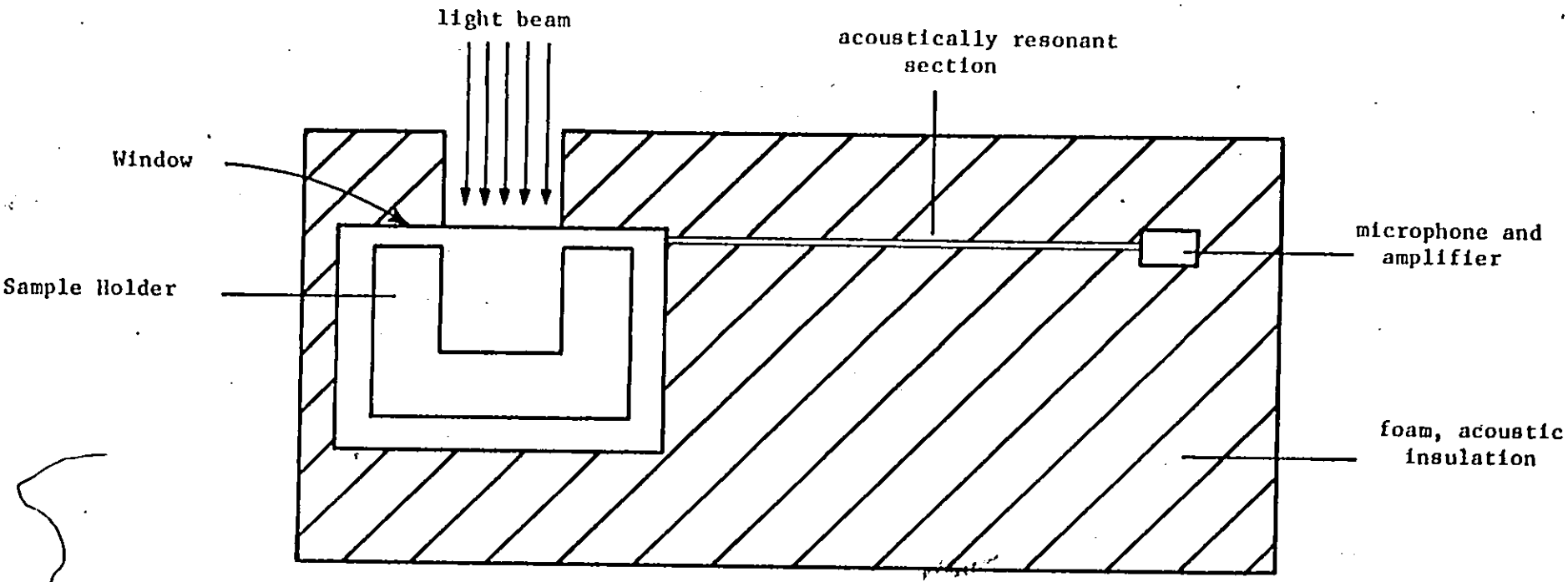

Figure 3.5 A photoacoustic cell with an acoustically resonant section.

3.7 Experimental Details

The photoacoustic measurements were made using the experimental arrangement depicted in figure 3.6. The light source used was a 650W quartz-iodine lamp. The light was chopped at 170Hz which was found experimentally to give maximum response. The monochromatic light from the exit slit of a CARL ZEISS (M4 QIII) spectrometer was focussed onto the sample. The photoacoustic signal was detected by a 1751 PA sensitive microphone via the resonance tube which was connected to the cell. The signal from the microphone was amplified by a PAR-213 amplifier. A PAR-210 selective amplifier which was tuned to the chopping frequency was used to reduce the noise signal other than at the chopping frequency. The signal from the selective amplifier was detected by a PAR-213 lock-in amplifier with a reference signal from the light chopper. The output from the lock-in amplifier was recorded by a digital multimeter as a function of wavelength of the incident light, and the photoacoustic spectrum obtained.

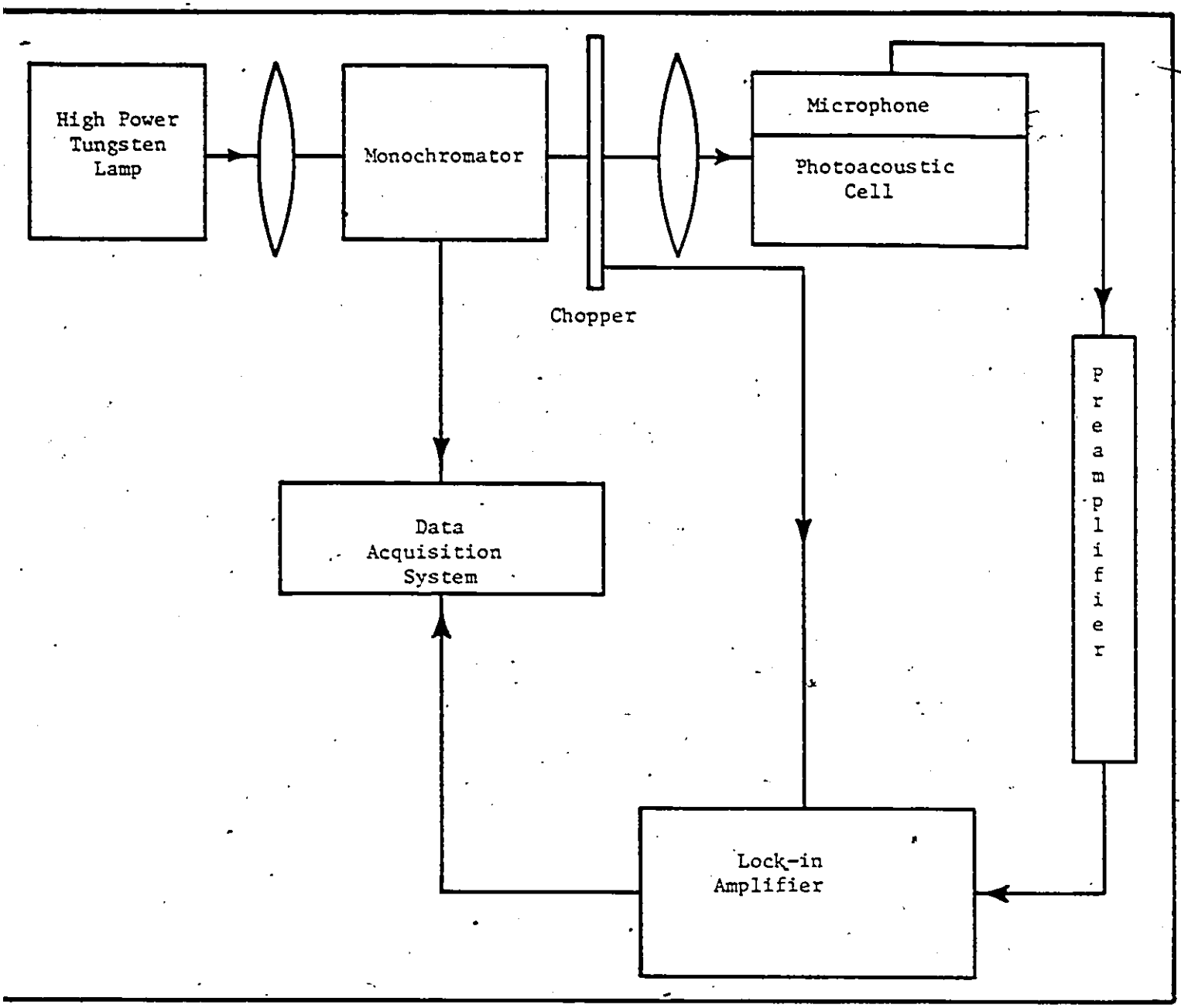

Figure 3.6 Block diagram of a photoacoustic spectrometer utilizing a gas-microphone cell.

CHAPTER IV - LATTICE PARAMETER RESULTS AND FITTING

4.1 Lattice Constant Results for the Faces of the Cube

Polycrystalline samples of the alloy system $(Cu_{1-x}Ag_x)(Ga_{1-y}In_y)(Se_{1-z}Te_z)_2$ with x, y, or z equal 0 or 1 were x-rayed using the Debye-Scherrer technique. Once equilibrium was attained these photographs were analyzed to determine values of lattice constants, a and c (see section 2.3 for details). Resulting experimental values are listed, in tables 4.1 to 4.5 (results for the Te face (z = 1) have been previously published (81A1)). Each sample was assigned a 6 digit number for convenient identification. The first two digits represent the value of x as a percent, and the 3rd and 4th, and last two digits represent y and z percentages respectively. In the case of x, y, or z equal to 1, or 100%, the composition variable was assigned a value of '10' in the identification number.

Graphs showing the variation of a and c as a function of composition for each of the 6 faces (x, y, or z equal to 0 or 1) are plotted in figures 4.1 through 4.6. As is seen in figures 4.6(a), (b), (c), and (d) for the tellurium face, lattice parameter values may be plotted as a function of either of two varying composition parameters. In the case of the tellurium face (z = 1), a and c have been plotted as a function of x at constant y and as a function of y at constant x. However, for the remaining faces, only one variation for each of a and c was plotted so that duplication of results was minimized. In most cases one of the variable composition parameters produces a clearer, more convenient graph. This is illustrated in figures 4.6(c) and (d)

Sample	a(nm)	c(nm)
000000	0.5619	1.1026
000025	0.5715	1.1232
000050	0.5813	1.1483
000075	0.5918	1.1703
000010	0.6025	1.1935
002500	0.5657	1.1181
002525	0.5759	1.1395
002550	0.5862	1.1626
002575	0.5957	1.1842
002510	0.6058	1.2068
005000	0.5697	1.1354
005025	0.5790	1.1595
005050	0.5900	1.1806
005075	0.6008	1.1984
005010	0.6098	1.2196
007500	0.5737	1.1475
007525	0.5841	1.1680
007550	0.5947	1.1893
007575	0.6052	1.2056
007510	0.6147	1.2295
001000	0.5794	1.1572
001025	0.5886	1.1767
001050	0.5964	1.1936
001075	0.6095	1.2186
001010	0.6201	1.2379

Table 4.1 Lattice constant values for x = 0 compositions.

Sample	a(nm)	c(nm)
250000	0.5695	1.1039
250025	0.5770	1.1218
250050	0.5865	1.1470
250075	0.5955	1.1705
250010	0.6081	1.1977
252500	0.5719	1.1187
252510	0.6119	1.2078
255000	multiphase	
255010	0.6169	1.2252
257500	multiphase	
257510	0.6196	1.2392
251000	0.5844	1.1690
251025	0.5918	1.1848
251050	0.6040	1.2082
251075	0.6115	1.2292
251010	0.6241	1.2468

Table 4.2 Lattice constant values for and multiphase samples for x = 0.25 compositions on the faces of the cubic composition range.

Sample	a(nm)	c(nm)
500000	multiphase	
500025	multiphase	
500050	multiphase	
500075	0.5945	1.1667
500010	0.6143	1.1996
502500	multiphase	
502510	0.6177	1.2129
505000	multiphase	
505010	0.6223	1.2309
507500	multiphase	
507510	0.6268	1.2440
501000	0.5919	1.1740
501025	0.6025	1.1935
501050	0.6087	1.2148
501075	0.6202	1.2402
501010	0.6309	1.2576

Table 4.3 Lattice constant values and multiphase samples for $x = 0.50$ compositions on the faces of the cubic composition range.

Sample	a(nm)	c(nm)
750000	0.5880	1.0970
750025	multiphase	
750050	0.6021	1.1470
750075	0.6127	1.1726
750010	0.6218	1.1995
752500	0.5902	1.1143
752510	0.6265	1.2160
755000	0.5935	1.1356
755010	0.6296	1.2336
757500	0.5973	1.1545
757510	0.6335	1.2497
751000	0.6000	1.1745
751025	0.6100	1.1961
751050	0.6152	1.2124
751075	0.6259	1.2372
751010	0.6369	1.2614

Table 4.4 Lattice constant values and multiphase sample for $x = 0.75$ compositions on the faces of the cubic composition range.

Sample	a(nm)	c(nm)
100000	0.5971	1.0952
100025	0.6054	1.1083
100050	0.6135	1.1400
100075	0.6221	1.1685
100010	0.6325	1.1991
102500	0.6017	1.1091
102525	multiphase	
102550	multiphase	
102575	0.6241	1.1829
102510	0.6349	1.2157
105000	0.6042	1.1284
105025	multiphase	
105050	0.6186	1.1734
105075	0.6255	1.1990
105010	0.6388	1.2338
107500	0.6072	1.1500
107525	0.6145	1.1667
107550	0.6220	1.1974
107575	0.6288	1.2185
107510	0.6415	1.2477
101000	0.6103	1.1713
101025	0.6161	1.1878
101050	0.6220	1.2111
101075	0.6338	1.2339
101010	0.6452	1.2639

Table 4.5 Lattice constant values and multiphase samples for x = 1.0 compositions.

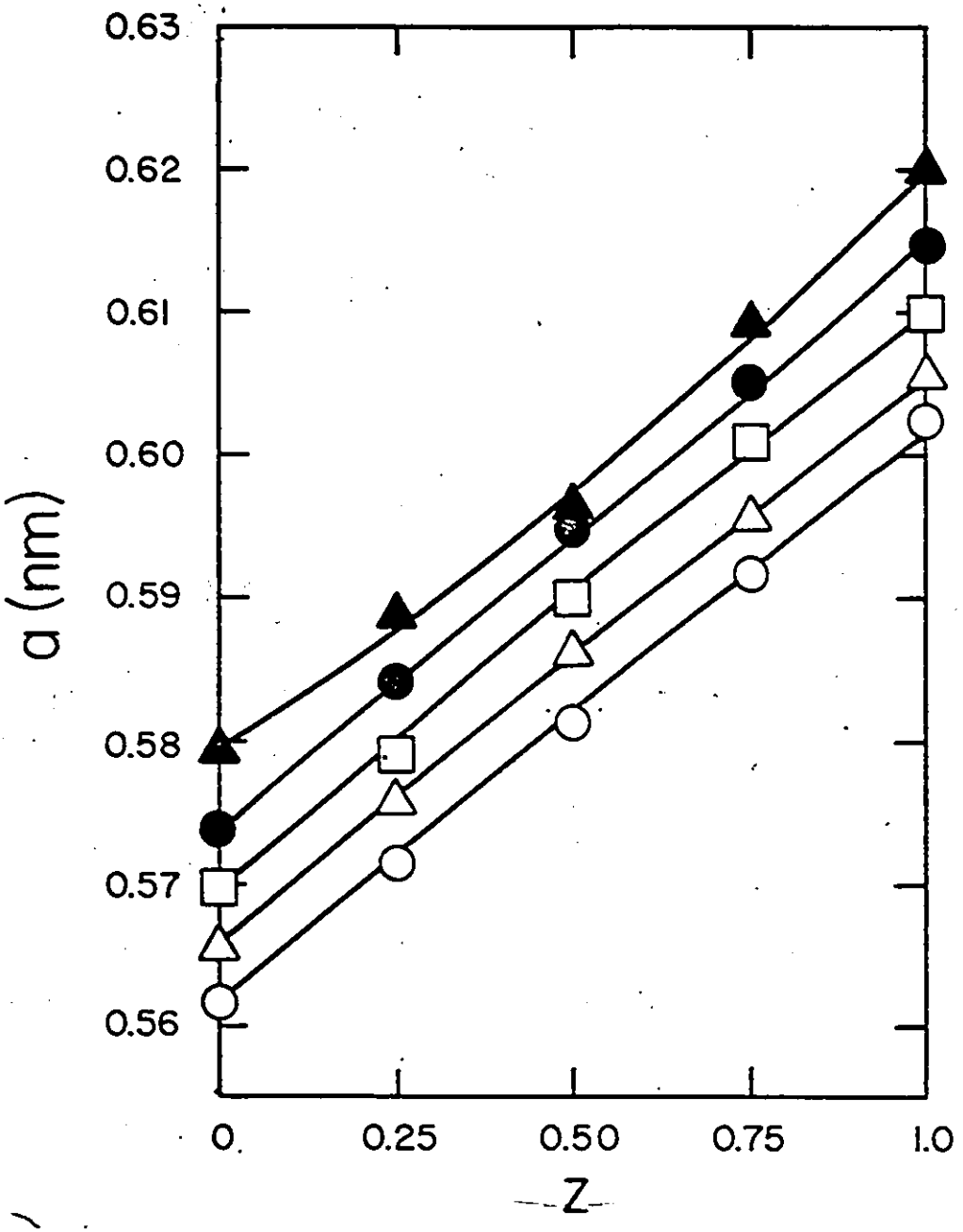

Figure 4.1(a) Variations of lattice parameter a for the Cu face as a function of z at various constant values of y. Curves have been drawn by fitting the experimental points to a nine term power series expression.
y = 0 ○, y = 0.25 △, y = 0.50 □, y = 0.75 ●, y = 1.0 ▲

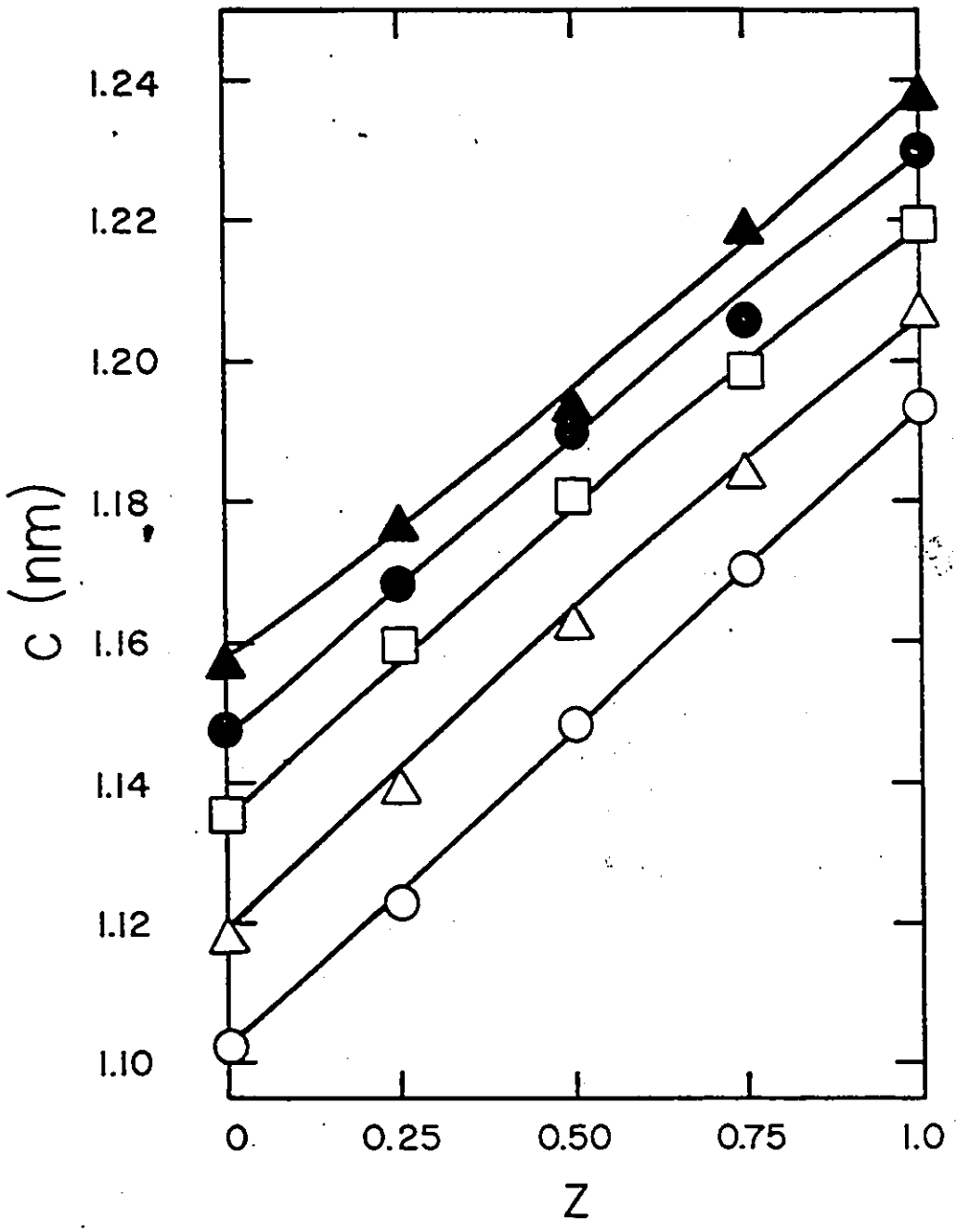

Figure 4.1(b) Variations of lattice parameter c for the Cu face as a function of z at various constant values of y. Curves have been drawn by fitting the experimental points to a nine term power series expression. y = 0 ○, y = 0.25 △, y = 0.50 □, y = 0.75 ●, y = 1.0 ▲

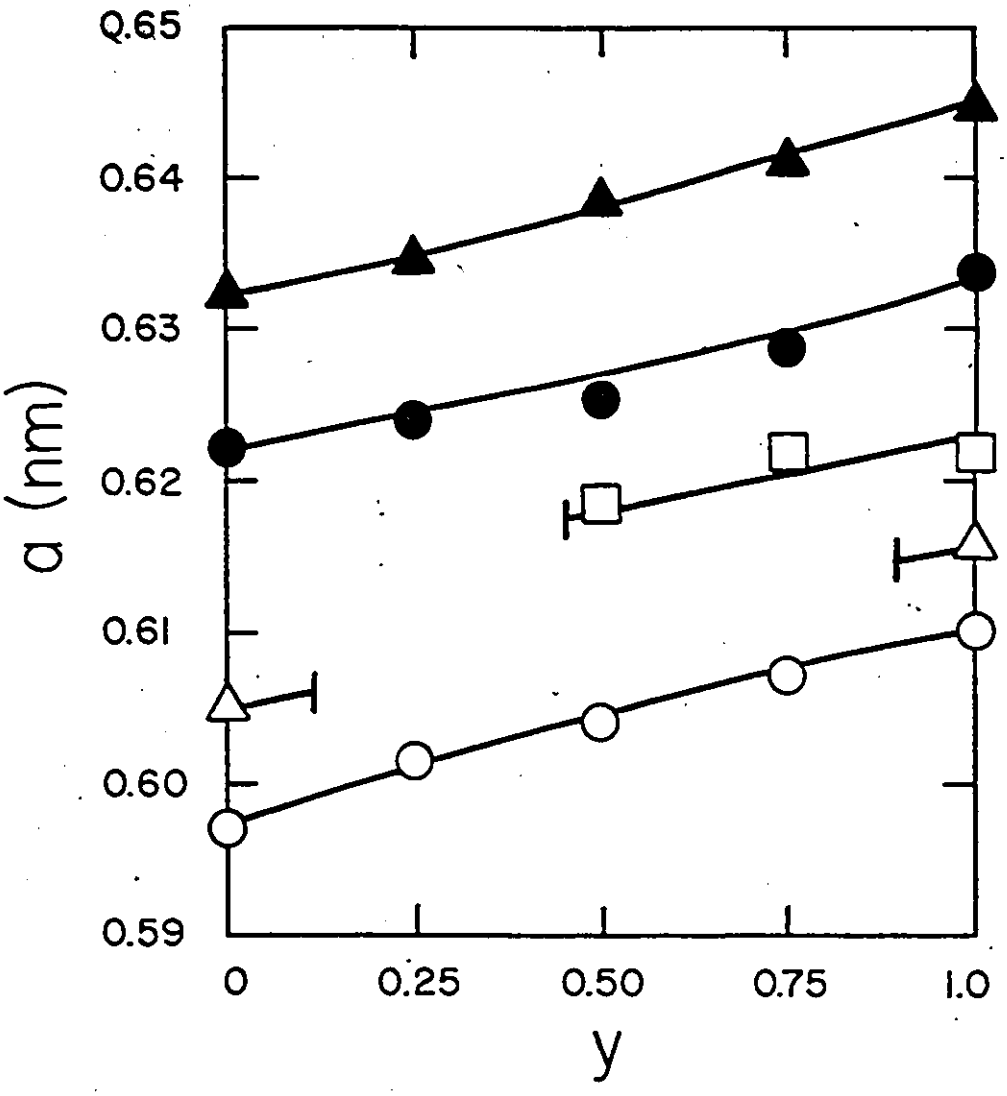

Figure 4.2(a) Variations of lattice parameter a for the Ag face as a function of y at various constant values of z. Curves have been drawn by fitting the experimental points to a nine term power series expression. Miscibility gaps occur for the z = 0.25 and z = 0.50 variations.
z = 0 ○, z = 0.25 △, z = 0.50 □, z = 0.75 ●, z = 1.0 ▲

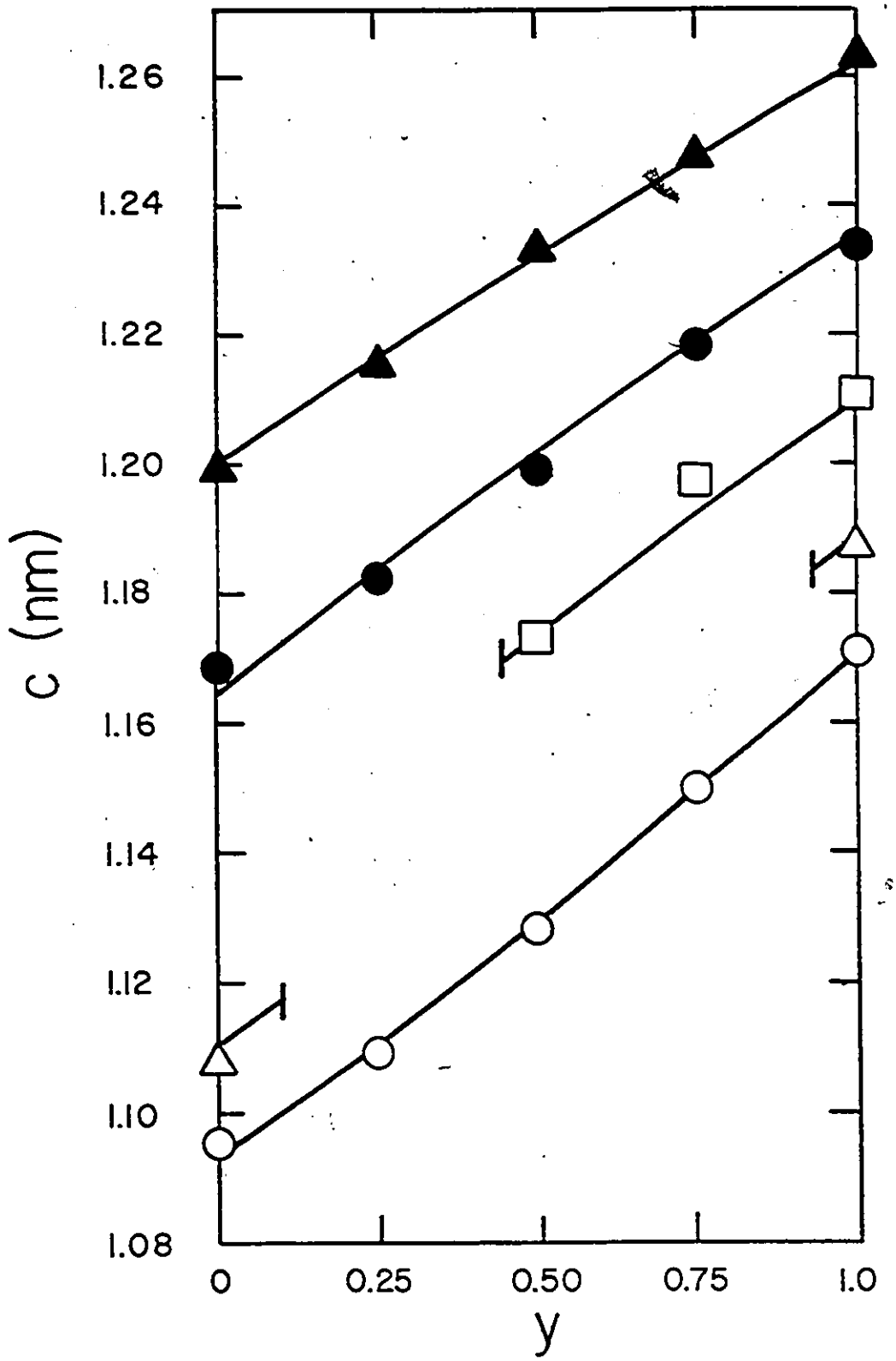

Figure 4.2(b) Variations of lattice parameter c for the Ag face as a function of y at various constant values of z. Curves have been drawn by fitting the experimental points to a nine term power ... expression. Miscibility gaps occur for the z = 0.25 and z = 0.50 variations.

z = 0 ○, z = 0.25 △, z = 0.50 □, z = 0.75 ●, z = 1.0 ▲

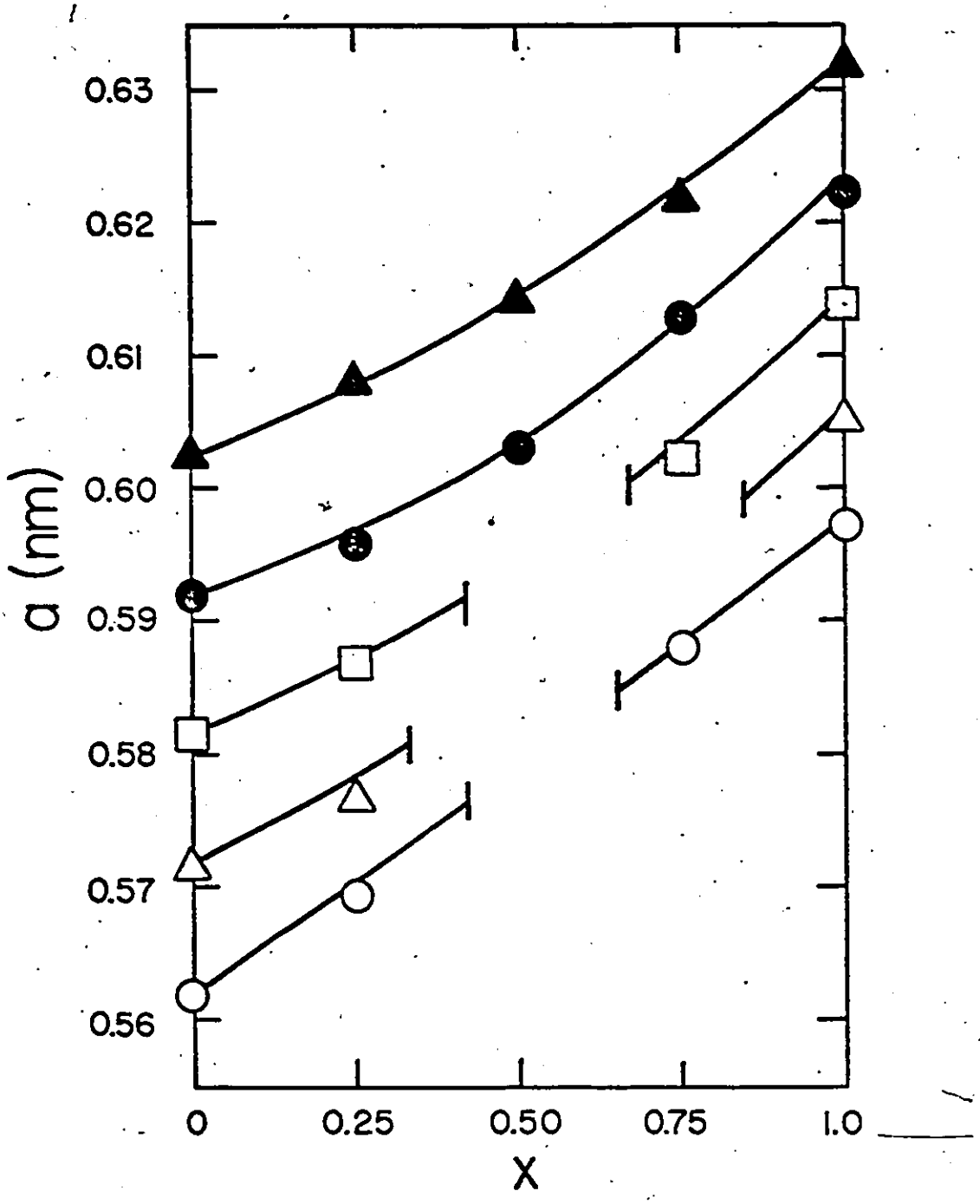

Figure 4.3(a) Variations of lattice parameter a for the Ga face as a function of x at various constant values of z. Curves have been drawn by fitting the experimental points to a nine term power series expression. Miscibility gaps occur for the z = 0, z = 0.25, and z = 0.50 variations.

z = 0○, z = 0.25△, z = 0.50□, z = 0.75●, z = 1.0▲

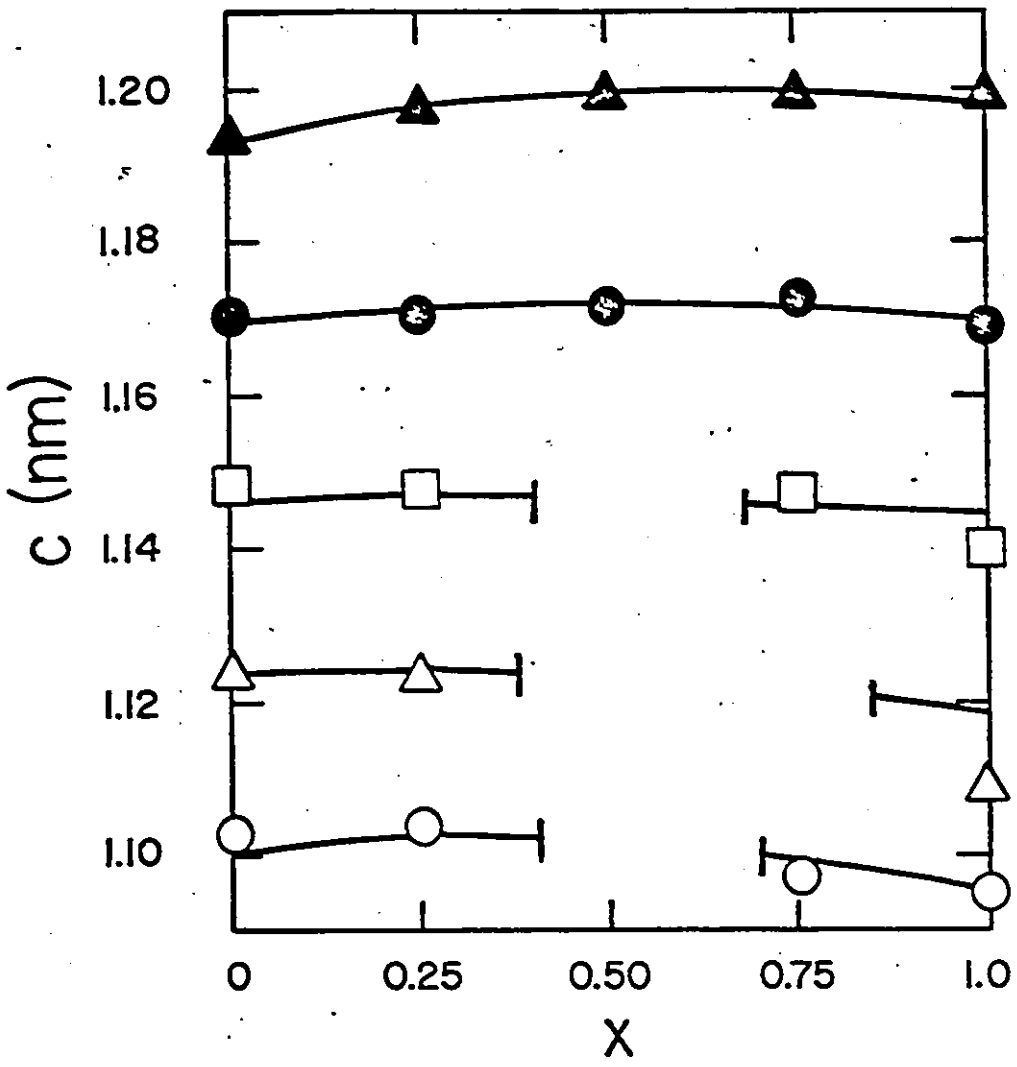

Figure 4.3(b) Variations of lattice parameter c for the Ga face as a function of x at various constant values of z. Curves have been drawn by fitting the experimental points to a nine term power series expression. Miscibility gaps occur for the z = 0, z = 0.25 and z = 0.50 variations.

z = 0 ○, z = 0.25 △, z = 0.50 □, z = 0.75 ●, z = 1.0 ▲

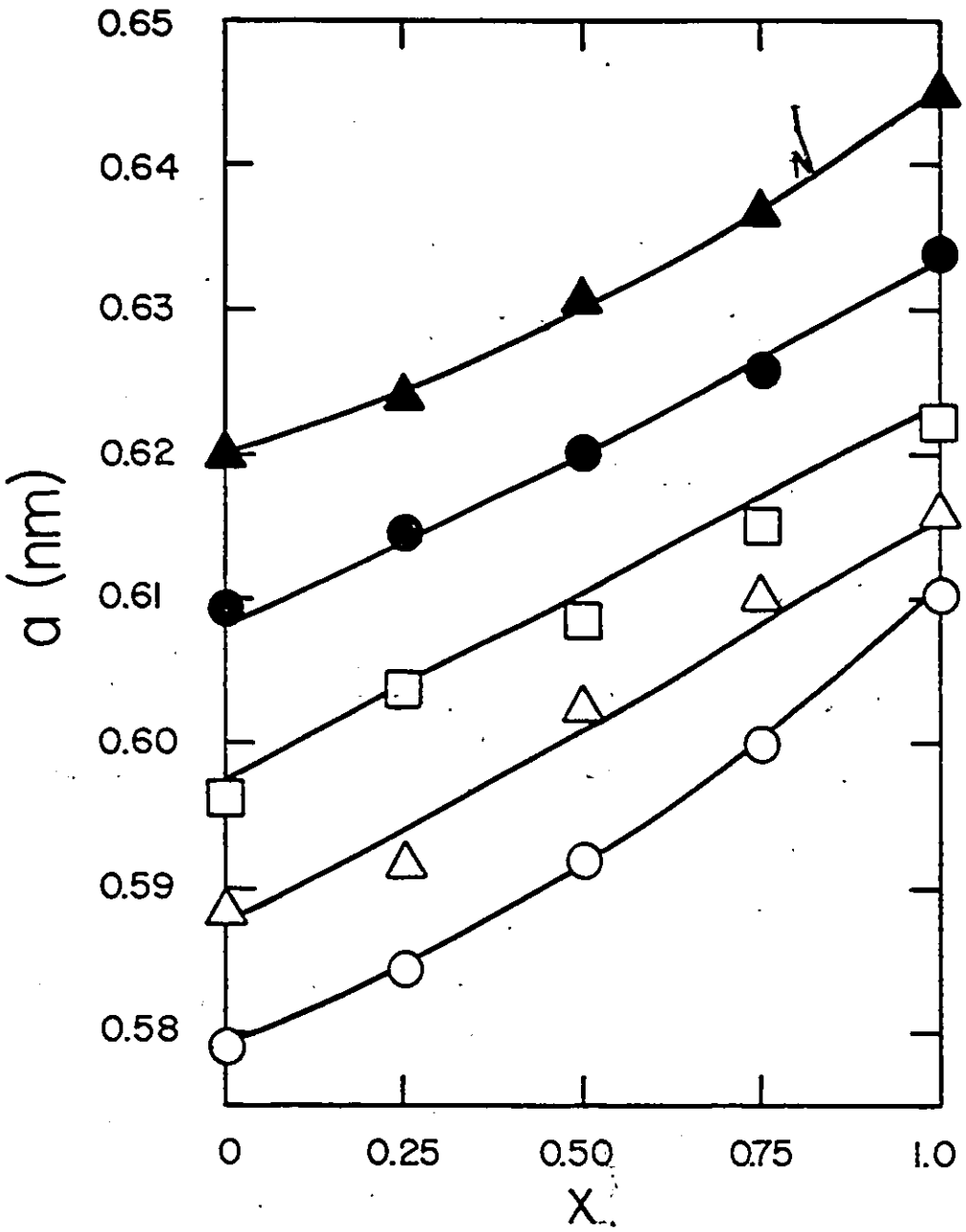

Figure 4.4(a) Variations of lattice parameter a for the In face as a function of x at various constant values of z. Curves have been drawn by fitting the experimental points to a nine term power series expression. z = 0 ○, z = 0.25 △, z = 0.50 □, z = 0.75 ●, z = 1.0 ▲

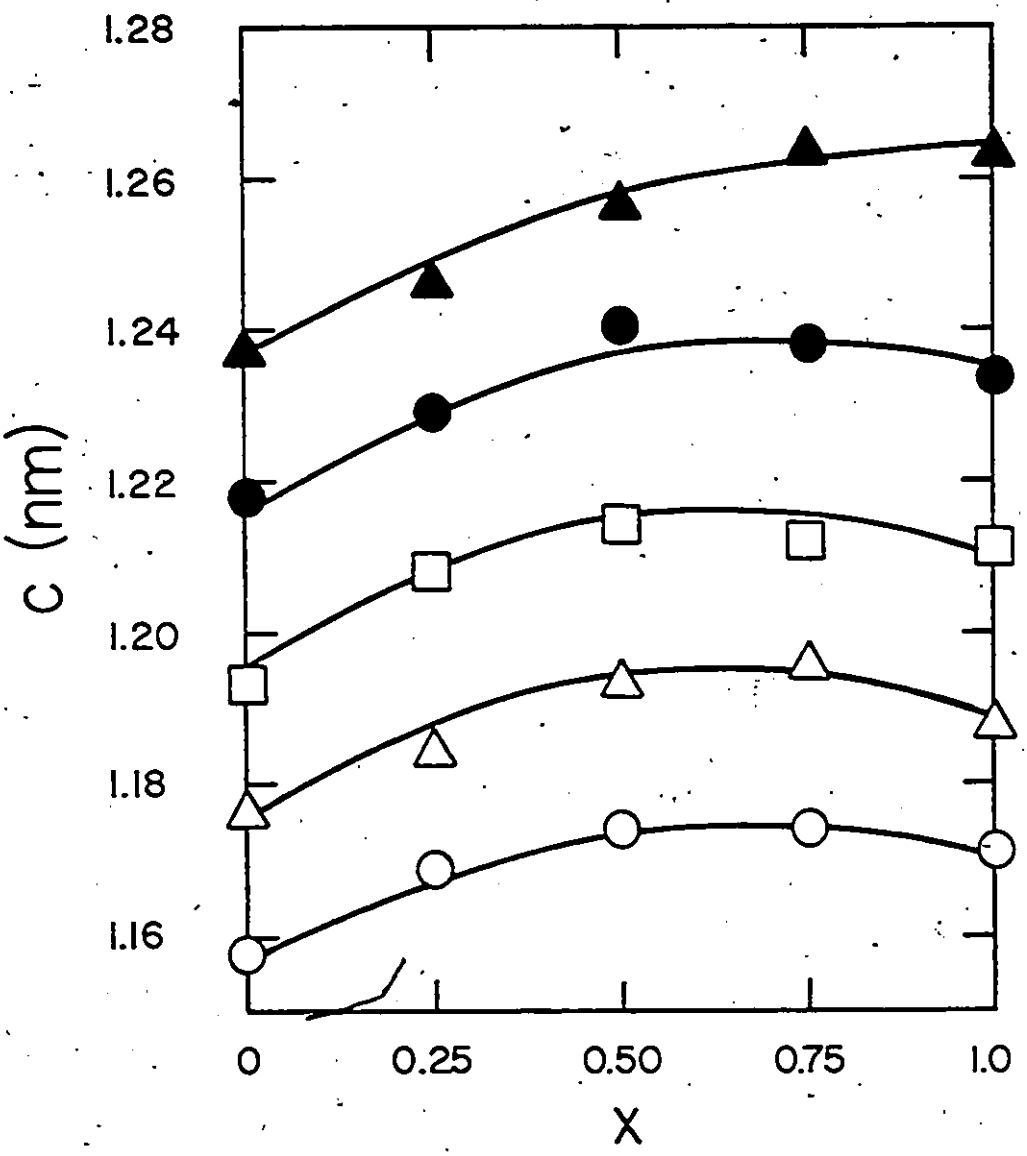

Figure 4.4(b) Variations of lattice parameter c for the In face as a function of x at various constant values of z. Curves have been drawn by fitting the experimental points to a nine term power series expression. z = 0 ○, z = 0.25 △, z = 0.50 □, z = 0.75 ●, z = 1.0 ▲

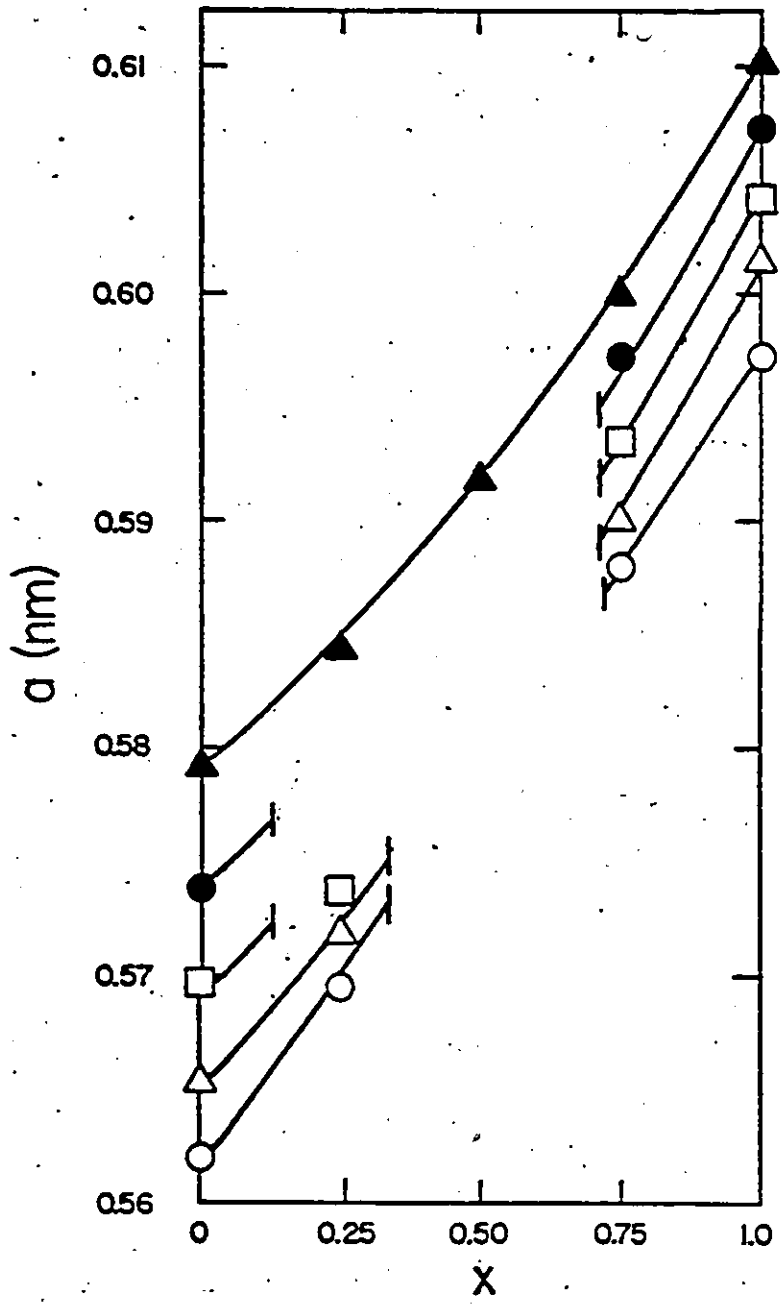

Figure 4.5(a) Variations of lattice parameter a for the Se face as a function of x at various constant values of y. Curves have been drawn by fitting the experimental points to a nine term power series expression. Miscibility gaps occur for the y = 0, y = 0.25, y = 0.50, and y = 0.75 variations.
y = 0 ○, y = 0.25 △, y = 0.50 □, y = 0.75 ●, y = 1.0 ▲

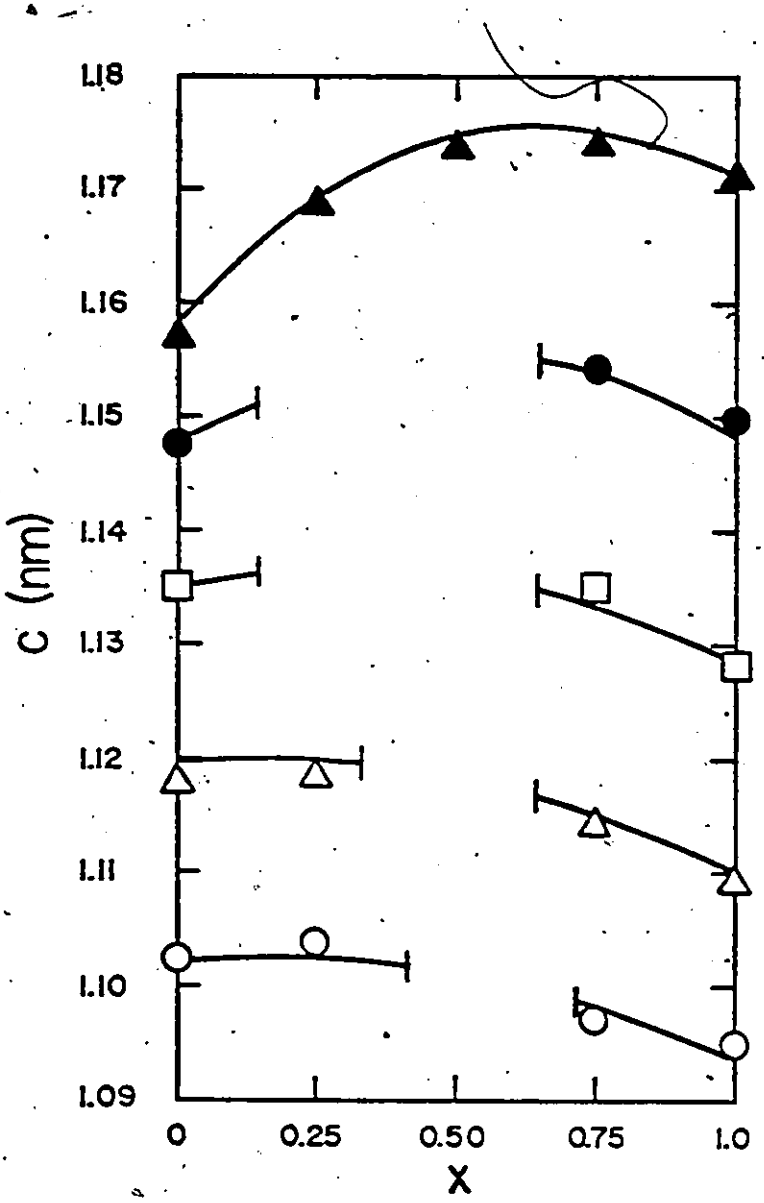

Figure 4.5(b) Variations of lattice parameter c for the Se face as a function of x at various constant values of y. Curves have been drawn by fitting the experimental points to a nine term power series expression. Miscibility gaps occur for the y = 0, y = 0.25, y = 0.50, and y = 0.75 variations.

y = 0○, y = 0.25△, y = 0.50□, y = 0.75●, y = 1.0▲

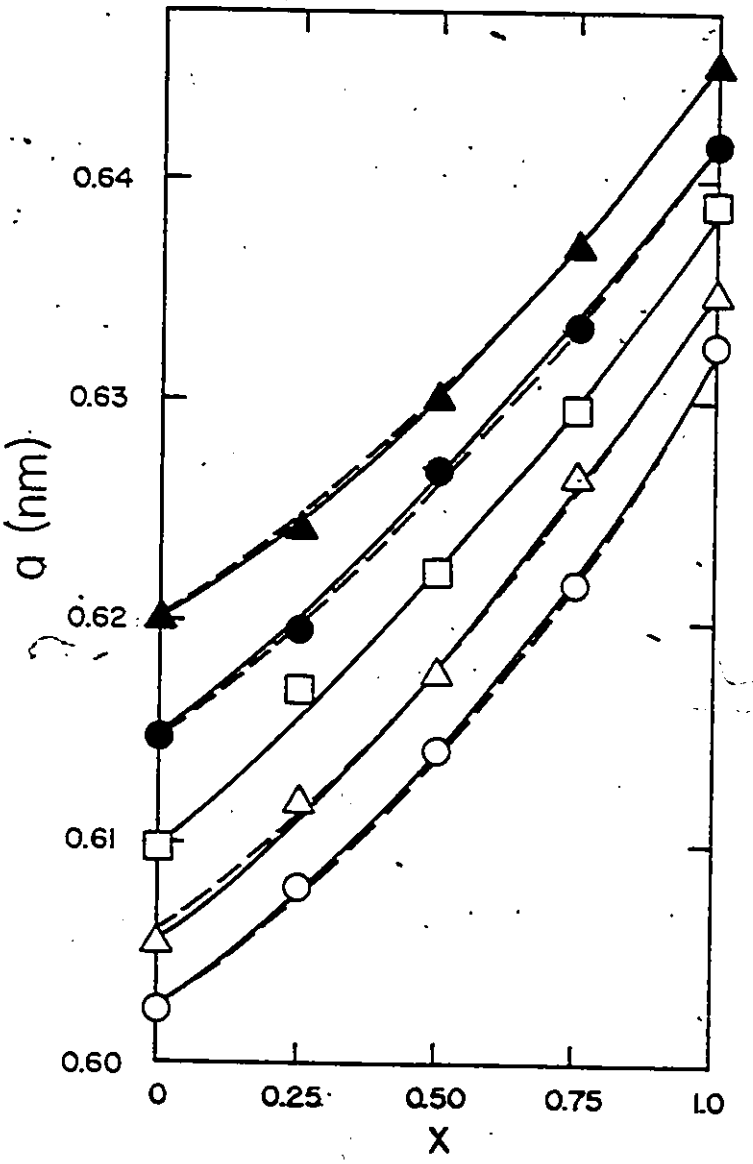

Figure 4.6(a) Variations of lattice parameter a for the Te face as a function of x at various constant values of y. Solid curves have been drawn by fitting the experimental points to a nine term power series expression. Dashed curves represent the variation predicted from a 26 term expression determined using an averaging technique.
y = 0 ○ , y = 0.25 △ , y = 0.50 □ , y = 0.75 ● , y = 1.0 ▲

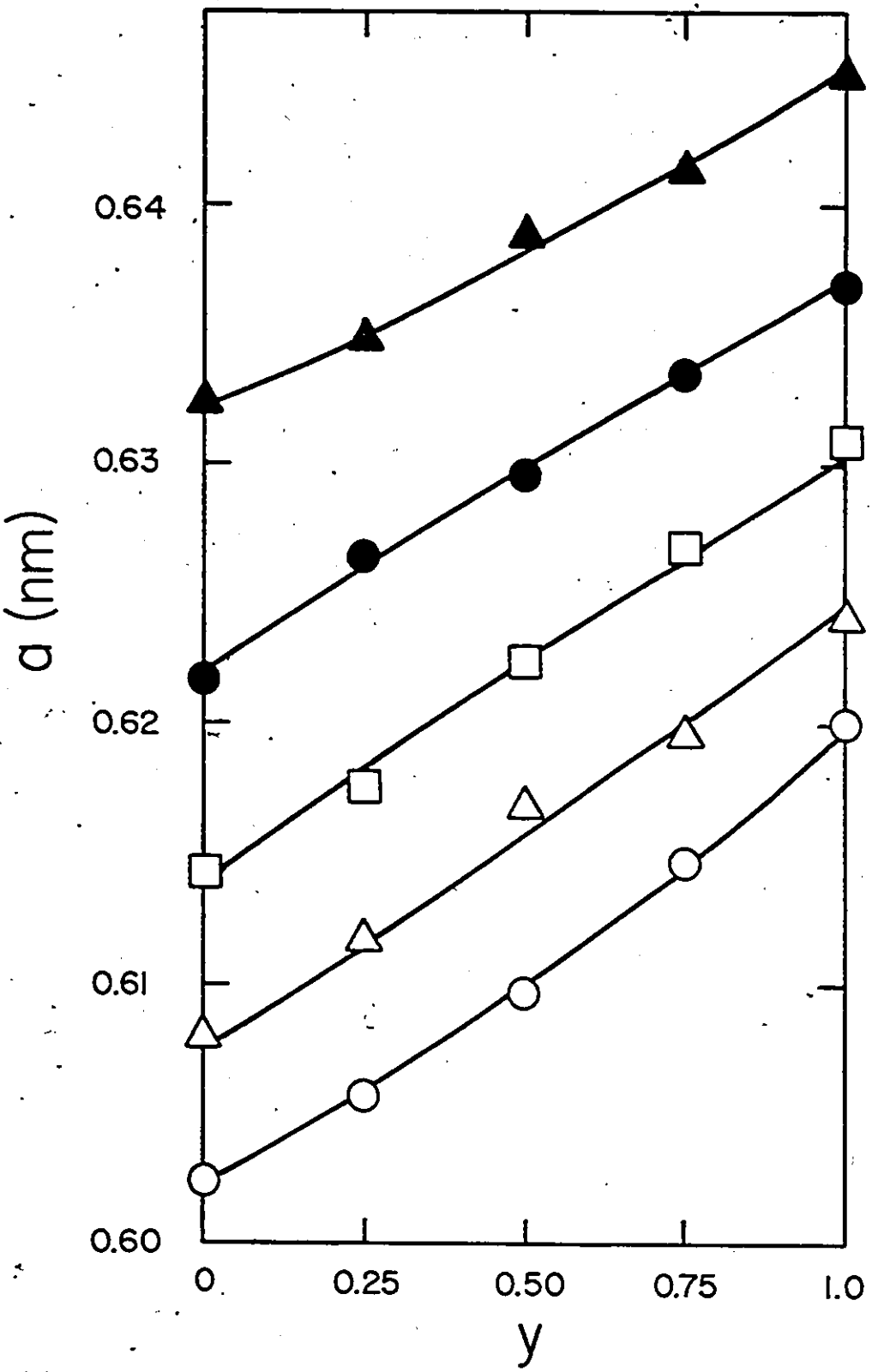

Figure 4.6(b) Variations of lattice parameter a for the Te face as a function of y at various constant values of x. Curves have been drawn by fitting the experimental points to a nine term power series expression.

x = 0 ○, x = 0.25 △, x = 0.50 □, x = 0.75 ●, x = 1.0 ▲

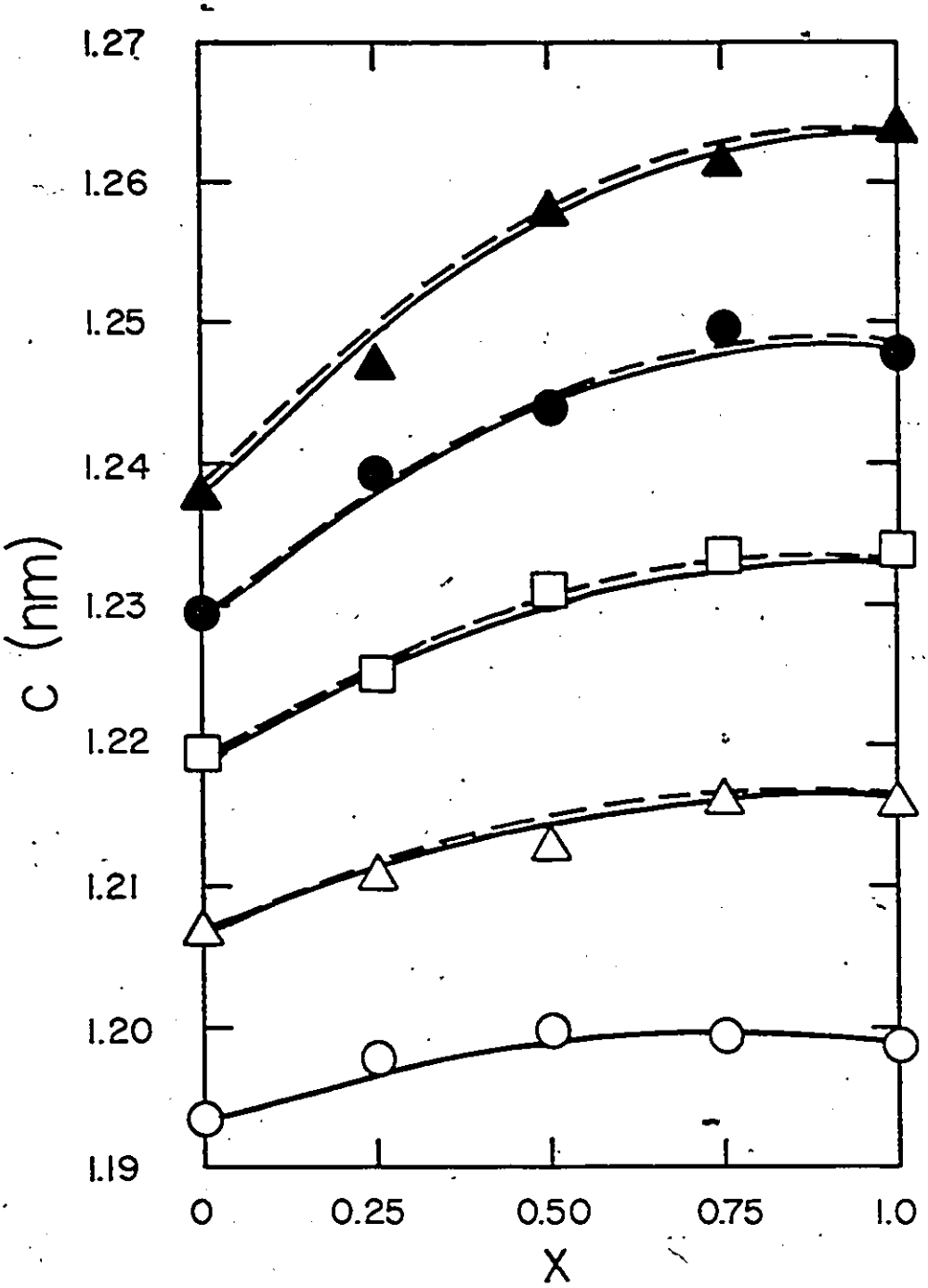

Figure 4.6(c) Variations of lattice parameter c for the Te face as a function of x at various constant values of y. Solid curves have been drawn by fitting the experimental points to a nine term power series expression. Dashed curves represent the variation predicted from a 26 term expression determined using an averaging technique.
y = 0 ○, y = 0.25 △, y = 0.50 □, y = 0.75 ●, y = 1.0 ▲

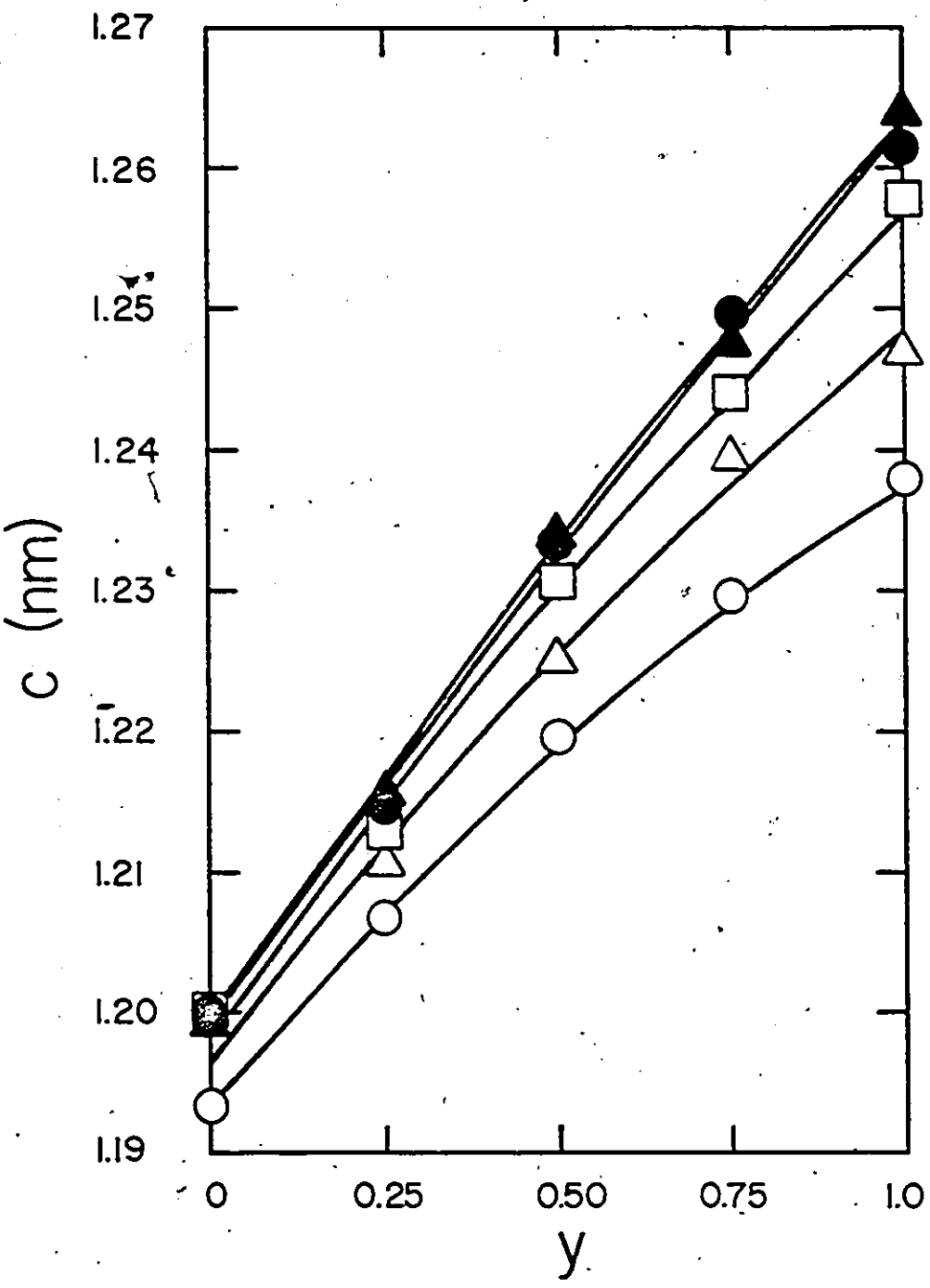

Figure 4.6(d) Variations of lattice parameter c for the Te face as a function of y at various constant values of x. Curves have been drawn by fitting the experimental points to a nine term power series expression.
x = 0 ○, x = 0.25 △, x = 0.50 □, x = 0.75 ●, x = 1.0 ▲

for the tellurium c variations, where c plotted as a function of x produces a clearer graph. Thus, for the remaining faces, the most convenient variation in this regard was plotted.

It can be seen in all cases that the variation of a and c with the appropriate composition variable does not take the linear form shown by Robbins et al (73R2) for various pseudo-binary sections involving selenides and sulphides. Within the limits of experimental error, all curves can be fitted to a parabolic form as shown by Chapman et al (79C1, 79C2) for $(Cu_{1-x}Ag_x)In(Se_{1-z}S_z)_2$ alloys. Also apparent from the graphs is a certain degree of scatter in the results. Some scatter, however, was expected for these alloys since complete equilibrium was not attained even after annealing for periods of up to 5 months. This was indicated by the occurrence of blurring of the high angle diffraction lines in the x-ray photographs of the corresponding samples.

In the gallium, silver, and selenium faces it was found that some photographs showing reasonably sharp diffraction lines gave a and c parameters very different from those expected from the curves shown in figures 4.2 and 4.3. These results are indicative of two phase behavior, and upon studying the appropriate photographs, the presence of the second phase was observed. The detection of such effects was not easy, however, due to several factors. Firstly, faint ordering lines present on the x-ray photographs were not measured in any detail. Hence it was possible to confuse these lines with faint lines resulting from the second phase. Secondly, the situation may have been

further complicated by multiphase rather than two-phase behavior, and finally, no simple straight line extrapolation could be used to determine phase limits as in the case of a binary diagram. Thus, the initial criterion for determining two phase or multiphase behavior was the observation of systematic deviations in lattice parameter values from the expected values. Although difficult, multiphase behavior was verified by detection of a second phase on the x-ray powder photographs.

Only estimates can be made at this stage on the boundaries of the miscibility gap, the reason being that although total of 125 compositions were investigated, this gave only five points on each curve in figures 4.1 through 4.6. Thus it was uncertain in several cases whether scatter in the data was due to poor equilibrium or proximity to the boundary edge. Miscibility gaps are shown in figures 4.2, 4.3 and 4.5 for the gallium, silver, and selenium faces.

As mentioned in the introduction (section 1.3), previous work on the $Cu_{1-x}Ag_xGaSe_2$, alloys indicated that only limited solid solubility was found over the composition range. Robbins et al (73R1, 73R2) have shown a miscibility gap to occur between the x = 0.45 and x = 0.65 compositions of this system. In the present work, results from the selenium face indicate that the $(Cu_{0.25}Ag_{0.75})GaSe_2$ alloy appears to be single phase. The $(Cu_{0.5}Ag_{0.5})GaS_2$ composition, however, was found to be multiphase. These results are, thus, consistent with those determined previously by Robbins et al. It has also been suggested by Robbins et al that if the change in the value of the c:a ratio along the $(Cu_{1-x}Ag_x)GaSe_2$ line is greater than 0.13, i.e. $\Delta(\frac{c}{a}) > 0.13$, then a miscibility gap will occur along this line. If this idea is extended over the cubic composition range it is expected that each of the Ag, Ga, and Se faces will exhibit multiphase behavior, since $\Delta(\frac{c}{a})$ is large in each of these cases. Thus, this extension is also consistent with the present experimental results.

In order to carry out further analysis of the lattice parameter data it is necessary to express a and c as functions of the composition parameters. As was mentioned previously, the variation of a and c can be fitted to parabolic form. This indicates the form of the empirical equation that must be used for the general alloys for a given face (x, y, or z equal to 0 or 1) with two variable parameters. The two variable composition parameters (u, v) appropriate to the face concerned cannot have powers of u or v higher than u^2 or v^2 in the general equation. Thus each parameter a and c for a given face has been fitted to equations of the form

$$a = \alpha_o + \beta_o u + \gamma_o v + \delta_o u^2 + \varepsilon_o v^2 + \zeta_o uv + \eta_o u^2 v + \theta_o uv^2 + \lambda_o u^2 v^2 \text{ nm} \quad (4.1)$$

or

$$c = \alpha_o' + \beta_o' u + \gamma_o' v + \delta_o' u^2 + \varepsilon_o' v^2 + \zeta_o' uv + \eta_o' u^2 v + \theta_o' uv^2 + \lambda_o' u^2 v^2 \text{ nm} . \quad (4.2)$$

Thus the values of a and c for a given face are given in terms of nine constants which were treated as adjustable parameters when a fit was made to the data for that face.

Fits were made separately to the data for each of the six faces. In each case a least squares method was used to give values of the nine coefficients in equation (4.1) and (4.2) (see appendix for least squares method). The values obtained, the number of points used in each case, and the standard deviation, σ, for the data points are summarized in table 4.6.

face		Cu	Ag	Ga	In	Se	Te
number of points		25	20	20	25	19	25
variable composition parameters (u,v)		(y,z)	(y,z)	(x,z)	(x,z)	(x,y)	(x,y)
Lattice Constant a(nm)	α_o	0.5620	0.5975	0.5617	0.5791	0.5618	0.6027
	β_o	0.0136	0.0155	0.0330	0.0193	0.0320	0.0161
	γ_o	0.0400	0.0277	0.0371	0.0318	0.0121	0.0121
	δ_o	0.0036	-0.0028	0.0025	0.0122	0.0035	0.0134
	ε_o	0.0005	0.0072	0.0038	0.0095	0.0054	0.0052
	ζ_o	0.0172	-0.0211	-0.0558	0.0290	-0.0245	0.0217
	η_o	-0.0248	0.0101	0.0489	-0.0446	0.0257	-0.0223
	θ_o	-0.0194	0.0148	0.0397	-0.0339	0.0126	-0.0215
	λ_o	0.0279	-0.0036	-0.0386	0.0428	-0.0215	0.0178
	σ	0.0005	0.0007	0.0004	0.0010	0.0006	0.0004
Lattice Constant c(nm)	α_o'	1.1573	1.1713	1.1025	1.1572	1.1022	1.1933
	β_o'	-0.0345	-0.0924	0.0030	0.0511	0.0047	0.0153
	γ_o'	0.0726	0.0674	0.0851	0.0714	0.0748	0.0580
	δ_o'	-0.0209	0.0143	-0.0109	-0.0372	-0.0130	-0.0098
	ε_o'	0.0088	0.0275	0.0061	0.0091	-0.0186	-0.0137
	ζ_o'	0.0593	0.0619	-0.176	0.0548	-0.0230	0.0203
	η_o'	-0.0418	-0.0671	0.0238	-0.0635	0.0098	-0.0056
	θ_o'	-0.0577	-0.0326	0.0331	-0.0510	0.0726	0.0162
	λ_o'	0.0502	0.0529	-0.0268	0.0721	-0.0383	-0.0104
	σ	0.0013	0.0018	0.0011	0.0015	0.0022	0.0011

Table 4.6 Coefficients corresponding to equations (4.1) and (4.2) for each of the six faces. The number of points used in the least squares fit and the standard deviation, σ, is also listed in each case.

It can be seen from the table that the standard deviations are small so that these values are determined by scatter in the data as seen in the graphs (4.1-4.6) and not by any systematic misfit of the fitting equations, (4.1) and (4.2).

The fitting equations (4.1) and (4.2) together with the appropriate coefficients listed in Table 4.6 can be used to give separately the contours of constant a and c for each face. These contours are shown in figures 4.7 through 4.12. Since the six sets of data in Table 4.6 correspond to the faces of a cube, each cube edge is common to two faces. Thus sections of adjacent faces are also shown in figures 4.7-4.12 even though the analysis for each face was treated separately. Ideally it is expected that the contours should exactly match on either side of a cube edge. As can be seen in the figures the agreement with this is reasonably good. Regardless of this however, the equations describing the a and c variations are not unique. The coefficients of the higher terms can vary to some extent, with a variation in one coefficient compensated by a variation in the opposite direction by another coefficient. This effectively occurs without a change in the value of the standard deviation, and is not unexpected since the analysis requires the fitting of nine parameters from as few as 19 points (selenium face).

In view of the above results, each face can be considered as a section of a larger three-dimensional problem. In general, it is necessary to fit to a power series in x, y, and z which, if terms containing cubed or higher powers are neglected, contains 27 terms, i.e.

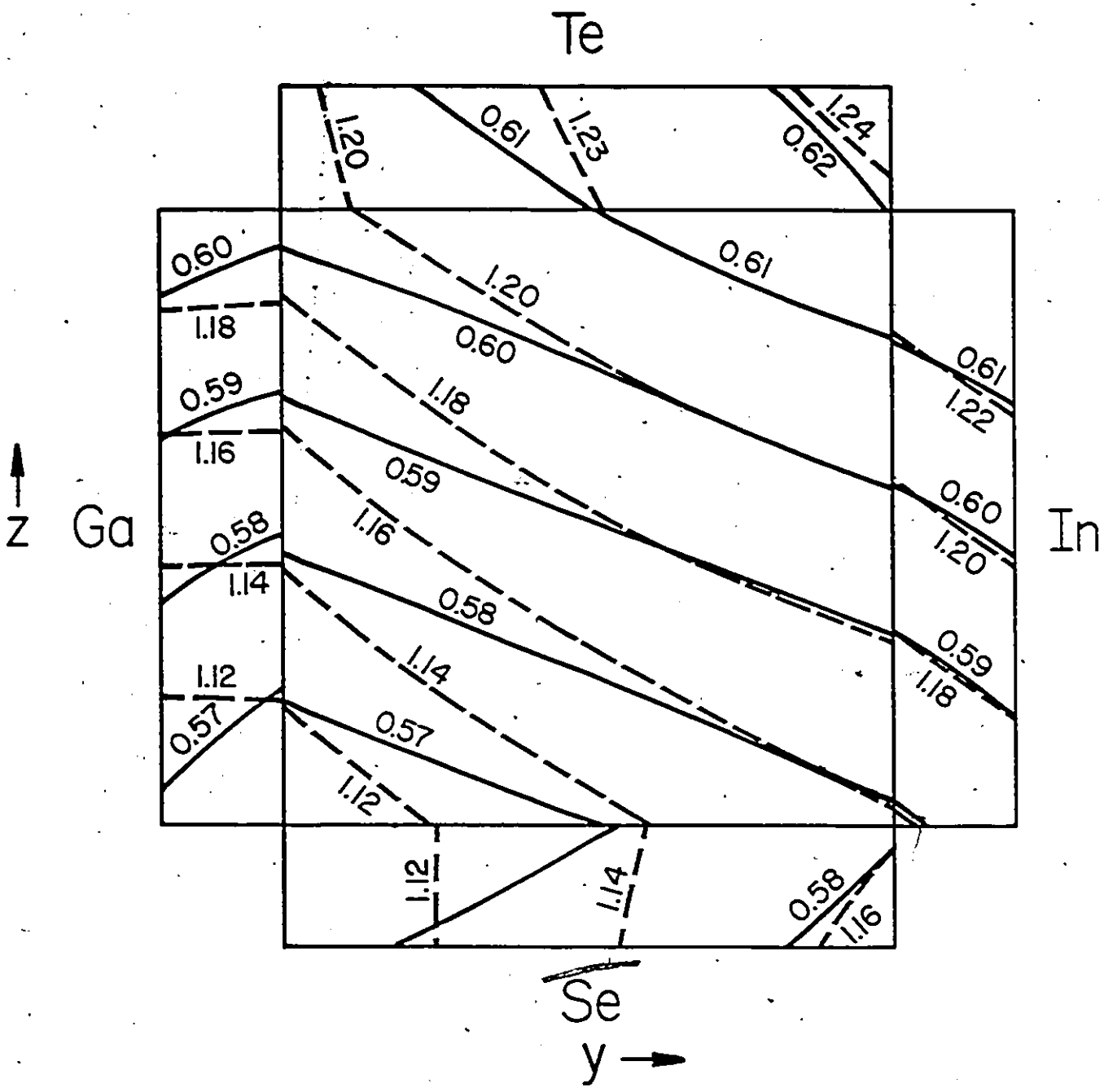

Figure 4.7 Contours of constant a (solid curves) and constant c (dashed curves) for the Cu face. Also shown are constant a and c contours for sections of the faces adjacent to the Cu face. (Contours are given in nm).

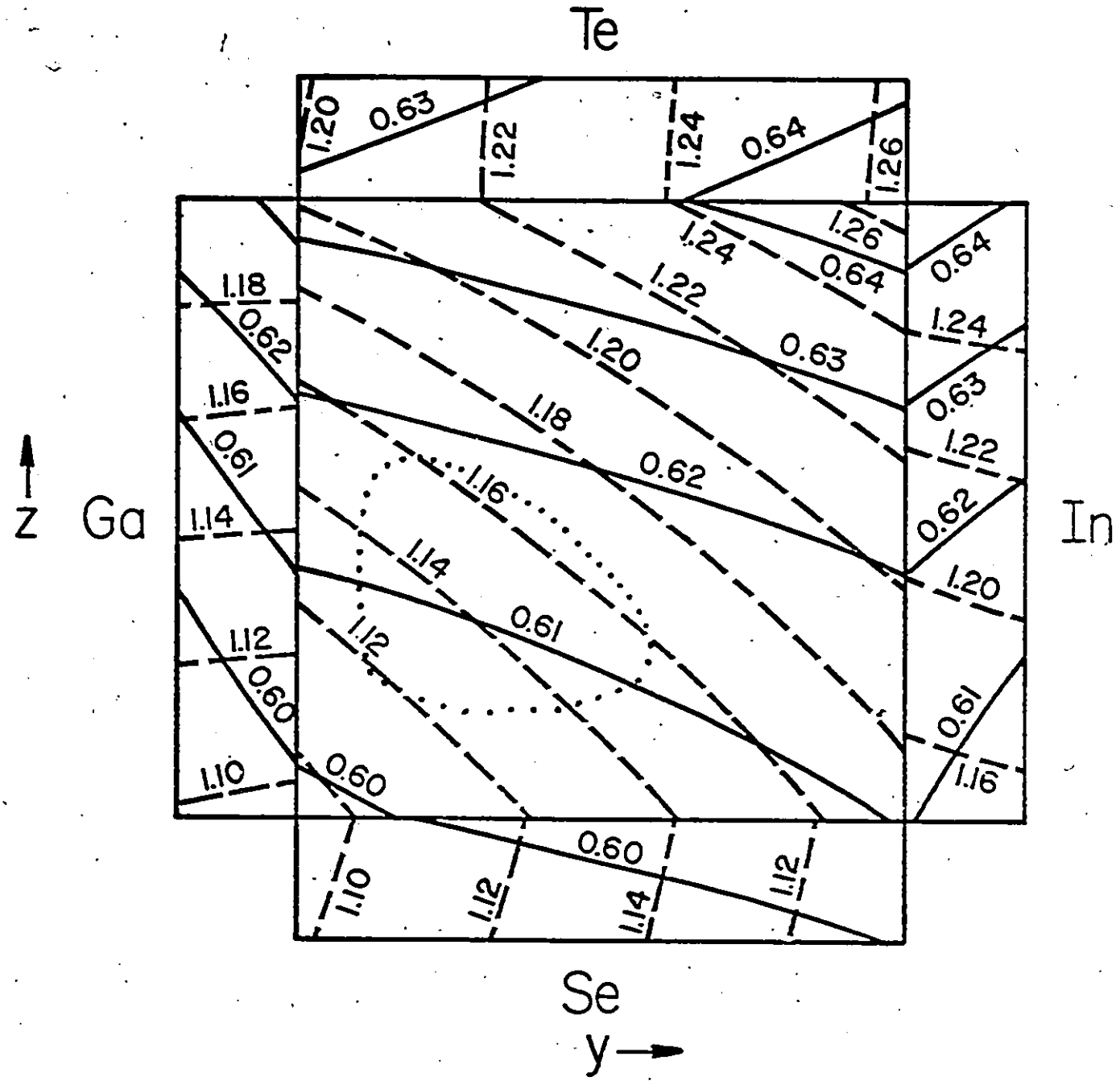

Figure 4.8 Contours of constant a (solid curves) and constant c (dashed curves) for the Ag face. Also shown are constant a and c contours for sections of the faces adjacent to the Cu face. (Contours are given in nm). A multiphase region is outlined by the dotted curve.

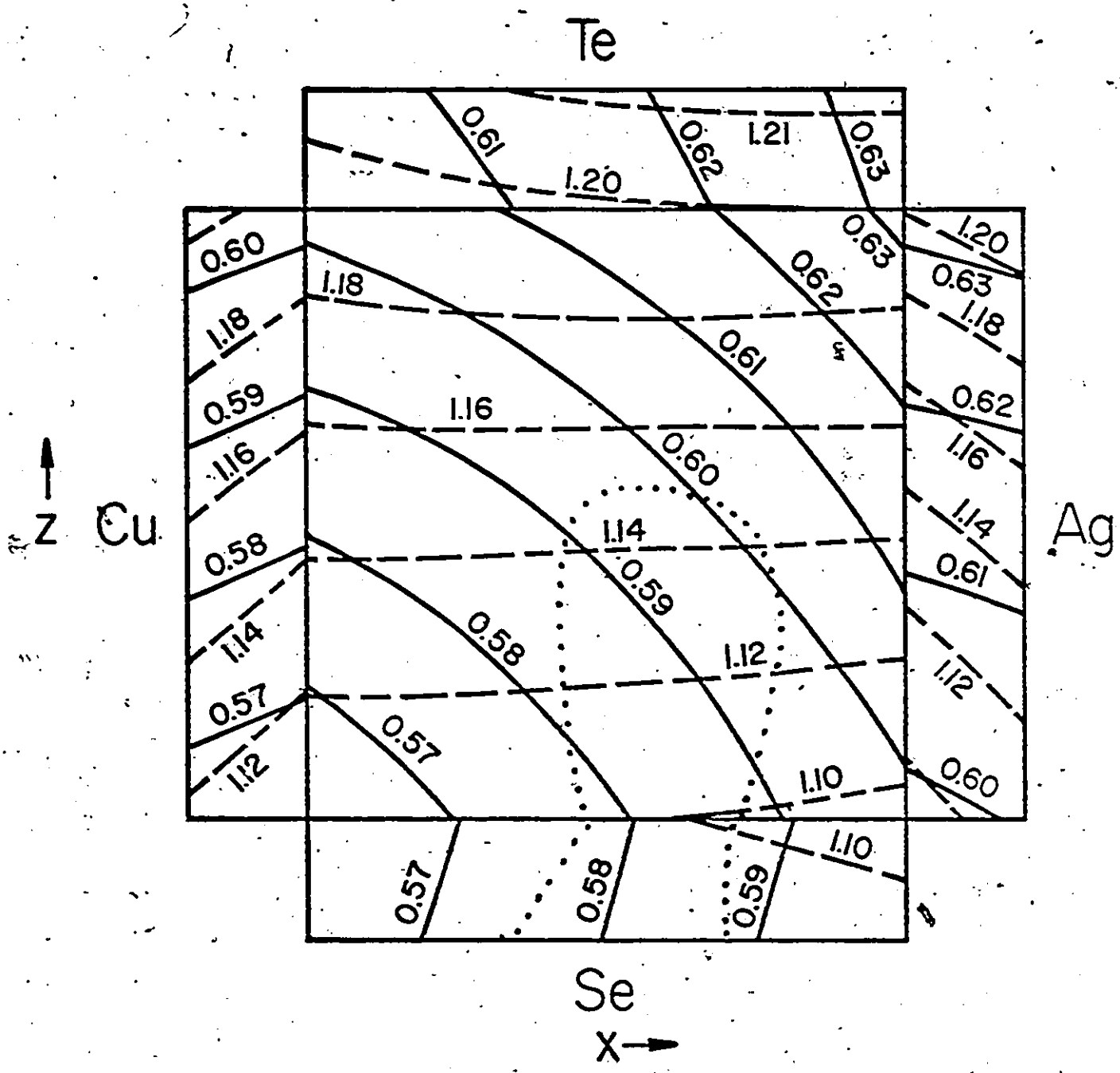

Figure 4.9 Contours of constant a (solid curves) and constant c (dashed curves) for the Ga face. Also shown are constant a and c contours for sections of the faces adjacent to the Ga face. (Contours are given in nm). A multiphase region is outlined by the dotted curve.

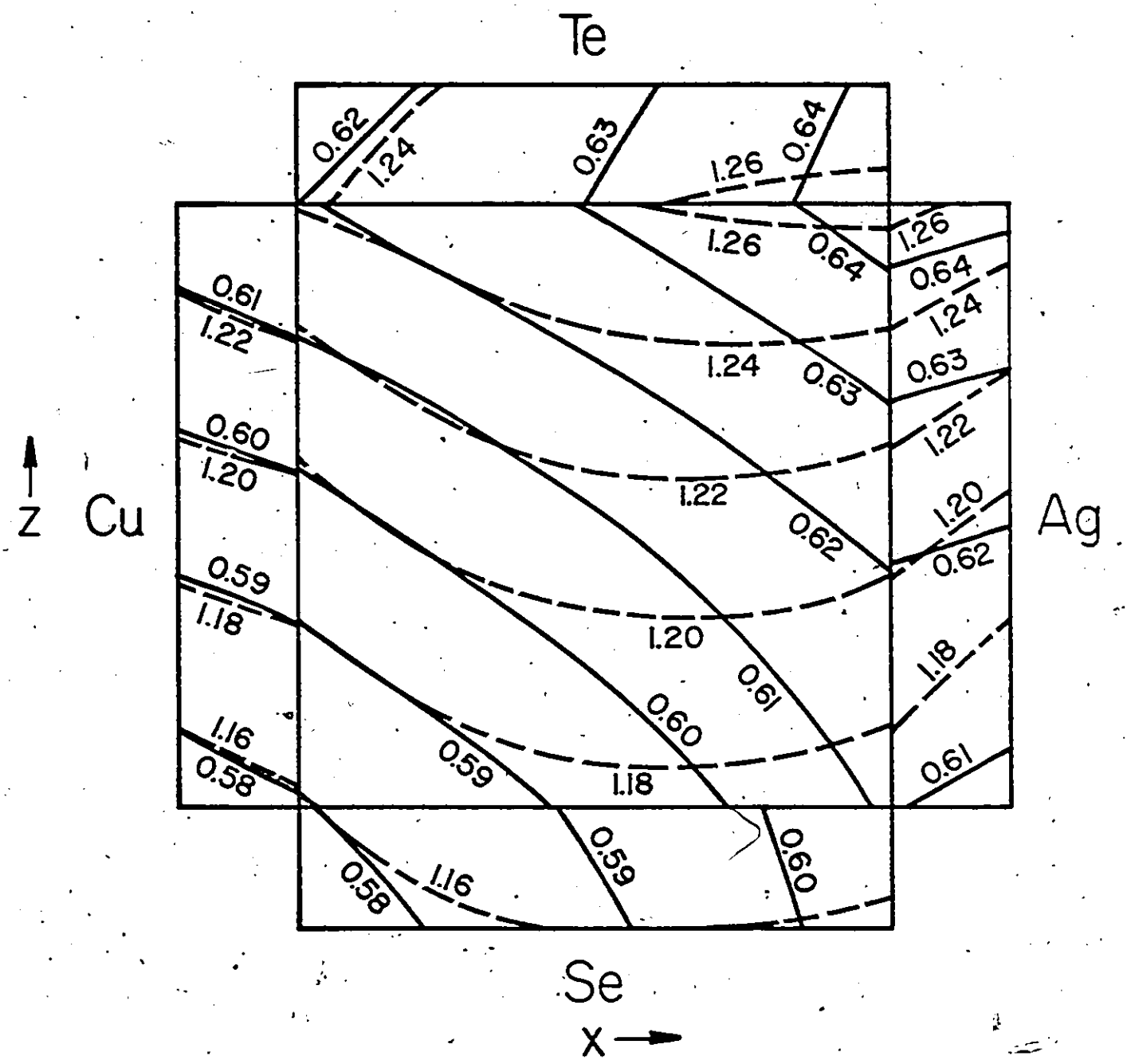

Figure 4.10 Contours of constant a (solid curves) and constant c (dashed curves) for the In face. Also shown are constant a and c contours for sections of the faces adjacent to the In face. (Contours are given in nm).

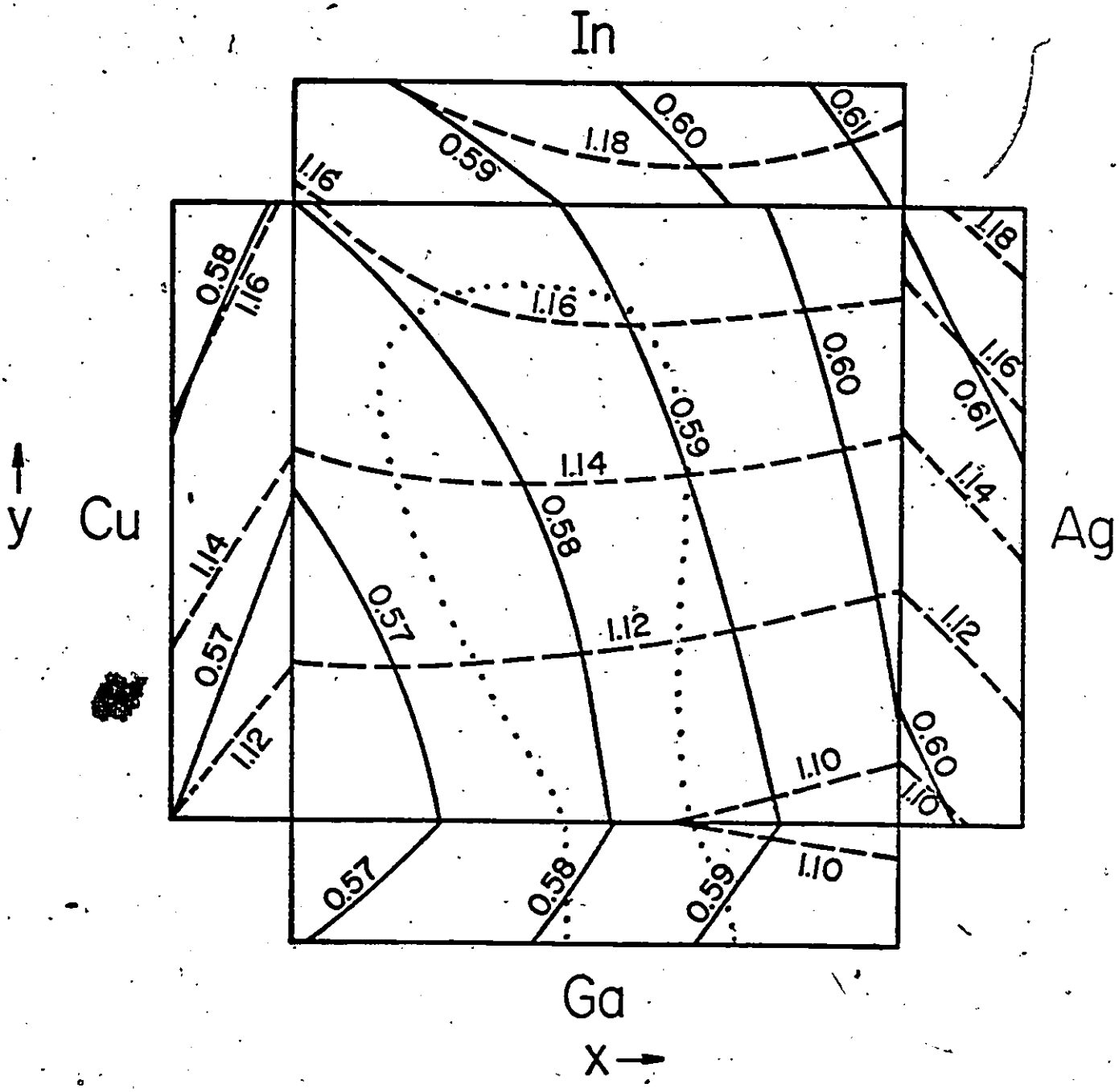

Figure 4.11 Contours of constant a (solid curves) and constant c (dashed curves) for the Se face. Also shown are constant a and c contours for sections of the faces adjacent to the Se face. (Contours are given in nm). A multiphase region is outlined by the dotted curve.

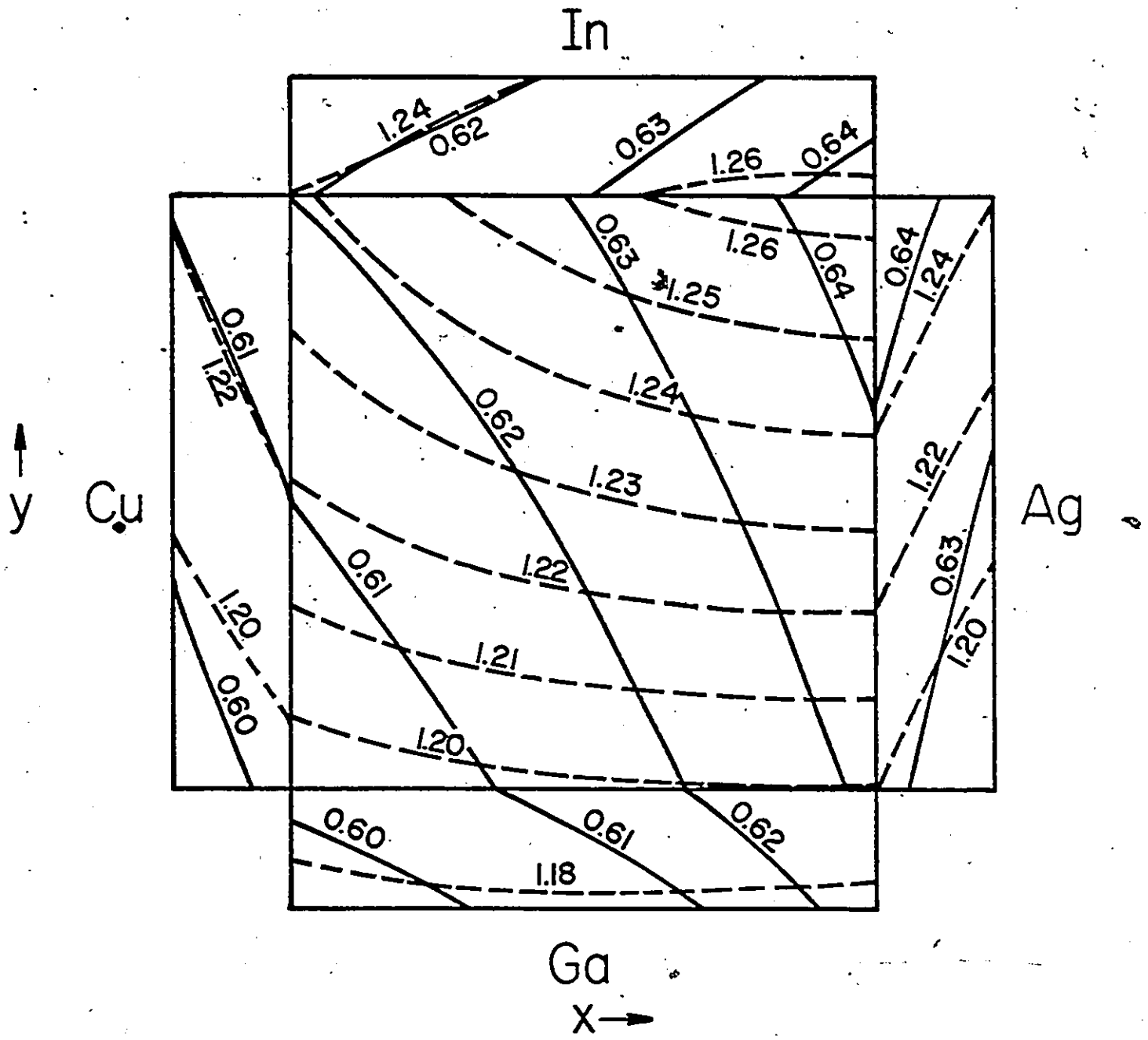

Figure 4.12 Contours of constant a (solid curves) and constant c (dashed curves) for the Te face. Also shown are constant a and c contours for sections of the faces adjacent to the Te face. (Contours are given in nm).

$$a = A + Bx + Cy + Dz + Ex^2 + Fy^2 + Gz^2 + Hxy + Iyz + Jxz$$
$$+ Kx^2y + Lxy^2 + My^2z + Nyz^2 + Ox^2z + Pxz^2 + Qxyz$$
$$+ Rx^2y^2 + Sy^2z^2 + Tx^2z^2 + Ux^2yz + Vxy^2z + Wxyz^2$$
$$+ Xx^2y^2z + Yxy^2z^2 + Zx^2yz^2 + \Sigma x^2y^2z^2 \text{ nm} . \qquad (4.3)$$

A similar equation can be written for c, with the coefficients represented using the corresponding primed notation. No attempt has been made to fit all of the data to equations of this form since this would require solving a 27 term square matrix. However, it is possible to use these equations to relate the various coefficients given in equation (4.3) and the corresponding c equation, and hence obtain averaged values for the coefficients. No simple analysis exists using the complete 27 term equation, but the averaging may be done quite simply if the final Σ or Σ' term in the equation is assumed to be zero. The method used here involves placing emphasis on the face associated with each composition variable that is thought to be the more accurate. (This will be discussed in more detail below). These are the Cu, In, and Te faces for the x, y, and z variables respectively since the Ag, Ga, and Se faces each contain miscibility gaps and have fewer data points. Thus the alloy system was temporarily rewritten as $(Cu_{1-x}Ag_x)(In_{1-y}Ga_y)(Te_{1-z}Se_z)_2$ and transformation equations were set up in order to determine the nine coefficients corresponding to each face defined in this manner. For convenience this was done in two steps by first converting to the system $(Cu_{1-x}Ag_x)(In_{1-y}Ga_y)(Se_{1-z}Te_z)_2$.

In the $(Cu_{1-x}Ag_x)(In_{1-y}Ga_y)(Se_{1-z}Te_z)_2$ system the lattice parameter variation may be written as

$$a = \alpha_o + \beta_o(1 - y) + \gamma_o z + \delta_o(1 - y)^2 + \varepsilon_o(1 - z)^2 + \zeta_o(1 - y)^2$$

$$+ \eta_o(1 - y)^2 z^2 + \theta_o(1 - y)z^2 + \lambda_o(1 - y)^2 z^2 \text{ nm} \qquad (4.4)$$

for the copper and silver faces, and

$$a = \alpha_o + \beta_o x + \gamma_o(1 - y) + \delta_o x^2 + \varepsilon_o(1 - y)^2 + \zeta_o x(1 - y)$$

$$+ \eta_o x^2(1 - y) + \theta_o(1 - y^2) + \lambda_o x^2(1 - y)^2 \text{ nm} \qquad (4.5)$$

for the selenium and tellurium faces, by replacing y by (1 - y) wherever appropriate in equation (4.1). When expanded and terms collected, equations (4.4) and (4.5) were respectively rewritten as

$$a = (\alpha_o + \beta_o + \delta_o) + (-\beta_o - 2\delta_o)y + (\gamma_o + \zeta_o + \eta_o)z + \delta_o y^2$$

$$+ (\varepsilon_o + \theta_o + \lambda_o)z^2 + (-\zeta_o - 2\eta_o)yz + \eta_o y^2 z$$

$$+ (-\theta_o - 2\lambda_o)yz^2 + \lambda_o y^2 z^2 \text{ nm} \qquad (4.6)$$

and

$$a = (\alpha_o + \gamma_o + \varepsilon_o) + (\beta_o + \zeta_o + \theta_o)x + (-\gamma_o - 2\varepsilon_o)y$$

$$+ (\delta_o + \eta_o + \lambda_o)x^2 + \varepsilon_o y^2 + (-\zeta_o - 2\theta_o)xy$$

$$+ (\eta_o - 2\lambda_o)x^2 y + \theta_o xy^2 + \lambda x^2 y^2 \text{ nm.} \qquad (4.7)$$

With the transformation equations (4.6) and (4.7) taking the form

$$a = \alpha_1 + \beta_1 u + \gamma_1 v + \delta_1 u^2 + \varepsilon_1 v^2 + \zeta_1 uv + \eta_1 u^2 v$$

$$+ \theta_1 uv^2 + \lambda_1 u^2 v^2 \text{ nm}, \qquad (4.8)$$

the values of the nine new coefficients, α_1, β_1, γ_1, etc., in the $(Cu_{1-x}Ag_x)(In_{1-y}Ga_y)(Se_{1-z}Te_z)_2$ transformed system were easily calculated using the data in table 4.6. The results are shown in Table 4.7. Also shown in the table are results using a similar analysis for the c lattice parameters, where the c lattice parameters are defined using the primed coefficients.

The second step of the analysis involved transforming from the new $(Cu_{1-x}Ag_x)(In_{1-y}Ga_y)(Se_{1-z}Te_z)_2$ system to the $(Cu_{1-x}Ag_x)(In_{1-y}Ga_y)(Te_{1-z}Se_z)_2$ system. This second transformation affects all the faces with z as a variable, i.e. the Cu, Ag, Ga, and In faces.

Following a procedure similar to the one used in the first transformation, the lattice parameter variation may be rewritten as

$$a = \alpha_1 + \beta_1 y + \gamma_1(1 - z) + \delta_1 y^2 + \varepsilon_1(1 - z)^2 + \zeta_1 y(1 - z)$$

$$+ \eta_1 y^2(1 - z) + \theta_1 y(1 - z)^2 + \lambda_1 y^2(1 - z)^2 \text{ nm} \qquad (4.9)$$

for the copper and silver faces, and

face		Cu	Ag	Se	Te
Variable composition parameters (u,v)		(y,z)	(y,z)	(x,y)	(x,y)
Lattice Constant a(nm)	α_1	0.5792	0.6102	0.5793	0.6200
	β_1	-0.0208	-0.0099	0.0201	0.0163
	γ_1	0.0324	0.0167	-0.0229	-0.0225
	δ_1	0.0036	-0.0028	0.0077	0.0089
	ε_1	0.0090	0.0184	0.0054	0.0052
	ζ_1	0.0324	0.0009	-0.0007	0.0213
	η_1	-0.0248	0.0101	0.0173	-0.0133
	θ_1	-0.0364	-0.0076	0.0126	-0.0215
	λ_1	0.0279	-0.0036	-0.0215	0.0178
Lattice Constant c(nm)	α_1	1.1573	1.1713	1.1584	1.2375
	β_1	-0.0345	-0.0924	0.0543	0.0518
	γ_1	0.0726	0.0647	-0.0376	-0.0306
	δ_1	-0.0209	0.0143	-0.0743	-0.0258
	ε_1	0.0088	0.0275	-0.0156	-0.0137
	ζ_1	0.0593	0.0619	-0.1222	-0.0527
	η_1	-0.0418	-0.0671	0.0668	0.0264
	θ_1	-0.0577	-0.0326	0.0726	0.0162
	λ_1	0.0502	0.0529	-0.0383	-0.0104

Table 4.7 Coefficients corresponding to equation (4.8) and a similar expression for the c lattice parameter for the Cu, Ag, Se, and Te faces. The coefficients are associated with the transformed system $(Cu_{1-x}Ag_x)(In_{1-y}Ga_y)(Se_{1-z}Te_z)_2$.

$$a = \alpha_o + \beta_o x + \gamma_o(1 - z) + \delta_o x^2 + \varepsilon_o(1 - z)^2 + \zeta_o x(1 - z)$$

$$+ \eta_o x^2(1 - z) + \theta_o x(1 - z)^2 + \lambda_o x^2(1 - z)^2 \text{ nm} \qquad (4.10)$$

for the gallium and indium faces, by respectively replacing z by (1 - z) in equations (4.8) and (4.1) wherever appropriate. When expanded and terms collected, equations (4.9) and (4.10) were, in turn, rewritten as

$$a = (\alpha_1 + \gamma_1 + \varepsilon_1) + (\beta_1 + \zeta_1 + \theta_1)y + (-\gamma_1 - 2\varepsilon_1)z + (\delta_1 + \eta_1 + \lambda_1)y^2$$

$$+ \varepsilon_1 z^2 + (-\zeta_1 - 2\theta_1)yz + (-\eta_1 - 2\lambda_1)y^2 z + \theta_1 yz^2 + \lambda_1 y^2 z^2 \text{ nm} \qquad (4.11)$$

and

$$a = (\alpha_o + \gamma_o + \varepsilon_o) + (\beta_o + \zeta_o + \theta_o)x + (-\gamma_o - 2\varepsilon_o)z$$

$$+ (\delta_o + \eta_o + \lambda_o)x^2 + \varepsilon_o z^2 + (-\zeta_o - 2\theta_o)xz +$$

$$+ (-\eta_o - 2\lambda_o)x^2 z + \theta_o xz^2 + \lambda_o x^2 z^2 \text{ nm} \qquad (4.12)$$

If equations (4.11) and (4.12) are expressed in the form

$$a = \alpha_2 + \beta_2 u + \gamma_2 v + \varepsilon_2 v^2 + \delta_2 uv + \eta_2 u^2 v$$

$$+ \theta_2 uv^2 + \lambda_2 u^2 v^2 \text{ nm} \qquad (4.13)$$

the coefficients α_2, β_2, γ_2 etc. and α_2', β_2', γ_2', etc. can be easily calculated using the data in Table 4.7 for the copper and silver faces, and the data in Table 4.6 for the indium and gallium faces. These results are listed in Table 4.8 and correspond to the power series coefficients in the completely transformed system $(Cu_{1-x}Ag_x)(In_{1-y}Ga_y)(Te_{1-z}Se_z)_2$. The coefficients α_1, β_1, γ_1, etc. in Table 4.7 for the selenium and tellurium faces also correspond to the completely transformed system since these faces are not affected by the change in the z variable.

The values of α_2, β_2, γ_2, etc. for the copper, silver, indium, and gallium faces may be given in terms of the coefficients A_2, B_2, C_2, etc. in the general power series expression

$$a = A_2 + B_2x + C_2y + D_2z + E_2x^2 + G_2z^2 + H_2xy + J_2yz + J_2xz$$
$$+ K_2x^2y + L_2xy^2 + M_2y^2z + N_2yz^2 + O_2x^2z + P_2xz^2$$
$$+ Q_2xyz + R_2x^2y^2 + G_2y^2z^2 + T_2x^2z^2 + U_2x^2yz + V_2xy^2z$$
$$+ W_2xyz^2 + X_2x^2y^2z + y_2xy^2z^2 + Z_2x^2yz^2 \text{ nm} \qquad (4.14)$$

for the lattice parameter variation in the $(Cu_{1-x}Ag_x)(In_{1-y}Ga_y)(Te_{1-z}Se_z)_2$ transformed system. This is done by comparing equations (4.13) and (4.14) for each of the faces given above. The results are listed in Table 4.9. A similar analysis may be carried out for the values of α_1, β_1, γ_1, etc. corresponding to the selenium and tellurium faces by comparing equations (4.8) and (4.14). These results are also given

face		Cu	Ag	Ga	In
Variable composition parameters (u,v)		(y,z)	(y,z)	(x,z)	(x,z)
Lattice Constant a(nm)	α_2	0.6206	0.6453	0.6026	0.6204
	β_2	-0.0248	-0.0166	0.0169	0.0144
	γ_2	-0.0504	-0.0535	-0.0447	-0.0508
	δ_2	0.0067	0.0037	0.0128	0.0104
	ϵ_2	0.0090	0.0184	0.0038	0.0095
	ζ_2	0.0404	0.0143	-0.0236	0.0388
	η_2	-0.0310	-0.0029	0.0283	-0.0410
	θ_2	-0.0364	-0.0076	0.0397	-0.0339
	λ_2	0.0279	-0.0036	-0.0386	0.0428
Lattice Constant c(nm)	α_2'	1.2387	1.2636	1.1937	1.2377
	β_2'	-0.0329	-0.0631	0.0185	0.0549
	γ_2'	-0.0902	-0.1197	-0.0973	-0.0892
	δ_2'	-0.0125	0.0001	-0.0139	-0.0286
	ϵ_2'	0.0088	0.0275	0.0061	0.0091
	ζ_2'	0.0561	0.0033	-0.0486	0.0472
	η_21	-0.0586	-0.0387	0.0298	-0.0807
	θ_21	-0.0577	-0.0326	0.0331	-0.0510
	λ_2'	0.0502	0.0529	-0.0268	0.0721

Table 4.8 Coefficients corresponding to equations (4.13) and a similar expression for the c lattice parameter for the Cu, Ag, Ga and In faces. The coefficients are associated with the completely transformed system $(Cu_{1-x}Ag_x)(In_{1-y}Ga_y)(Te_{1-z}Se_z)_2$.

in Table 4.9. A table similar to Table 4.9 can be constructed giving α_2', β_2', γ_2', etc. for the c parameters in terms of A_2', B_2', C_2', etc. in an equation analagous to equation (4.14). The table would be the same as for the a parameter except that all coefficients would be primed.

As aforementioned, the coefficients in the general power series equation (4.14) were determined using an averaging technique. From Table 4.9, it is evident that the A_2 coefficient may be determined directly by averaging the α values calculated using the transformations, for the Cu, In, and Te faces. Similarly, the B_2 coefficient may be calculated by averaging the β values for the In and Te faces. Thus, by continuing in this manner, by simply averaging, the coefficients A_2 through G_2 were calculated. The values of H_2 through P_2 and R_2, S_2, and T_2 were taken directly from the table as these only occurred once as coefficients in the Cu, In, and Te variations. Thus the remaining coefficients, Q_2 and U_2 through Z_2, were calculated from the values determined from the Ag, Ga, and Se faces making use of the parameters already obtained from the Cu, In, and Te faces. The resulting values were averaged whenever the coefficients were determined from more than one calculation. It should be noted here that if the transformation to the new system, $(Cu_{1-x}Ag_x)(In_{1-y}Ga_y)(Te_{1-z}Se_z)_2$ were not made, then emphasis would have been placed on the Cu, Ga, and Se faces. Thus A_2 through T_2, excluding Q_2, would have essentially been calculated from the less reliable faces.

face	Cu	Ag	Ga	In	Se	Te
Variable composition parameter (u,v)	(y,z)	(y,z)	(x,z)	(x,z)	(x,y)	(x,y)
i	2	2	2	2	1	1
α_i	A_2	$A_2+B_2+E_2$	$A_2+C_2+F_2$	A_2	$A_2+D_2+G_2$	A_2
β_i	C_2	$C_2+H_2+K_2$	$B_2+H_2+L_2$	B_2	$B_2+J_2+P_2$	B_2
γ_i	D_2	$D_2+J_2+O_2$	$D_2+I_2+M_2$	D_2	$C_2+I_2+N_2$	C_2
δ_i	F_2	$F_2+L_2+R_2$	$E_2+K_2+R_2$	E_2	$E_2+O_2+T_2$	E_2
ϵ_i	G_2	$G_2+P_2+T_2$	$G_2+N_2+S_2$	G_2	$F_2+M_2+S_2$	F_2
ζ_i	I_2	$I_2+Q_2+U_2$	$J_2+Q_2+V_2$	J_2	$H_2+Q_2+W_2$	H_2
η_i	M_2	$M_2+V_2+X_2$	$O_2+U_2+X_2$	O_2	$K_2+U_2+Z_2$	K_2
θ_i	N_2	$N_2+W_2+Z_2$	$P_2+W_2+Y_2$	P_2	$L_2+V_2+Y_2$	L_2
λ_i	S_2	S_2+Y_2	T_2+Z_2	T_2	R_2+X_2	R_2

Table 4.9 Relationship between coefficients of equation (4.13) for the Cu, Ag, In, and Ga faces and equation (4,8) for the Se and Te faces describing the variation of the lattice parameter a in the completely transformed system, and the coefficients of the general equation (4.14).

NEXT

FICHE

SUIVANTE

The variation of a and c for the transformed system, $(Cu_{1-x}Ag_x)(In_{1-y}Ga_y)(Te_{1-z}Se_z)_2$, were found in this manner to be given by

$$a = 0.6203 + 0.0154x - 0.0237y - 0.0506z + 0.0097x^2 + 0.0060y^2$$
$$+0.0093z^2 + 0.0213xy + 0.0404yz + 0.0388xz$$
$$- 0.0133x^2y - 0.0215xy^2 - 0.0310y^2z - 0.0364yz^2$$
$$- 0.0410x^2z - 0.0339xz^2 - 0.1317xyz + 0.0178x^2y^2$$
$$+ 0.0279y^2z^2 + 0.0428x^2z^2 + 0.1056x^2yz + 0.0693xy^2z$$
$$+ 0.1097xyz^2 - 0.0388x^2y^2z - 0.0357xy^2z^2$$
$$- 0.0780x^2y^2z^2 \text{ nm} \qquad (4.15)$$

and

$$c = 1.2380 + 0.534x - 0.0318y - 0.0897z - 0.0272x^2 - 0.0131y^2$$
$$+ 0.0090z^2 - 0.0527xy + 0.0561yz + 0.472xz$$
$$+ 0.0264x^2y + 0.0162xy^2 - 0.0586y^2z - 0.0577yz^2$$
$$- 0.0807x^2z - 0.0510xz^2 - 0.1701xyz - 0.0104x^2y^2$$
$$- 0.0502y^2z^2 + 0.0721x^2z^2 + 0.1173x^2yz$$
$$+ 0.0743xy^2z + 0.1006xyz^2 - 0.0306x^2y^2z$$
$$- 0.0172xy^2z^2 - 0.0762x^2yz^2 \text{ nm.} \qquad (4.16)$$

Reverse transformations were performed giving the variation (4.3) and a similar c variation for the variables x, y, and z defined in the original system, $(Cu_{1-x}Ag_x)(Ga_{1-y}In_y)(Se_{1-z}Te_z)_2$. The final results are given below

$$\begin{aligned} a = {} & 0.5622 + 0.0317x + 0.0139y + 0.0396z + 0.0048x^2 + 0.0029y^2 \\ & + 0.0008z^2 - 0.0235xy + 0.0172yz - 0.0566xz \\ & + 0.0277x^2y + 0.0121xy^2 - 0.0248y^2z - 0.0194yz^2 \\ & + 0.0446x^2z + 0.0401xz^2 + 0.0835xyz - 0.0210x^2y^2 \\ & + 0.0279y^2z^2 - 0.0352x^2z^2 - 0.1280x^2yz \\ & + 0.0021xy^2z - 0.0383xyz^2 + 0.388x^2y^2z - 0.0357xy^2z \\ & + 0.0780x^2yz^2 \text{ nm} \end{aligned} \qquad (4.17)$$

and

$$\begin{aligned} c = {} & 1.1024 + 0.0007x + 0.0764y + 0.0892z - 0.0093x^2 \\ & - 0.0215y^2 + 0.0015z^2 - 0.0244xy + 0.0243yz \\ & - 0.0162xz + 0.0145x^2y + 0.0733xy^2 + 0.1109xyz \\ & - 0.0410x^2y^2 + 0.0502y^2z^2 - 0.0041x^2z^2 - 0.0963x^2yz \\ & - 0.0399xy^2z - 0.0662xyz^2 + 0.0306x^2y^2z - 0.0172xy^2z^2 \\ & + 0.0762x^2yz^2 \text{ nm.} \end{aligned} \qquad (4.18)$$

The averaged coefficient equations (4.17) and (4.18) were used to fit the data of each of the six faces. It was found that the use of these averaged values made only a small difference to the fitted curves in figures 4.1 through 4.6 with the overall standard deviations being 0.0015nm for a and 0.0023nm for c. The worst fits occurred

in the case of the tellurium face. These are plotted in figures 4.6(a) and 4.6(c), corresponding to the dashed lines. The deviation from the original fitting curve is relatively small, however, even in this extreme case; and thus the 'averaged' curves, either as curves of a or c vs. u etc. or for contours of constant a and c, have not been shown for the remaining faces. The averaged values in equations (4.17) and (4.18) will be used further in the analysis of the data for the compositions investigated inside the cube.

As discussed in the introduction, the energy gap or lattice parameter value for alloys with a single variable, such as the $Ga_{1-x}In_xAs$ alloys, can be very useful for determining the compositions of the alloy sample (section 1.1). However, in the case of cubic alloys with two composition variables, e.g. $Ga_{1-x}In_xAs_{1-y}P_y$ alloys, this cannot be done because a single lattice parameter cannot define both composition variables. In the case of tetragonal alloys, when two lattice parameter values, a and c, are obtained, the values of two composition variables can be determined under favourable circumstances. This requires that contours of constant a and constant c intersect at a fairly large angle. Thus in the diagrams shown in figures 4.7 to 4.12 the gallium, selenium, and tellurium faces satisfy this condition very well. One half of the indium face is also satisfactory, while with the silver face it may also be possible. For the remaining half of the indium face and the entire copper face, the a and c contours either do not intersect or intersect at small angles and are therefore not useful in determining alloy compositions.

It should be noted that the above situation, whereby two alloy composition variables may be determined from contours of constant a and c, is only possible for compositions on the faces. Alloy compositions within the interior of the cube have three composition

variables. Thus, once again the lattice parameter gives insufficient data to determine the composition.

4.2 Lattice Constant Results for Compositions Inside the Cube and the Range of Solid Solution

In addition to investigating the lattice parameter variation on the surface of the cube, all samples were investigated having compositions x, y, and z equal to 0.25, 0.50, and 0.75. Using the same identification method described in section 4.1, these samples are listed in Table 4.10 with the experimentally determined values of lattice parameter. Also listed are the interpolated values of a and c determined using the averaged coefficient, general equations (4.17) and (4.18).

As can be seen in the table, several of the samples were found to be two or multiphase, the criterion being apparent 'errors' in the values of a and c as predicted from curves similar to those of figures 4.1–4.6; and the detection of diffraction lines due to a second phase in the x-ray powder photographs. (This has been discussed in more detail in section 4.1). Thus the multiphase region, as well as affecting the silver, gallium, and selenium faces, extends over quite a large region in the center of the cube. Eleven out of the twenty-seven compositions investigated in the central region were, in fact, found to be multiphse. Figure 4.13 indicates the multiphase samples investigated in various sections of the cube. As can be seen from the figure, much of the $z = 0$, $z = 0.25$ planes consist of multiphase material. The $z = 0.50$ plane also was found to contain multiphase material, whereas the $z = 0.75$ plane (not shown) was single phase throughout.

Sample	Experimental Values		Predicted Values	
	a(nm)	c(nm)	a(nm)	c(nm)
252525	multiphase			
252550	multiphase			
252575	0.5973	1.1784	0.6011	1.1889
255025	multiphase			
255050	0.5938	1.1780	0.5957	1.1825
255075	0.6084	1.2144	0.6056	1.2044
257525	0.5829	1.1716	0.5901	1.1748
257550	0.6002	1.1965	0.5999	1.1966
257575	0.6139	1.2146	0.6099	1.2178
502525	multiphase			
502550	multiphase			
502575	0.6055	1.1857	0.6074	1.1897
505025	multiphase			
505050	multiphase			
505075	0.6112	1.2040	0.6119	1.2068
507525	0.5941	1.1760	0.5971	1.1771
507550	0.6054	1.1960	0.6064	1.1999
507575	0.6157	1.2191	0.6161	1.2224
752525	multiphase			
752550	multiphase			
752575	0.6153	1.1280	0.6154	1.1886
755025	multiphase			
755050	0.6019	1.1674	0.6099	1.1811
755075	0.6189	1.2036	0.6192	1.2065
757525	multiphase			
757550	0.6089	1.1909	0.6135	1.1989
757575	0.6224	1.2202	0.6230	1.2231

Table 4.10 Values of a and c from experiment and by prediction using the averaged parameter equations for compositions x, y, and z equal to 0.25, 0.50, and 0.75. Multiphase samples are also indicated.

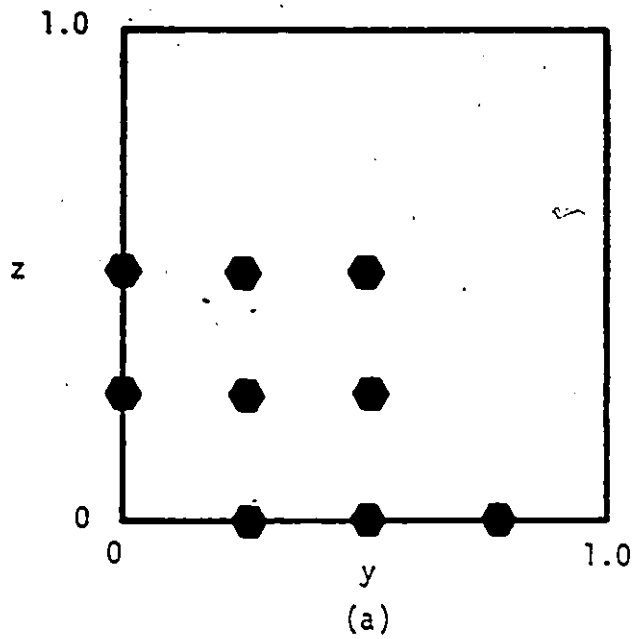

(a)

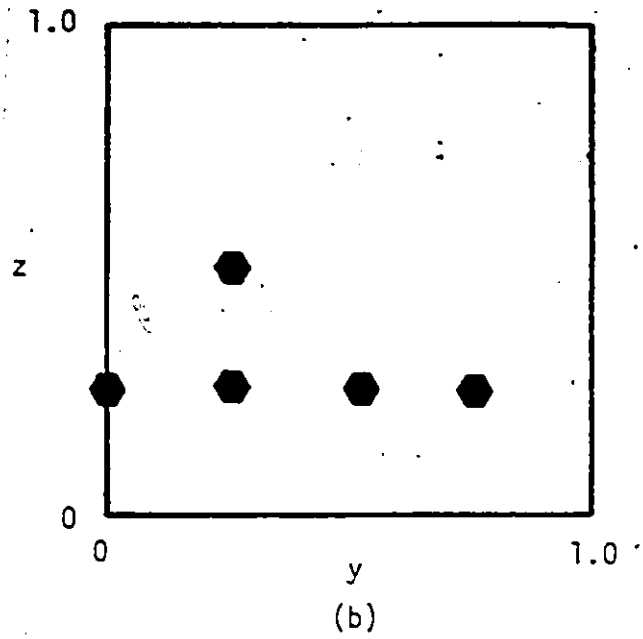

(b)

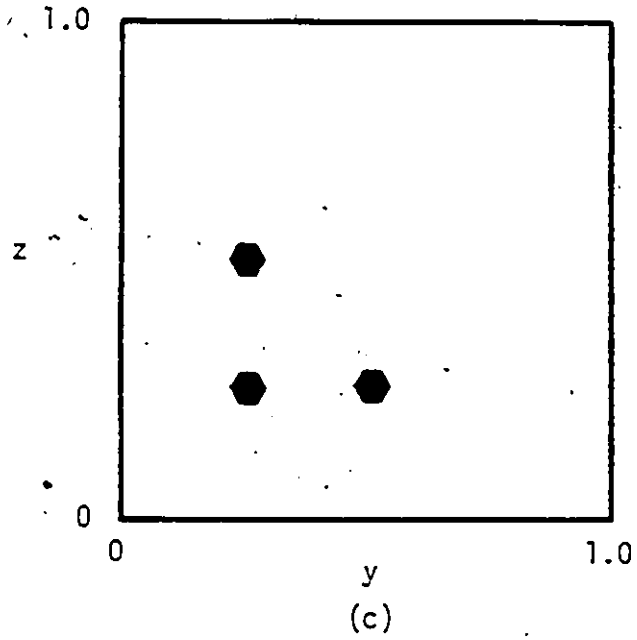

(c)

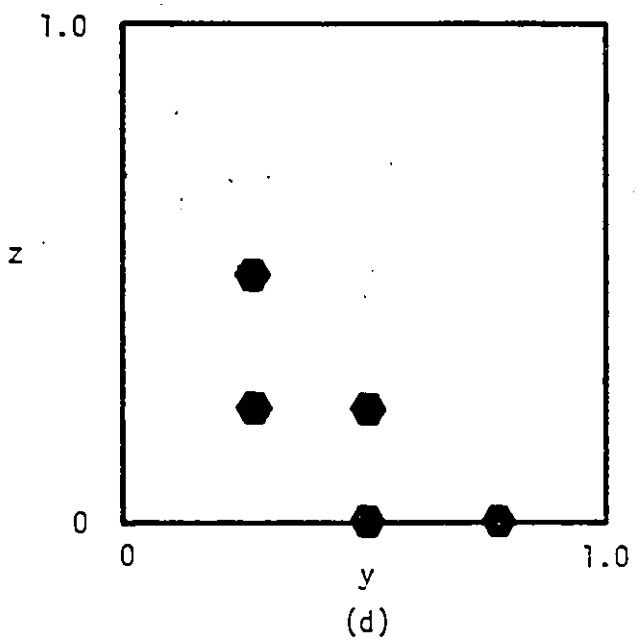

(d)

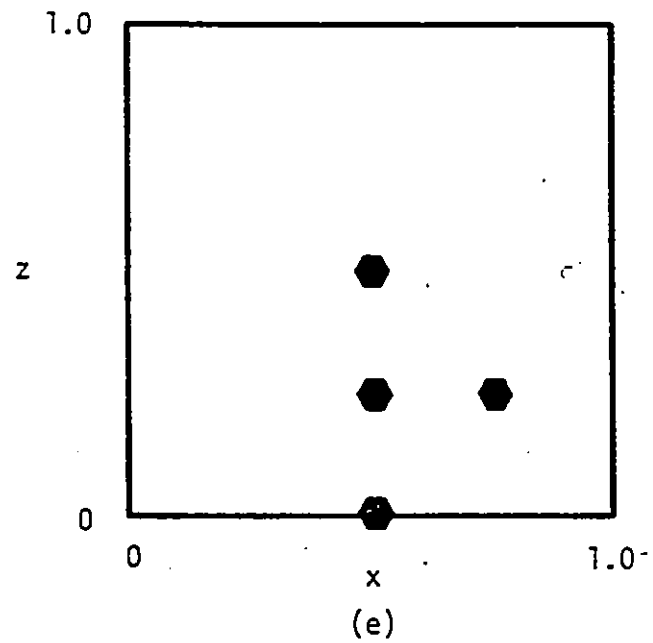

(e)

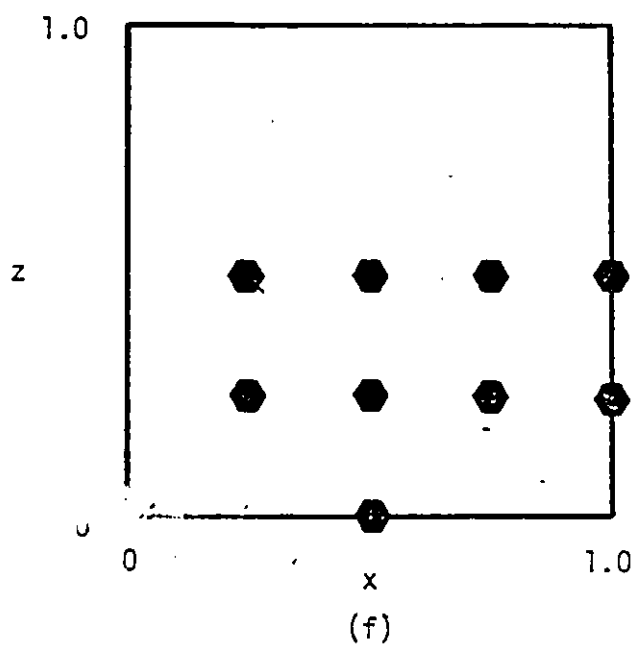

(f)

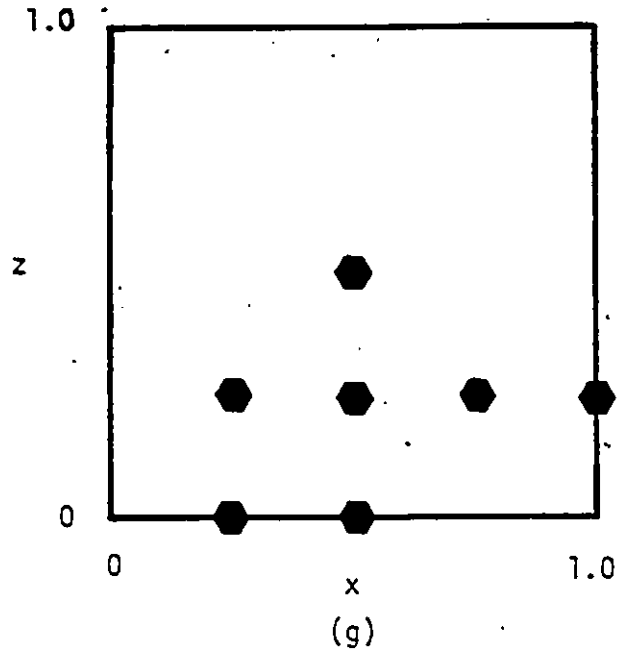

(g)

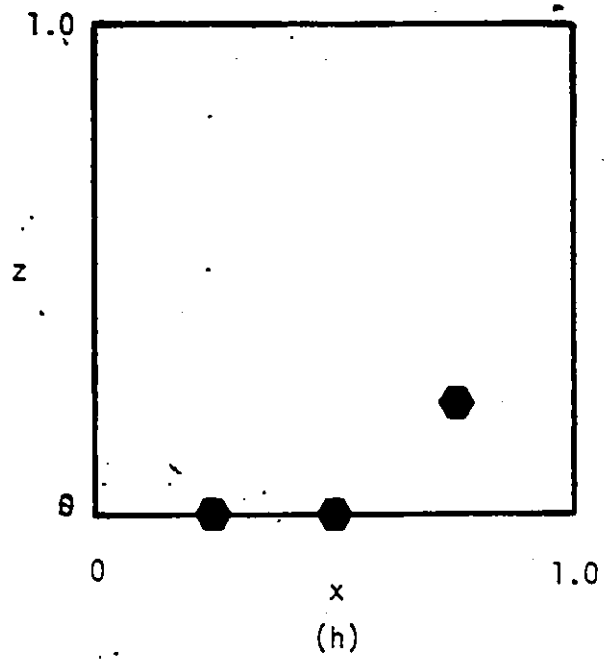

(h)

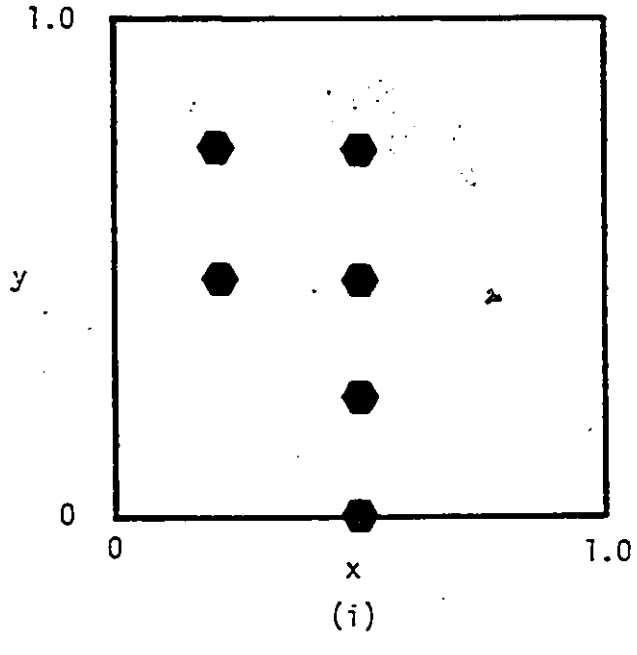

(i)

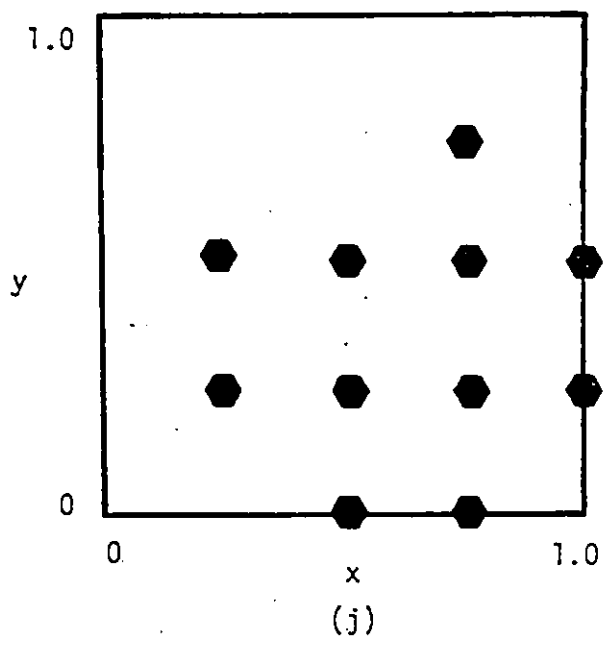

(j)

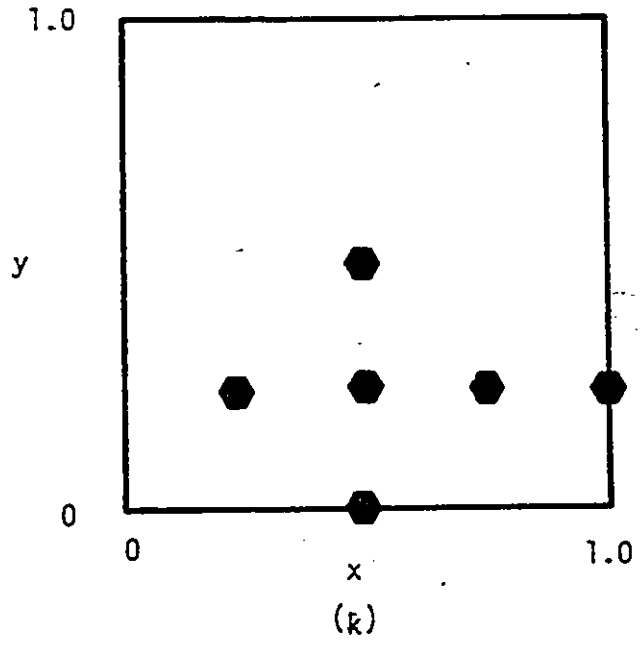

(k)

Figure 4.13 Compositions (⬢) found to be multiphase in various sections of the cube: (a) x=0.50, (b) x=0.75, (c) x=1.0, (d) x=0.25, (e) y=0, (f) y=0.25, (g) y=0.50, (h) y=0.75, (i) z=0, (j) z=0.25, (k) z=0.50.

An estimated region of the cube in which there is a miscibility gap is shown in figure 4.14. The exact boundaries of this region are uncertain for reasons previously discussed. Very detailed analysis, well beyond the scope of this thesis, is required to obtain more accurate information.

Graphs have been drawn showing the lattice parameter variation with composition for various sections having appreciable single phase range. These graphs, for planes x = 0.25, y = 0.75, and z = 0.75, are illustrated in figures 4.15 to 4.17, and show both the experimental points for single phase compositions and solid curves obtained from the averaged equations (4.17) and (4.18). As seen from the curves, the fit to the interior points is consistently worse than the fit to the points corresponding to a cube edge on each graph. The standard deviations for a and c were found to be 0.0029 nm and 0.0059 nm respectively in this case. These are considerably greater than the standard deviations of the fit to the faces listed in Table 4.6. This is partially due to the experimental scatter discussed in section 4.1. In addition, however, it is also apparent that there is some degree of systematic variation, with the experimental points in many cases falling below the fitted curves. A general fit using equation (4.3) to all the experimental points together, including surface and interior points, would improve the fit to the interior points but worsen the fit to the faces. This general fit would require the solution of a 26 x 26 square matrix, and is not plausible in the present analysis.

Using the averaged fitting equations, the standard deviation for all points in the system was calculated to be 0.0015 nm and 0.0029 nm for the a and c parameters respectively. These values are

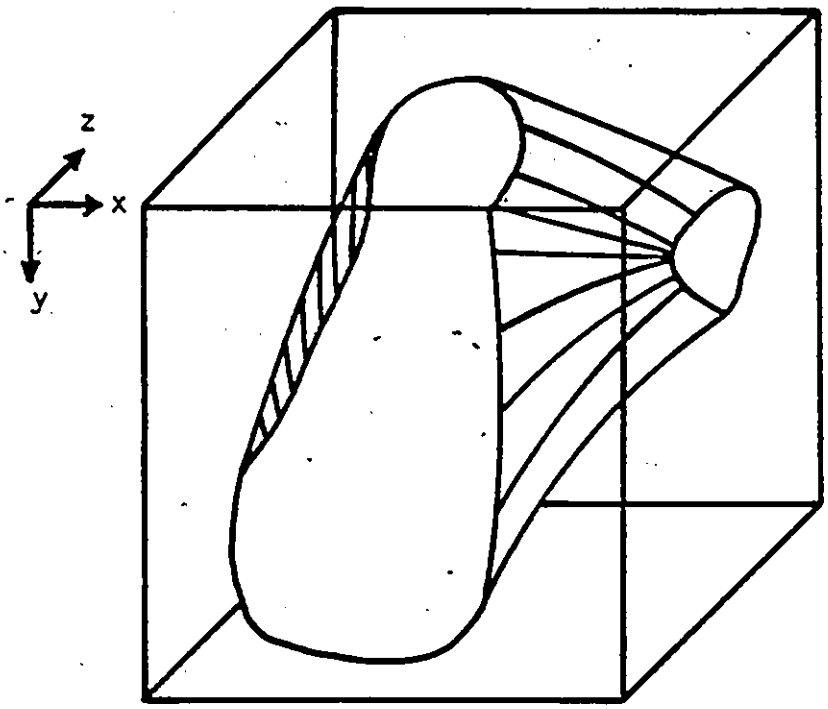

Figure 4.14 Estimated region of the cube showing multiphase behavior.

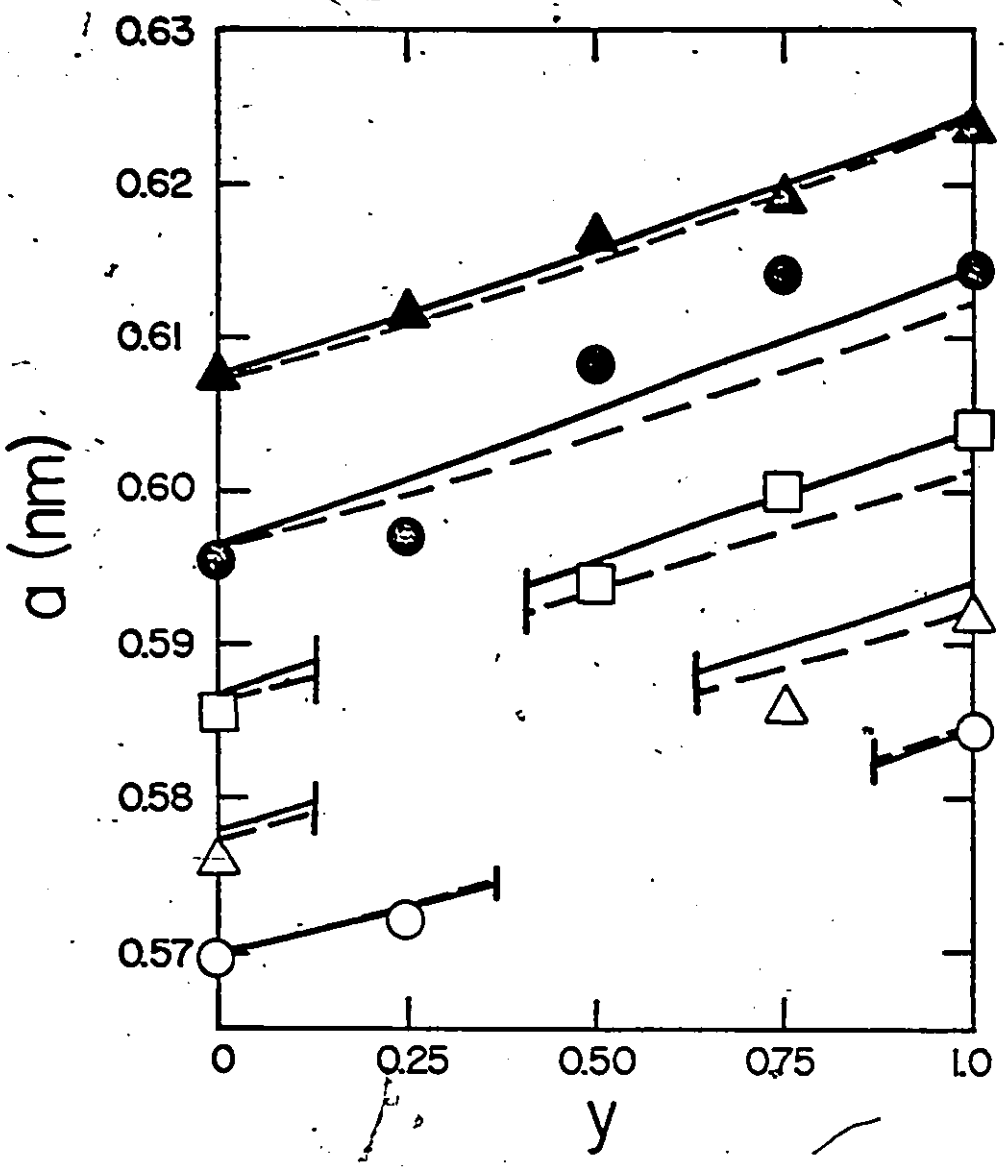

Figure 4.15(a) Variations of lattice parameter a for the x = 0.25 plane as a function of y at various constant values of z. Solid lines indicate the curves predicted by the average parameter equation. Dashed lines correspond to the three-dimensional equation derived from the Moon et al interpolation equation (section 6.5).
z = 0 ○, z = 0.25 △, z = 0.50 □, z = 0.75 ●, z = 1.0 ▲

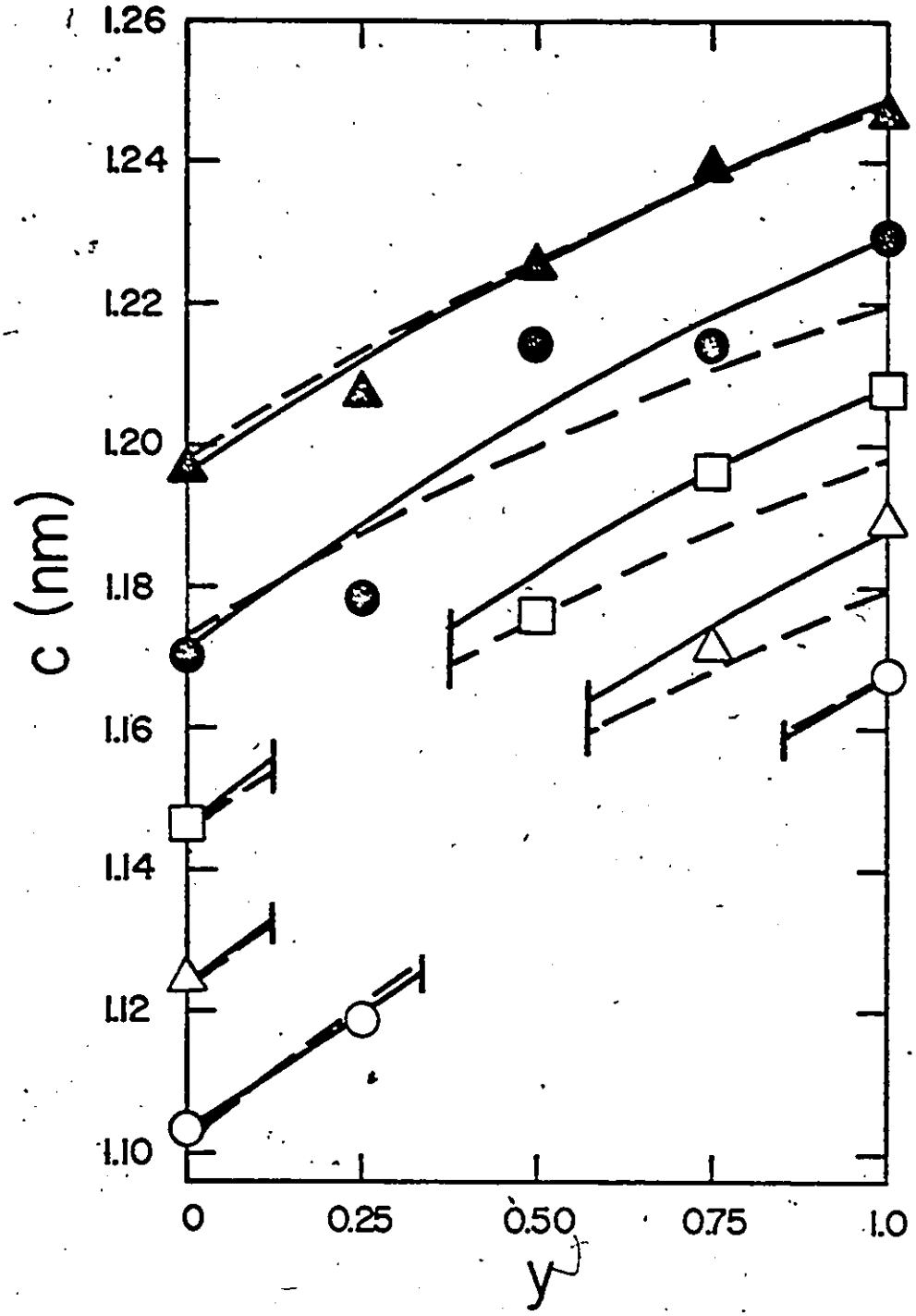

Figure 4.15(b) Variations of lattice parameter c for the x = 0.25 plane as a function of y at various constant values of z. Solid lines indicate the curves predicted by the average parameter equation. Dashed lines correspond to the three-dimensional equation derived from the Moon et al interpolation equation (section 6.5).
z = 0 ○, z = 0.25 △, z = 0.50 □, z = 0.75 ●, z = 1.0 ▲

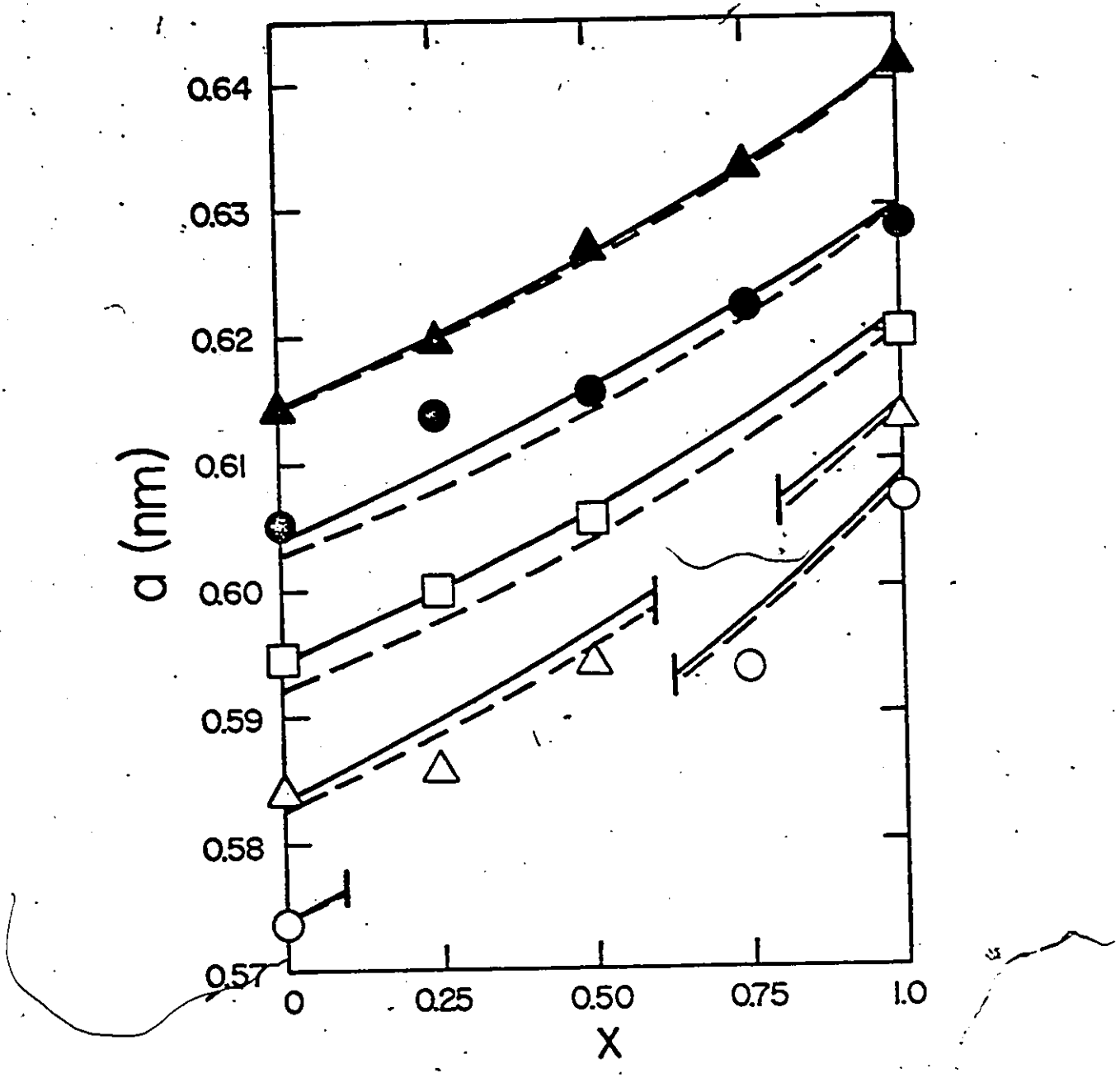

Figure 4.16(a) Variations of lattice parameter a for the y = 0.75 plane as a function of x at various constant values of z. Solid lines indicate the curves predicted by the average parameter equation. Dashed lines correspond to the three-dimensional equation derived from the Moon et al interpolation equation (section 6.5).
z = 0○, z = 0.25△, z = 0.50□, z = 0.75●, z = 1.0▲

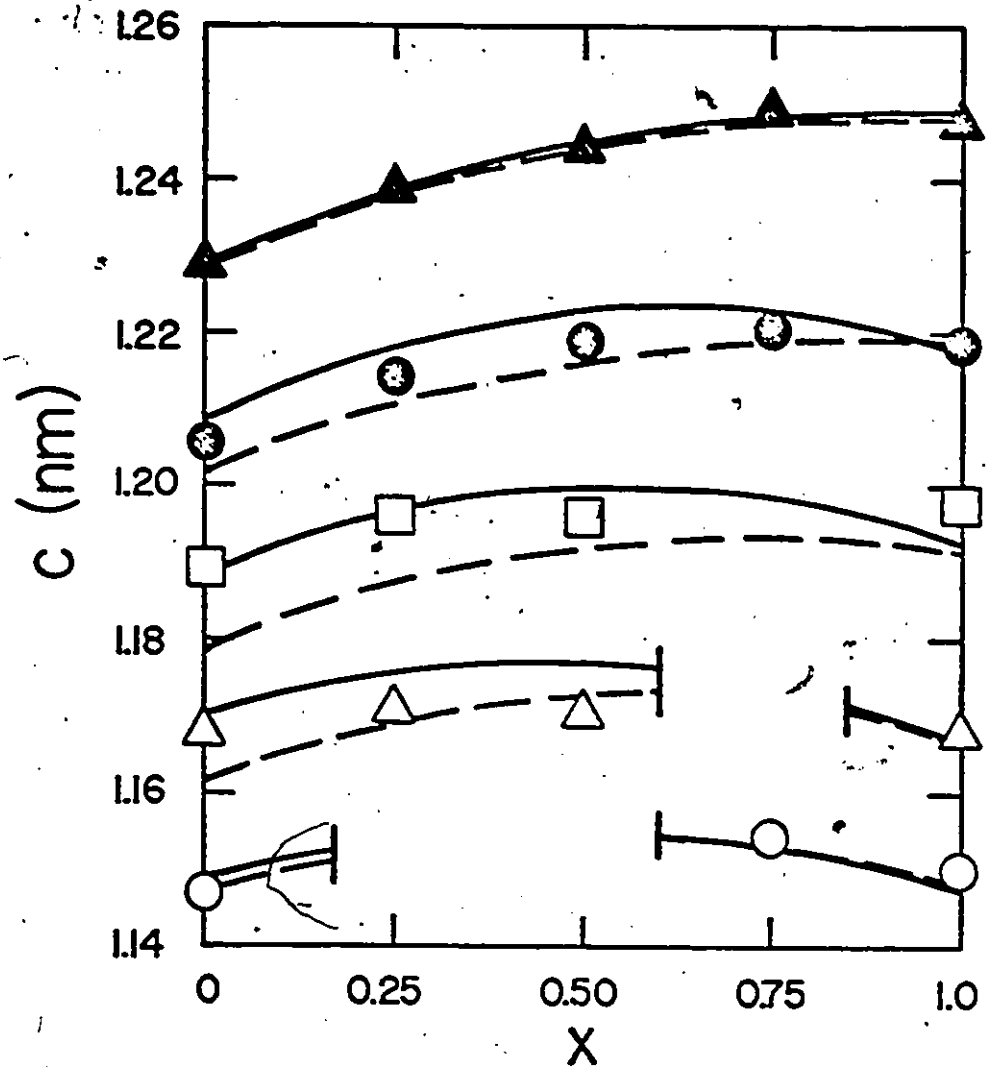

Figure 4.16(b) Variations of lattice parameter c for the y = 0.75 plane as a function of x at various constant values of z. Solid lines indicate the curves predicted by the average parameter equation. Dashed lines correspond to the three-dimensional equation derived from the Moon et al interpolation equation (section 6.5).
z = 0○, z = 0.25△, z = 0.50□, z = 0.75●, z = 1.0▲

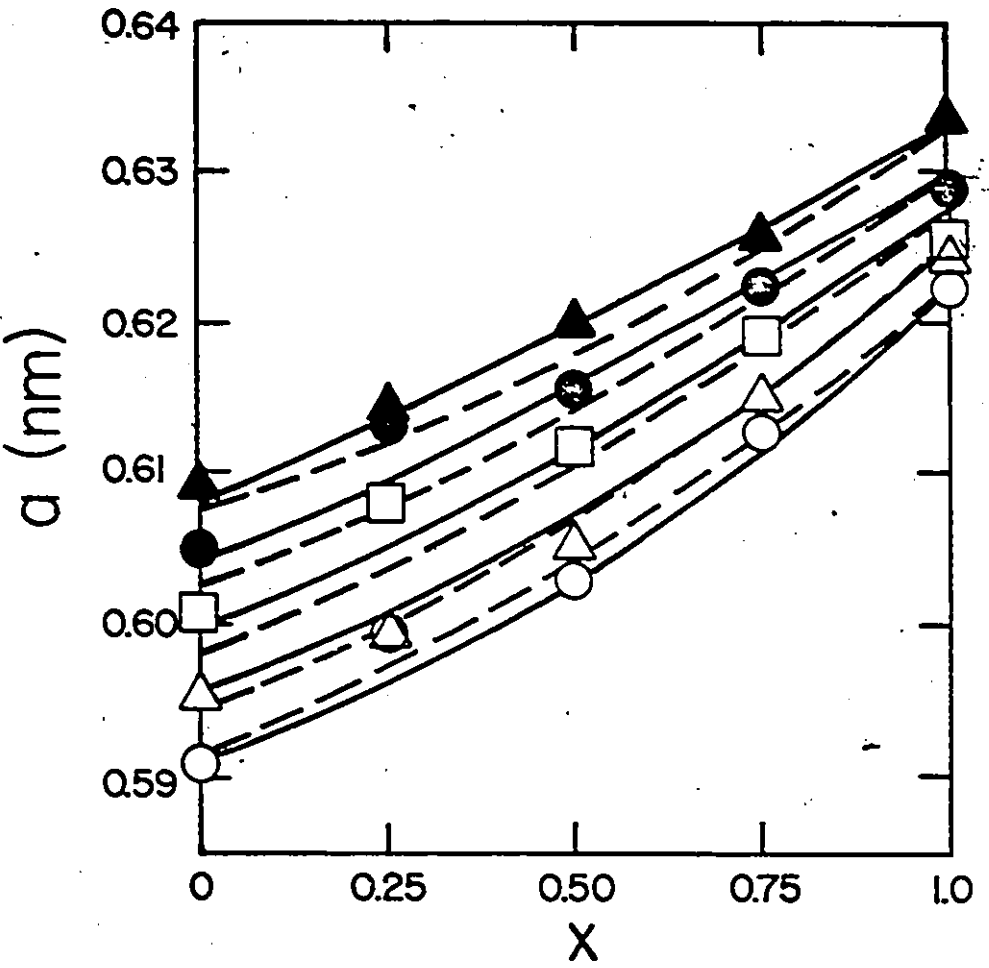

Figure 4.17(a) Variations of lattice parameter a for the z = 0.75 plane as a function of x at various constant values of y. Solid lines indicate the curves predicted by the average parameter equation. Dashed lines correspond to the three-dimensional equation derived from the Moon et al interpolation equation (section 6.5). y = 0 ○, y = 0.25 △, y = 0.50 □, y = 0.75 ●, y = 1.0 ▲

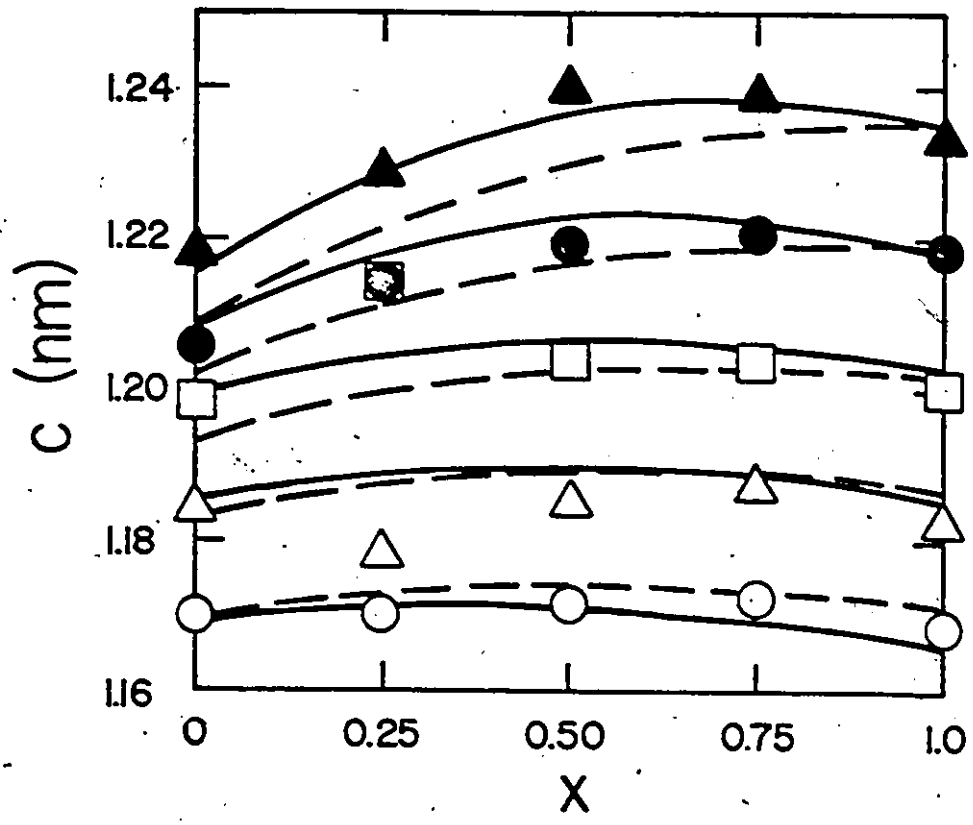

Figure 4.17(b) Variations of lattice parameter c for the z = 0.75 plane as a function of x at various constant values of y. Solid lines indicate the curves predicted by the average parameter equation. Dashed lines correspond to the three-dimensional equation derived from the Moon et al interpolation equation (section 6.5). y = 0 ○, y = 0.25 △, y = 0.50 □, y = 0.75 ●, y = 1.0 ▲

useful for comparison with another interpolation method to be discussed in Chapter VI.

4.3 Summary

Lattice parameter values were calculated for $(Cu_{1-x}Ag_x)(Ga_{1-y}In_y)(Se_{1-z}Te_z)_2$ alloys throughout the cubic composition range. Single phase solid solution was found throughout all the faces except the gallium, silver, and selenium faces. Here, as well as in much of the interior of the cube, multiphase behavior was found.

Curves showing the variation of a and c as a function of composition were plotted for each face. Fitting was done separately to each face using a nine term power series expression. Small standard deviations were calculated indicating that deviations were mainly the result of scatter. The fitting equations were used to give contours of constant a and c, which were plotted for each of the faces. In a general three-dimensional analysis, the power series fits to each face were used to determine the coefficients of a 26 term power series using an averaging method. When plotted, the curves corresponding to the resulting expression were found to essentially coincide with the power series fits to each face. Thus only the tellurium face curves, which were slightly different, are shown.

In addition to considering the lattice parameter variation on the faces, similar graphs were plotted for interior planes having single phase solid solution over most of the composition range. Experimental points were compared to curves using the 26 term averaged coefficient expression. Systematic deviations from the curves were

evident indicating that the power series expression would need to be extended to give a better fit.

The standard deviation of all the experimental points was calculated for the averaged fit. This was found to be σ_a = 0.0015 nm and σ_c = 0.0023 nm and will be used for comparison with interpolation method results to be discussed in Chapter VI.

CHAPTER V - ENERGY GAP RESULTS AND FITTING

5.1 Experimental Results and Fitting

As in the case of lattice parameter measurements, energy gaps were investigated for many of the alloys $(Cu_{1-x}Ag_x)(Ga_{1-y}In_y)(Se_{1-z}Te_z)_2$ with x, y, and z having values 0, 0.25, 0.5, 0.75, and 1.0, excluding those found to be multiphase (see sections 4.1 and 4.2). The methods used are described in Chapter III. It was not possible, however, to obtain energy gap values for many of the samples investigated owing to several factors. In many cases the condition of the sample was such that sufficiently thin samples could not be prepared for absorption without breakage first occurring. For these samples energy gaps were investigated using the photoacoustic technique, since with this method, powdered samples can be used. However, problems also arose with the photoacoustic method in that several of the PA spectra were relatively flat and did not peak near the frequency corresponding to the energy gap. Figure 5.1 shows PA curves for the 101010, 102510, and 255010 compositions (see section 4.1 for explanation of identification scheme) where the signal intensities behave as expected, distinctly increasing and then remaining constant as hν increases. Figure 5.2, however, shows the PA spectrum for the 757510 composition. It can be clearly seen that in this case, it is impossible to determine the energy gap value from the criterion discussed in section 3.6 since the curve never distinctly peaks. Thus for samples characterized by this behavior and the inability to polish to thicknesses sufficient for absorption, energy gap values were not determined. It should be noted, however, that whenever possible, absorption measurements were made

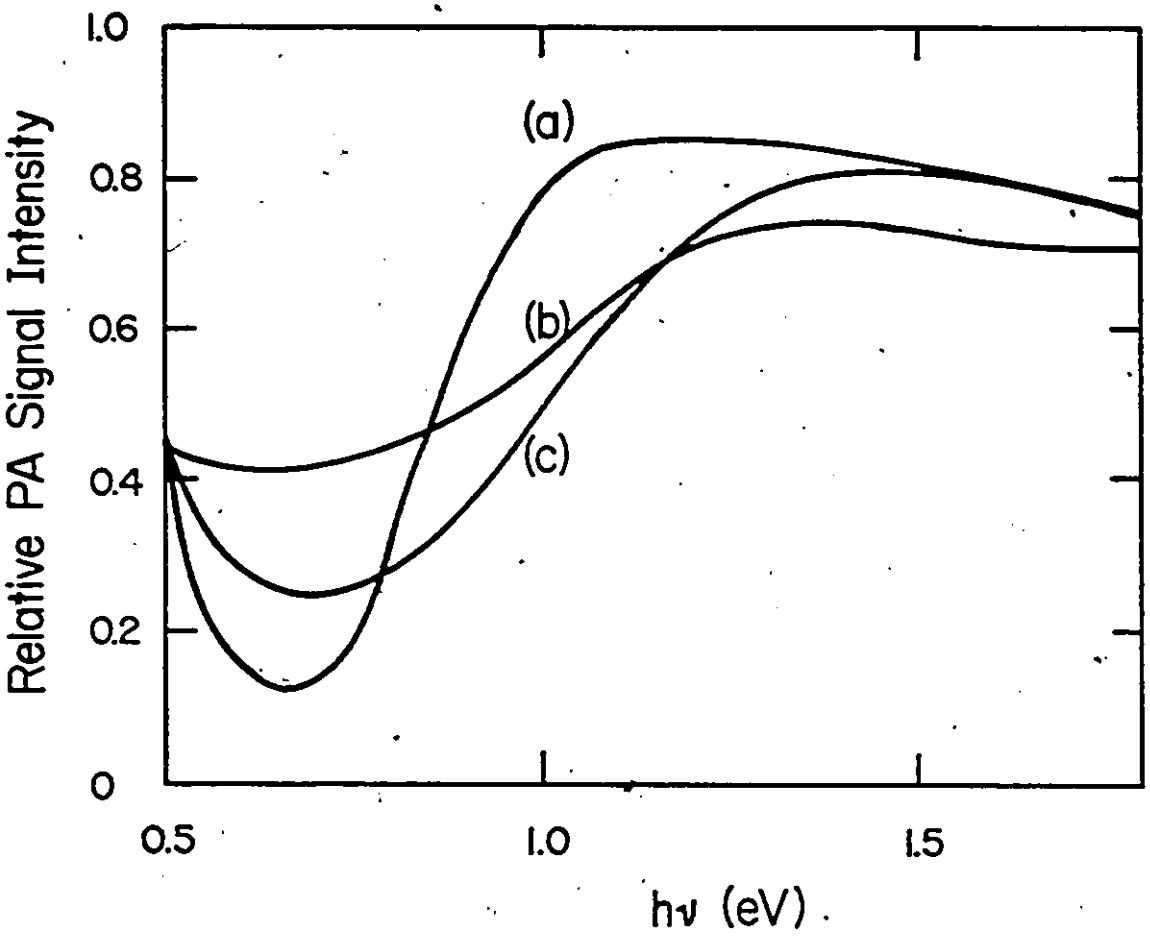

Figure 5.1 PA curves for compositions (a) 101010, (b) 255010, and (c) 102510.

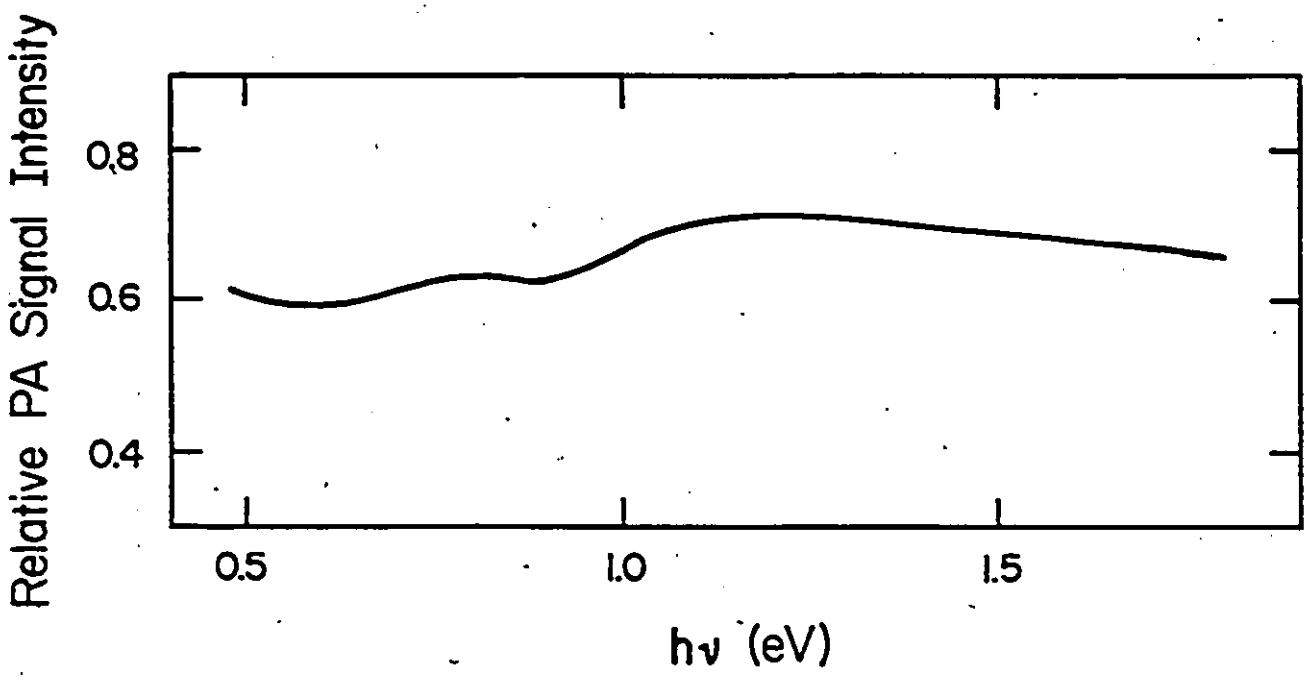

Figure 5.2 PA curve for composition 757510. The curve never distinctly peaks.

rather than photoacoustic measurements since the former method involves a more reliable technique.

Another problem encountered in absorption measurements was the occurrence of high background absorption. This was the main difficulty in determining energy gap values for the tellurium face. Results for the compounds have shown that a range of compositions occurs for these samples (75S1). In these instances, using the melt and anneal technique described in section 2.1, it is possible to obtain a slight excess of tellurium. The excess tellurium can act as a donor, giving large electron concentrations, and thus be a factor which could account for high background absorption. A solution to this problem would involve a detailed investigation of possible composition variation in these materials.

When absorption measurements were successful, curves similar to those in figures 5.3(a) and 5.4(a) were obtained. These graphs show the variation of the apparent absorption coefficient, α, as a function of energy, $h\nu$, where $\alpha = -\frac{1}{d} \ell n(\frac{I_0}{I_T})$ (see equation (3.3.)) and d, I_0, and I_T represent the thickness of the sample, and the incident and transmitted light intensities respectively. Typically α varied from about 0.035 - 0.070 μm^{-1} for samples ranging in thickness 150 - 200 μm. Figure 5.3(a) shows the absorption spectrum for $(Cu_{0.25}Ag_{0.75})GaTe_2$ (750010). In the calculation of α, a straight line extrapolation of the background absorption, α_o, as indicated in the figure, was subtracted from the measured value of $\frac{1}{d} \ell n(\frac{I_0}{I_T})$ to give the required values of α. Figure 5.4(a) shows the absorption spectrum for $(Cu_{0-5}Ag_{0.5})GaTe_2$ (500010). In this case it can be seen that at low energies scattering effects are present with $\frac{1}{d} \ell n(\frac{I_0}{I_T})$ increasing

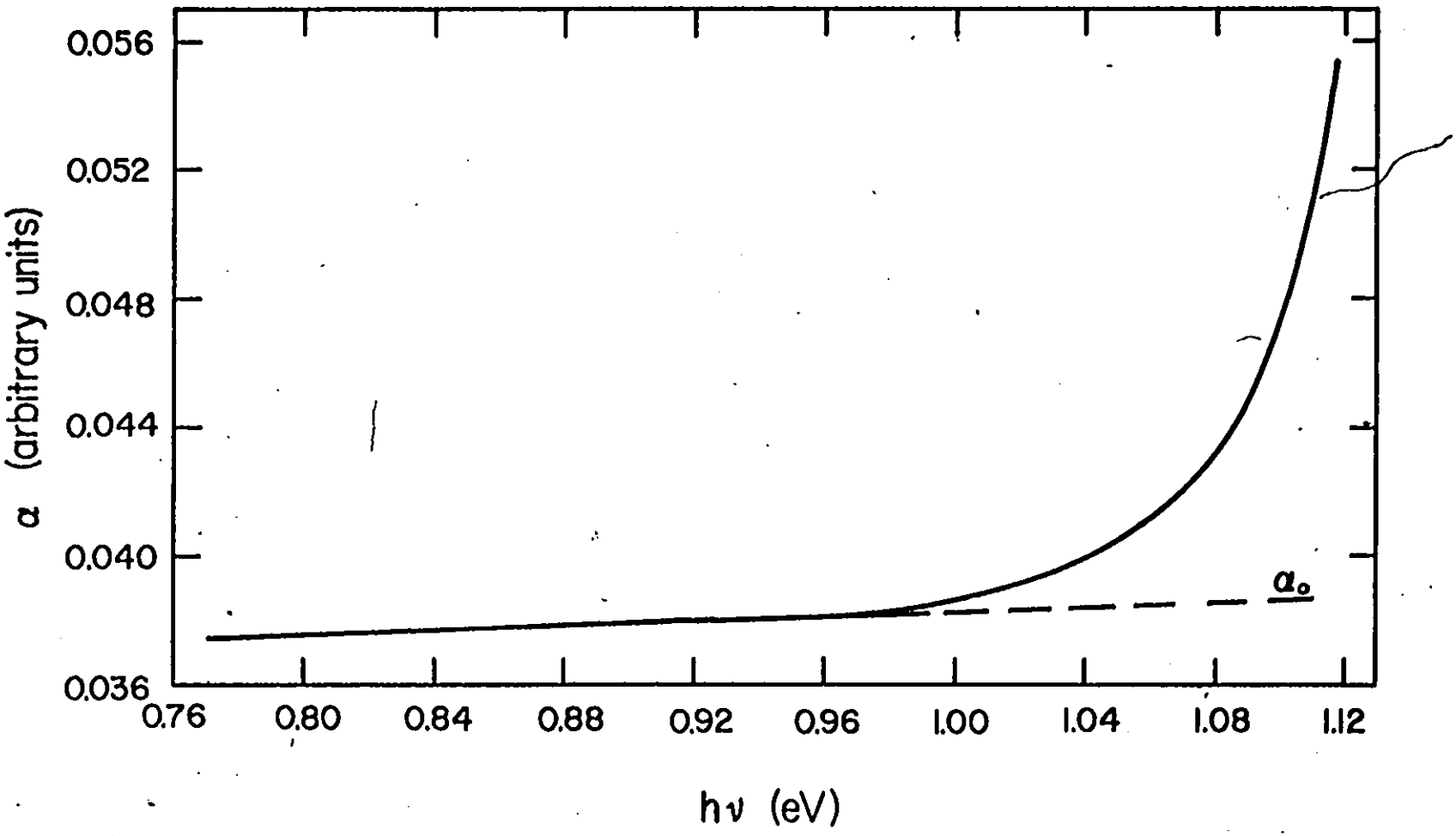

Figure 5.3(a) Absorption spectrum for $(Cu_{0.25}Ag_{0.75})GaTe_2$(750010). A straight line extrapolation of the background absorption, α_o, was used to determine values of α.

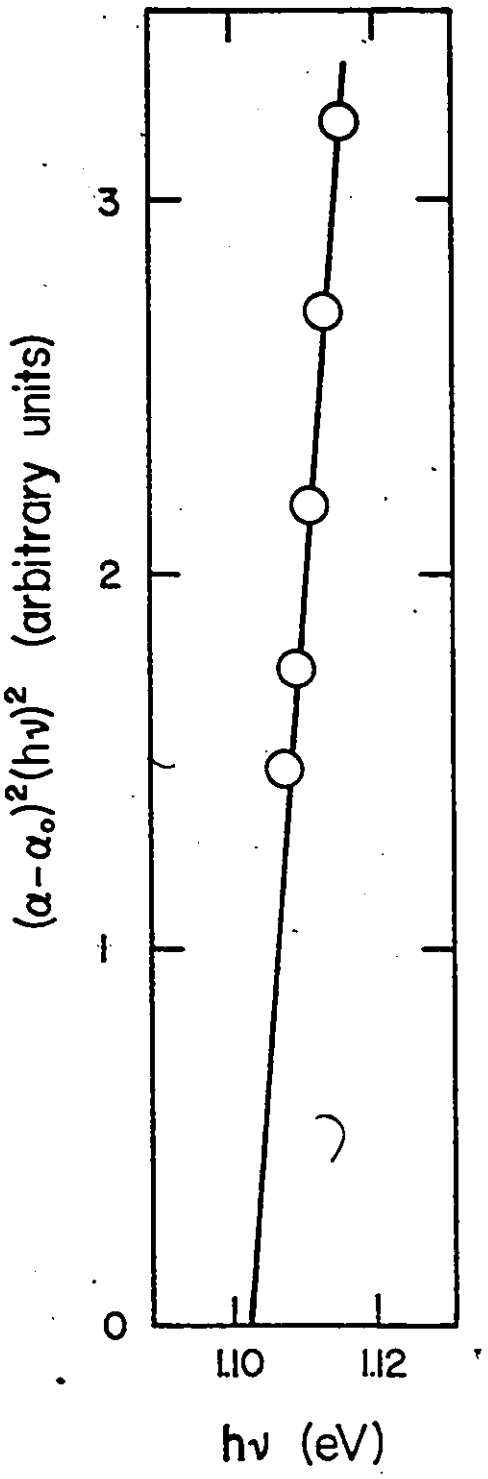

Figure 5.3(b) The straight line variation of $(\alpha - \alpha_o)^2(h\nu)^2$ versus hν for $(Cu_{0.25}Ag_{0.75})GaTe_2$.

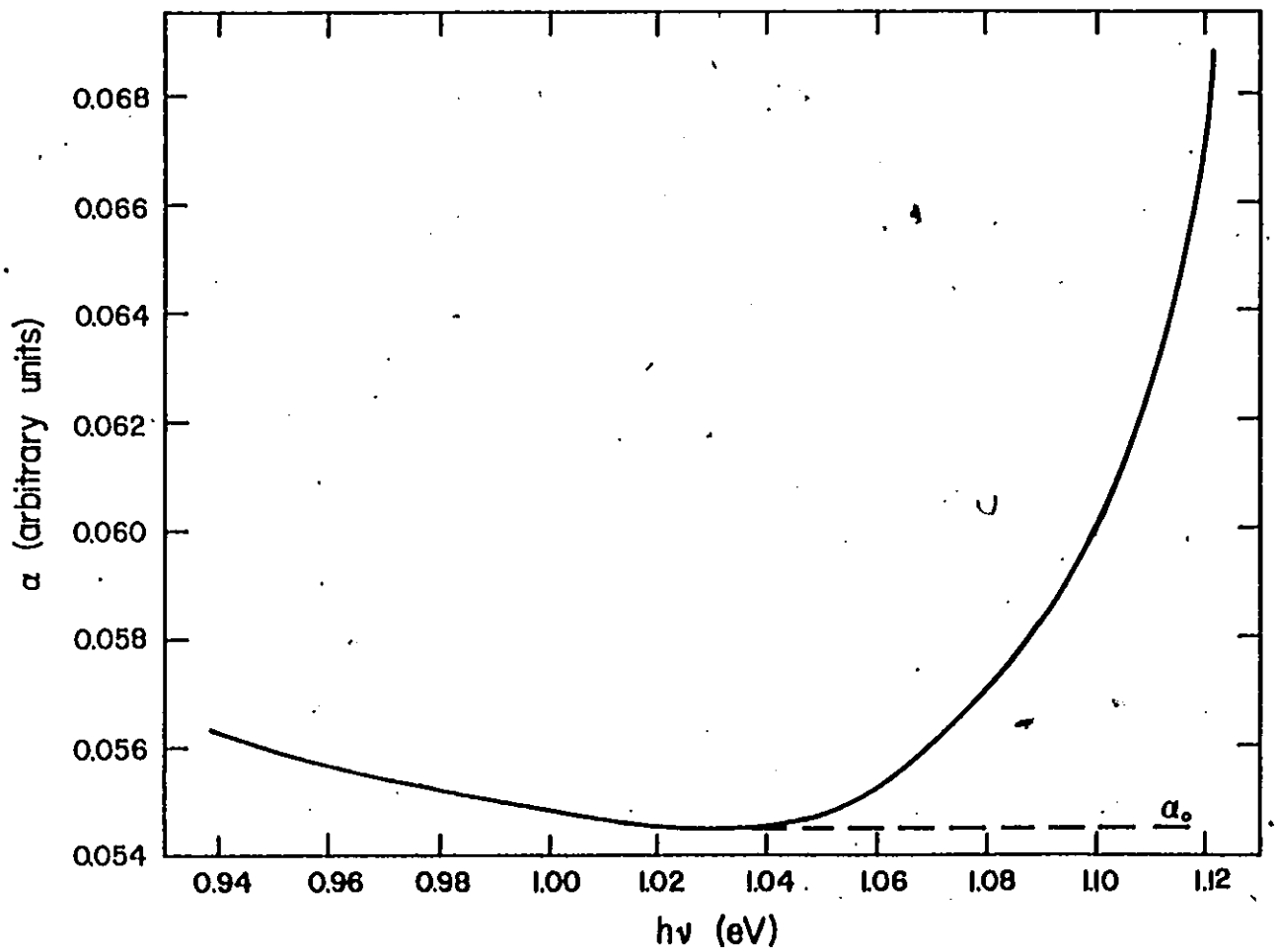

Figure 5.4(a) Absorption spectrum for $(Cu_{0.5}Ag_{0.5})GaTe_2$(500010). Although scattering effects are evident, a straight line extrapolation of the background absorption, α_o, was used to determine values of α.

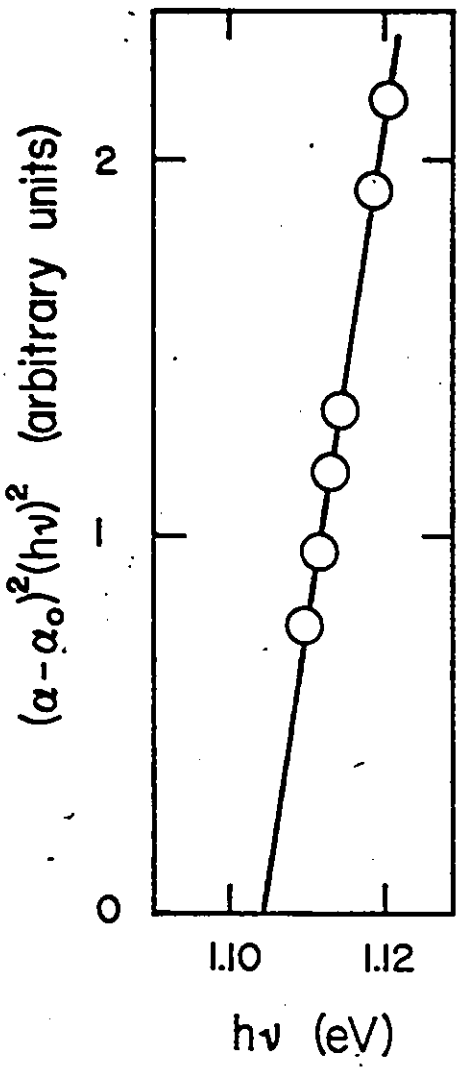

Figure 5.4(b) The straight-line variation of $(\alpha - \alpha_o)^2(h\nu)^2$ versus $h\nu$ for $(Cu_{0.5}Ag_{0.5})GaTe_2$.

as hν decreases. This type of variation, as discussed in section 3.2, takes the form $\alpha = \alpha_o(h\nu)^{-m}$. However, close to the band edge this effect is small compared with the other background effects. Thus, in the calculation of α, a straight line extrapolation of the background absorption, α_o, was again subtracted from the measured value of $\frac{1}{d}\ell n(\frac{I_0}{I_T})$.

Figures 5.3(b) and 5.4(b) show the corresponding variation of $(\alpha - \alpha_o)^2(h\nu)^2$ versus hν for the 750010 and 500010 compositions respectively. Since the resulting curves are straight, the value of n appearing in equation (3.5) was appropriately chosen as $n = \frac{1}{2}$. This confirms that the transitions involved are direct.

Owing to the difficulties discussed above in determining energy gaps, the only faces of the composition range having complete data are the copper face (data obtained by K. Yoodee) and the indium face. Energy gap values were determined for several of the interior compositions with nearly complete data being obtained for the x = 0.25 and z = 0.75 planes. These, as well as the copper and indium faces, are the only planes which will be discussed in detail. Energy gap values for the compositions concerned with here, as well as all other determined values (corresponding to random compositions), are listed in Table 5.1.

Curves of the energy gap, E_g, versus composition for the copper and indium faces are shown in figures 5.5 and 5.6 respectively. As in the case of the lattice parameter variations discussed in section 4.1, parabolic curves were obtained and fitted to an equation of the form

$$E_g = A + Bu + Cv + Du^2 + Ev^2 + Fuv + Gu^2v + Huv^2 + Iu^2v^2 \text{ eV.} \qquad (5.1)$$

The coefficients, number of points, and the standard deviation σ, obtained in the least squares fit (see appendix) to equation (5.1) are summarized in Table 5.2. Since the standard deviation is small, differences between the experimental points and the corresponding value on the fitted curves may be attributed to scatter and not to some form of systematic variation.

The coefficients listed in Table 5.2 were used to calculate contours of constant energy gap. These are shown for the copper and indium faces in figures 5.7 and 5.8 respectively. Contours for the copper face are similar to those determined by Chapman et al (79C1, 79C2) for $(Cu_{1-x}Ag_x)In(Se_{1-z}S_z)_2$ alloys. The contours for the indium face are more unusual in that a minimum in energy gap occurs near the composition for which $x = 0.275$ and $z = 0.55$.

Curves of the energy gap, E_g, variation with composition for the $x = 0.25$ and $z = 0.75$ interior planes are shown in figures 5.9 and 5.10 respectively. For these planes an insufficient number of accurate points could be obtained to carry out the analysis used for the copper and indium faces, i.e. fitting to equation (5.1). Instead, for the $z = 0.75$ plane, each set of data in figure 5.10 was least squares fitted (Appendix) to a parabolic equation of the form

$$E_g = A + Bu + Cu^2 \qquad (5.2)$$

The coefficients determined in this manner are listed in Table 5.3 and the curves are drawn in figure 5.10. For the $x = 0.25$ section, only the data corresponding to the constant parameter $y = 0.75$ and $y = 1.0$ could

Sample	E_g (eV)	Method	Sample	E_g (eV)	Method	Sample	E_g (eV)	Method
000000	1.52	P	001025	0.854	A	501000	1.032	A
000025	1.42	P	001050	0.845	A	501025	0.898	A
000050	1.33	P	001075	0.875	A	501050	0.845	A
000075	1.30	P	001010	0.94	P	501075	0.859	A
	1.251	A		0.928	A	501010	0.916	A
000010	1.39	P	250075	1.201	A	750075	1.239	A
002500	1.37	P	250010	1.18	P	750010	1.15	P
002525	1.26	P	252525	1.262	A		1.102	A
002550	1.18	P	252575	1.111	A	752575	1.124	A
002575	1.20	P	255075	1.053	A	752510	1.00	P
	1.139	A	255010	1.12	P	755050	1.070	A
005000	1.21	P		1.042	A	755075	1.038	A
	1.239	A	257525	0.989	A	755010	1.10	P
005025	1.09	P	257550	0.944	A	757575	0.965	A
	1.088	A	257575	0.960	A	751025	0.912	A
005050	1.06	P	257510	1.00	P	751050	0.893	A
	1.044	A	251000	0.966	A	751075	0.872	A
0Q5075	1.08	P	251025	0.859	A	751010	0.93	P
	1.057	A	251050	0.81	P	100000	1.78	P
007500	1.06	P	251075	0.870	A	100010	1.16	P
	1.106	A	251010	0.927	A		1.092	A
007525	0.96	P	500075	1.199	A	102510	1.13	P
	0.977	A	500010	1.21	P	105075	1.079	A
007550	0.96	P		1.102	A	107575	0.998	A
	0.926	A	502510	1.09	P	101000	1.11	P
007575	0.97	P	505075	1.010	A	101025	1.04	P
	0.973	A	505010	1.09	P	101050	0.933	A
001000	0.94	P		1.065	A	101010	0.91	P
	0.954	A	507575	0.938	A		0.938	A

Table 5.1 All energy gap results, E_g, for the alloy system under present investigation. 'P' denotes photoacoustic and 'A' denotes absorption.

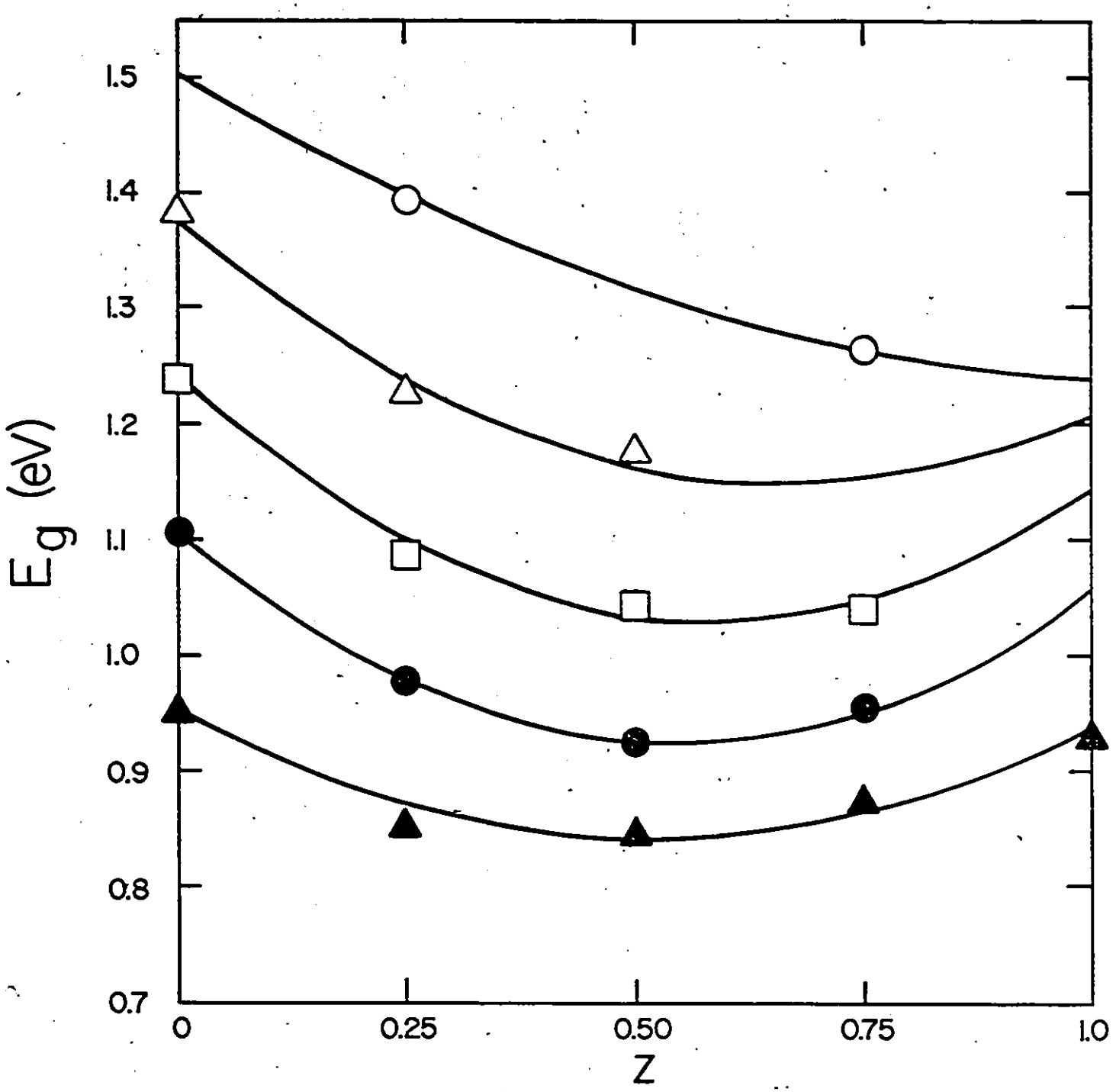

Figure 5.5 Variation of energy gap, E_g for the Cu face, as a function of z at various constant values of y. Experimental data was fitted to a nine-term power series equation.
y = 0 ○ , y = 0.25 △ , y = 0.50 □ , y = 0.75 ● , y = 1.0 ▲

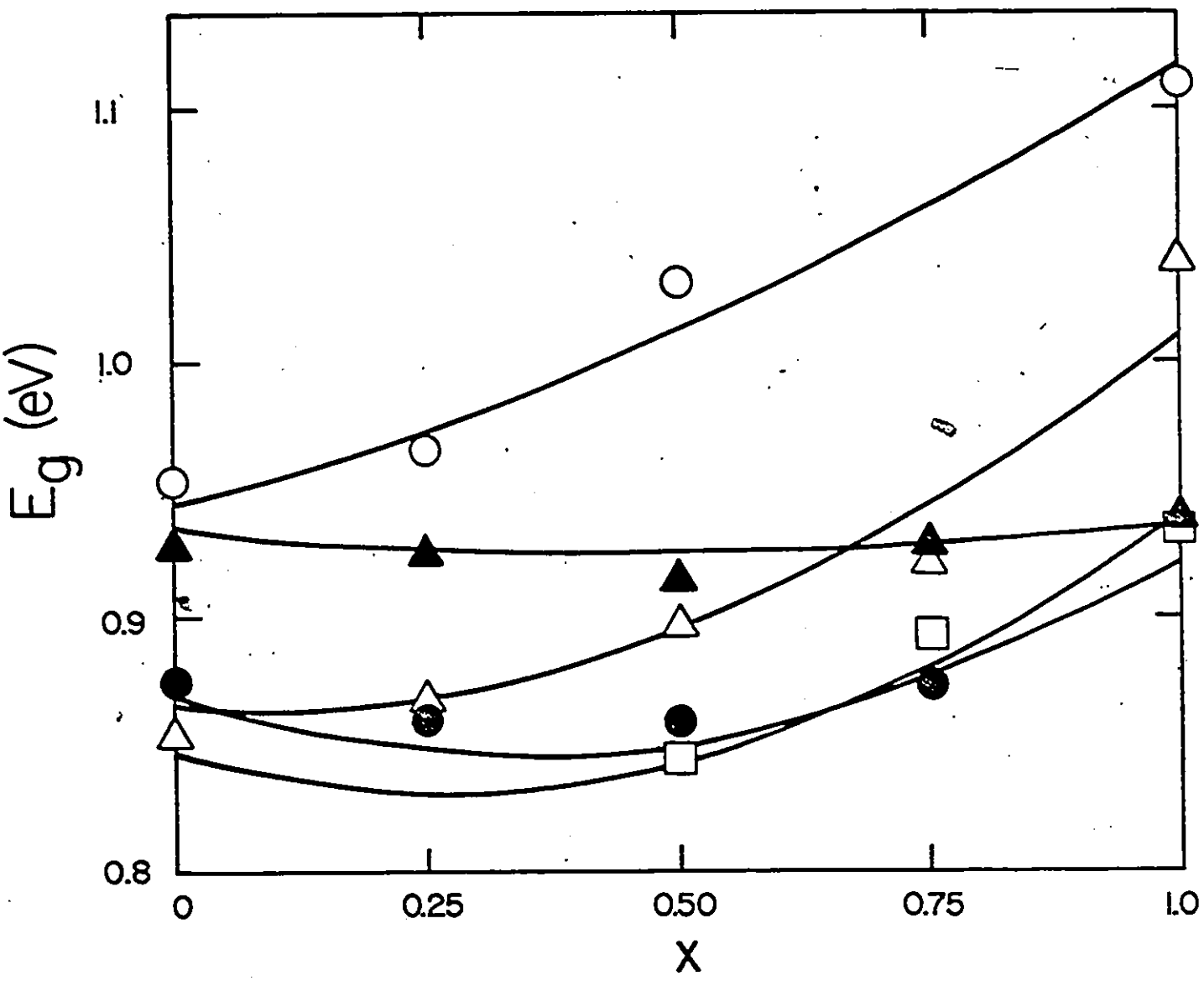

Figure 5.6 Variation of energy gap, E_g, for the In face as a function of x at various constant values of z. Experimental data was fitted to a nine term power series equation.
z = 0 ○ , z = 0.25 △ , z = 0.50 □ , z = 0.75 ● , z = 1.0 ▲

Face		Cu	In
Number of points		18	22
Variable compositions parameters (u,v)		(y,z)	(x,z)
Energy Gap, E_g (eV)	A	1.503	0.943
	B	-0.488	0.104
	C	-0.483	-0.386
	D	-0.067	0.071
	E	0.220	0.379
	F	-1.073	-0.709
	G	1.145	0.594
	H	1.476	0.569
	I	-1.299	-0.629
	σ	0.008	0.013

Table 5.2 Power series fitting coefficients to an equation $E_g = A + Bu + Cv + Du^2 + Ev^2 + Fuv + Gu^2v + Huv^2 + Iu^2v^2$ eV for the Cu and In faces. Also listed are the number of data points used in the analysis, the variable composition parameters, and the standard deviation σ.

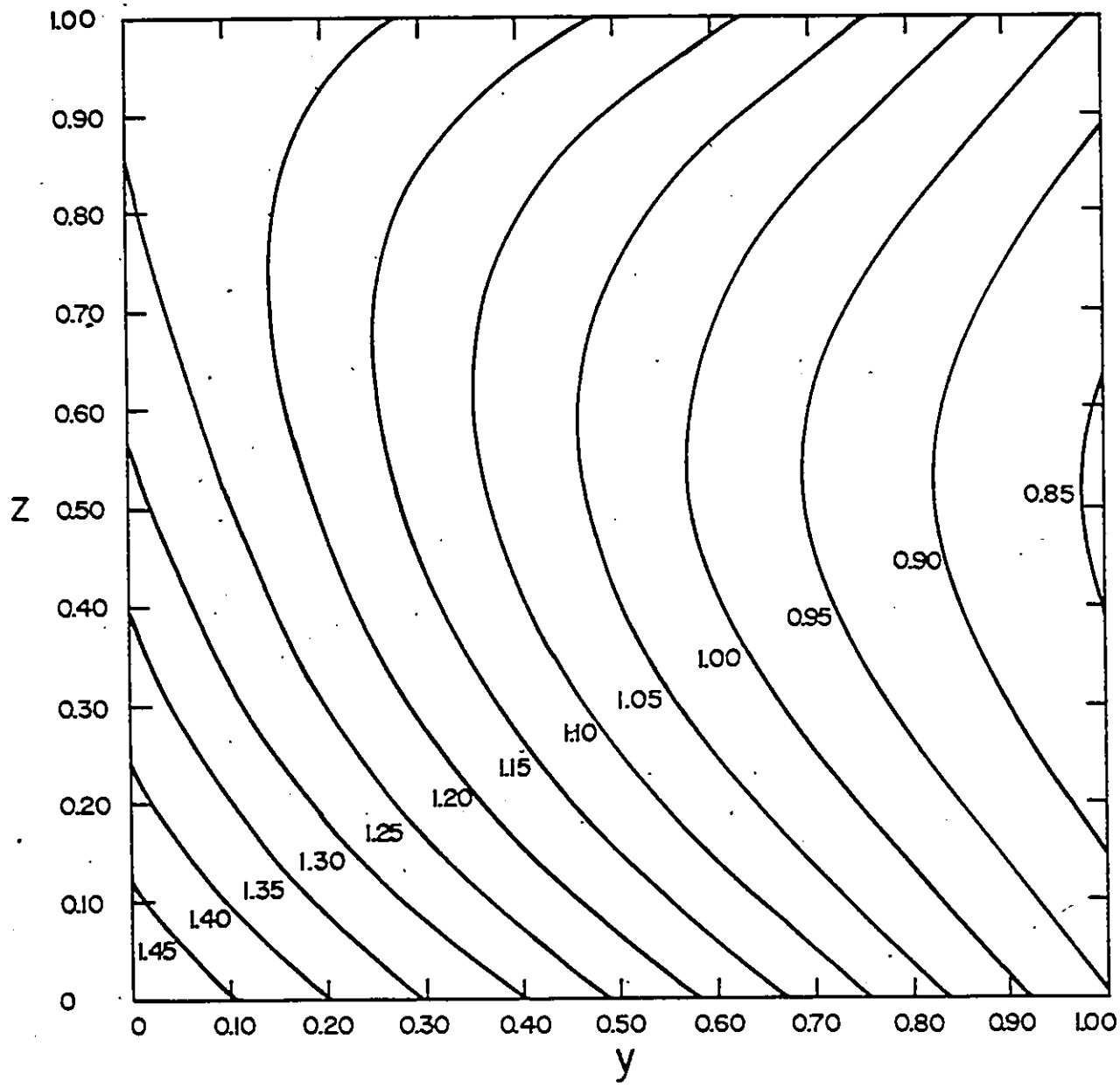

Figure 5.7 Contours of constant E_g(eV) for the Cu face.

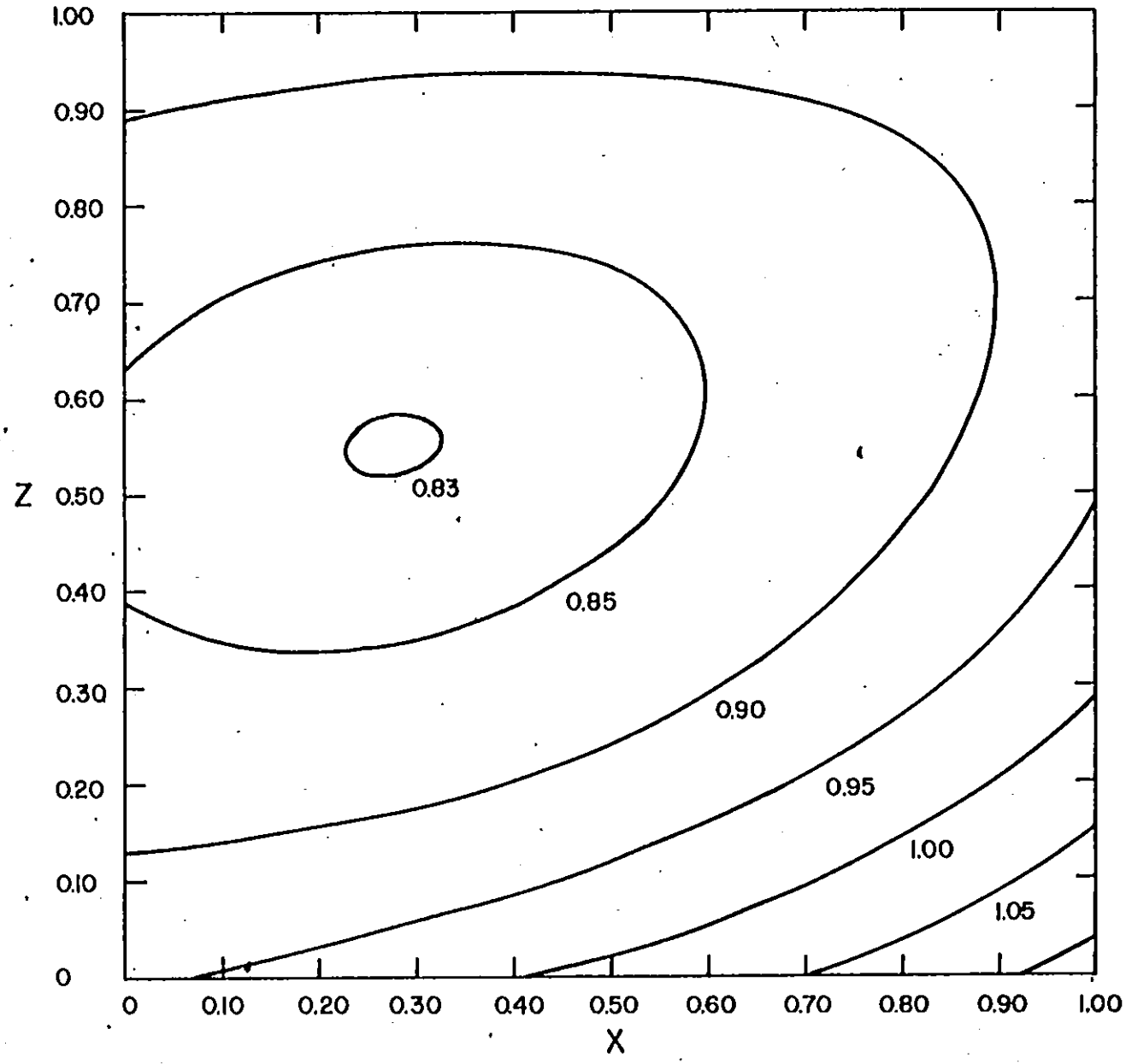

Figure 5.8 Contours of constant E_g (eV) for the In face. A minimum in E_g occurs near the composition for which x = 0.275 and z = 0.55.

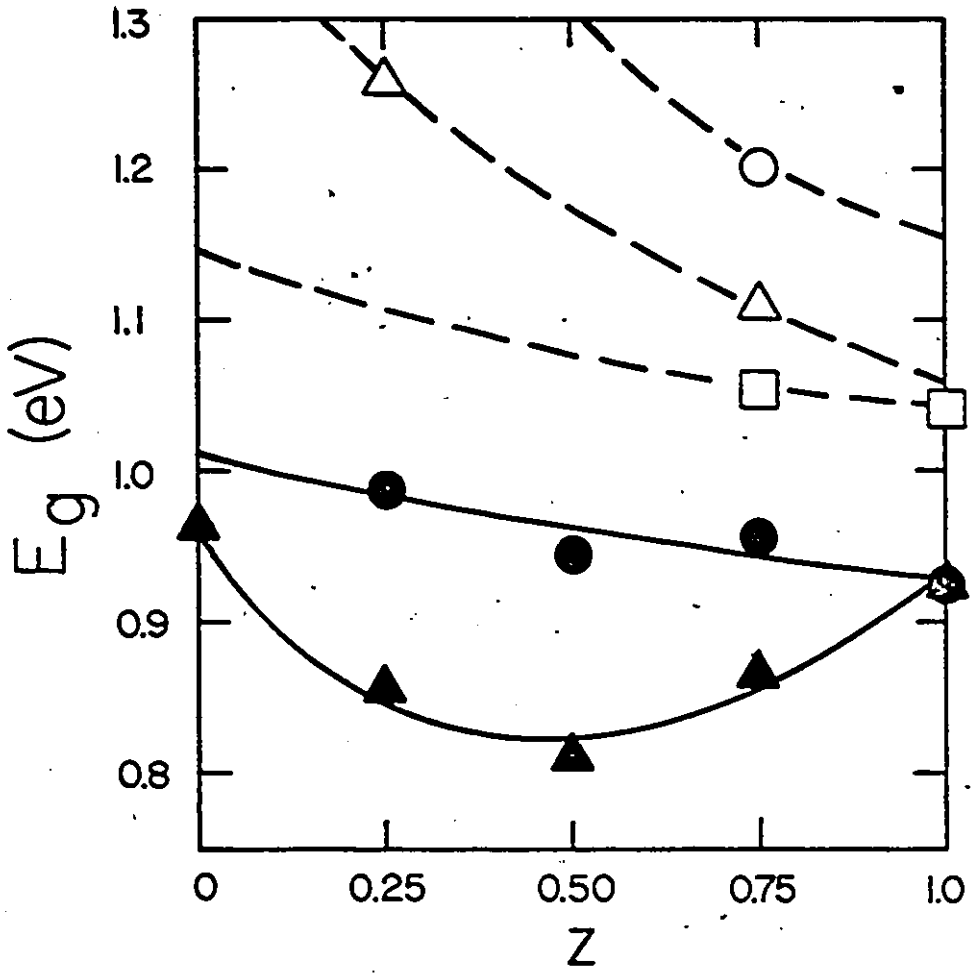

Figure 5.9 Variation of energy gap, E_g, for the x = 0.25 plane as a function of z at various constant values of y. The experimental data for the y = 0.75 and y = 1.0 curves were fitted to parabolic form (solid lines). Estimated curves were drawn for the y = 0, y = 0.25, and y = 0.50 (dashed lines).

y = 0 ○ , y = 0.25 △ , y = 0.50 □ , y = 0.75 ● , y = 1.0 ▲

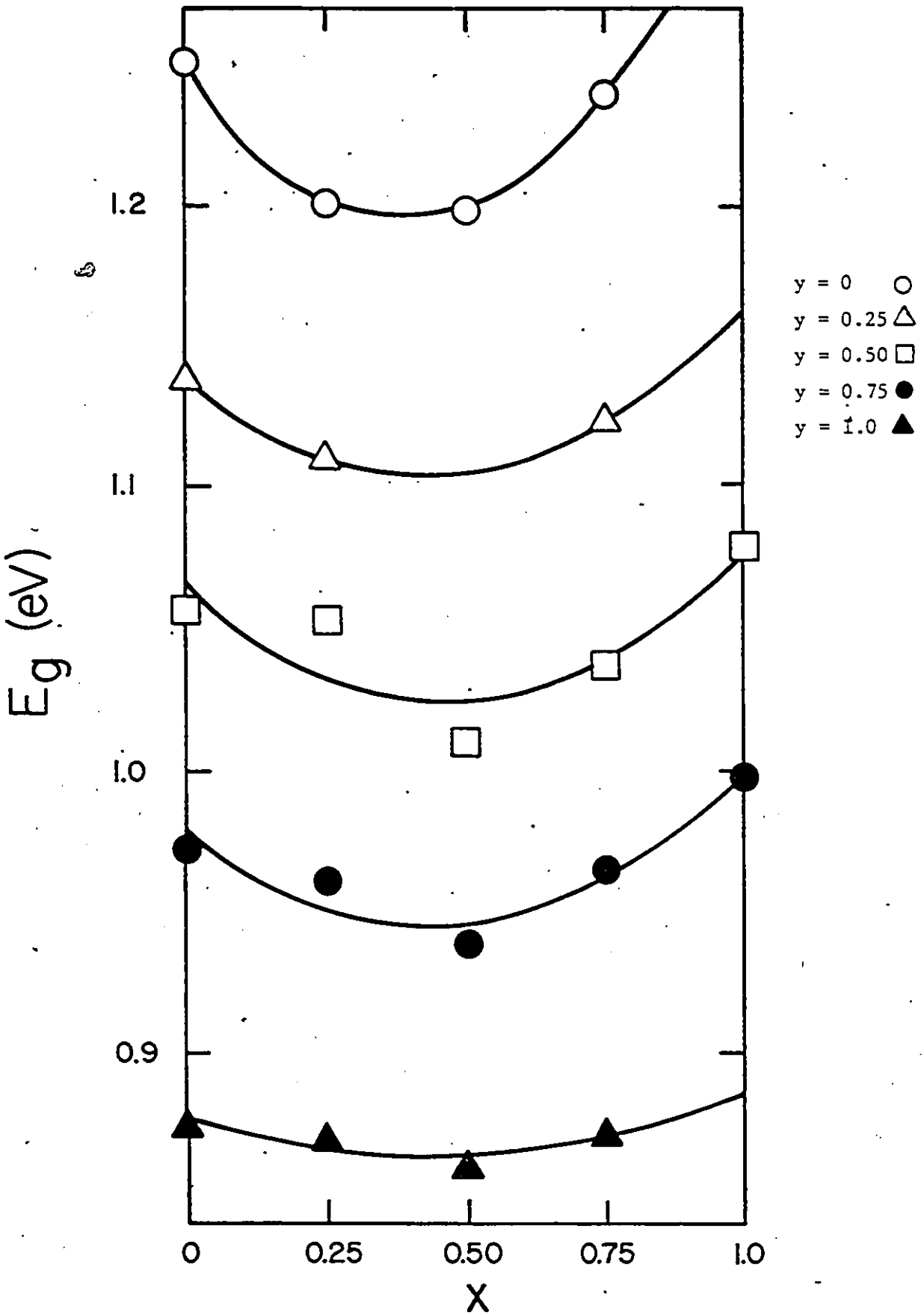

Figure 5.10 Variations of energy gap E_g for the [illegible] 0.75 plane as a function of x at various constant values of y. Experimental data corresponding to each value of y was fitted to parabolic form.

be fitted to equation (5.2), the equations determined in this way being

$$E_g = 0.962 - 0.526z + 0.499z^2 \text{ eV}$$

for y = 0.75, and

$$E_g = 1.011 - 0.120z + 0.040z^2 \text{ eV}$$

coefficient \ y	0	0.25	0.50	0.75	1.0
A	1.251	1.139	1.065	0.976	0.877
B	-0.285	-0.158	-0.172	-0.139	-0.062
C	0.360	0.184	0.184	0.161	0.072

Table 5.3 Parabolic fitting coefficients to an equation $E_g = A + Bu + Cu^2$ eV for the z = 0.75 interior plane. The variable parameter, u, is x in this case for constant y values.

for y = 1.0. For the y = 0, 0.25, and 0.5 variations (x = 0.25 plane) only one or two experimental points were determined for each curve and thus no fitting could be done. However, guided by the energy gap values for the compounds, dashed curves have been drawn estimating the type of variation that can be expected in these cases. As seen in figure 5.9 the resulting curve for the y = 1.0 variation shows a minimum.

This is expected since these values are common with the indium face. However, as progression is made toward the y = 0 curve, the minimum vanishes and the curves become progressively steeper.

5.2 Summary

Energy gap values were investigated for most of the $(Cu_{1-x}Ag_x)(Ga_{1-y}In_y)(Se_{1-z}Te_z)_2$ alloys excluding those previously found be be two phase or multiphase. This was done using either of the absorption or photoacoustic techniques outlined in Chapter III. The absorption method was used whenever possible. However, owing to either strong absorption by free carriers or impurities, or the condition of the material being poor, absorption methods were not always successful. In such cases attemps were made to determine the energy gap photoacoustically. This latter method, as well, was not always successful since, for several alloys, the resulting PA spectra were relatively flat.

As a result of the above difficulties the only faces having complete energy gap data are the copper face (determined by K. Yoodee) and the indium face. Energy gap values were determined for several of the interior compositions with nearly complete data being obtained for the x = 0.25 and z = 0.75 planes. Curves of the energy gap versus composition were plotted for the copper and indium faces and the x = 0.25 and z = 0.75 planes. Experimental data for the Cu and In faces were least squares fitted to a nine term power series equation (equation (5.1)). The standard deviation from the fitted curves was small suggesting any differences between the experimental points and the curves is due to scatter. Experimental data for curves of constant y were fitted to parabolic form (equation (5.2)) for the

z = 0.75 plane and part of the x = 0.25 plane (y = 0.75 and y = 1.0). For the remainder of the x = 0.25 plane insufficient data was available to do any fitting, thus only estimated curves could be drawn.

Contours of constant a and c were plotted for both the copper and indium faces, with a minimum in the indium face occurring near the x = 0.275, z = 0.55 composition.

CHAPTER VI - TEST OF INTERPOLATION EQUATIONS

6.1 Introduction

There has been considerable interest in quaternary semiconductor materials for various technical applications. Regardless of this, however, very little information is available on these materials with no detailed studies having been performed. As a result, various attempts have been made to suggest interpolation methods to estimate quaternary parameters from binary and/or ternary alloy values. The basic interpolation approach is to assume a linear interpolation and superimpose on this some type of bowing. Two examples of such an analysis, applicable to the present work, have been carried out by Glisson et al (78Gl) and Moon et al (74Ml). These interpolation techniques are presented in section 6.2.

6.2 Moon et al and Glisson et al Interpolation Formulae

In order to estimate the band gap and lattice constant values for quaternary alloy systems of the general form $A_{1-x}B_xC_{1-y}D_y$, Moon et al (74Ml) and Glisson et al (78Gl) have developed separate formulae interpolating these values from ternary and binary data. The formulae proposed by the two groups differ to some extent (see below), both dealing with a two-parameter (x and y), or two dimensional, representation of the alloy composition. Thus, in both cases, the compositions were graphically represented by means of a square in the x-y plane with a binary compound at each of the corners. Further, the quaternary alloy parameter under investigation (e.g. band gap or lattice constant) was described by a parameter Q(x,y) over the x, y

composition plane. At the corners (x and y equal to zero and/or one) the parameter, Q(x, y), for the four binary compounds can be defined as $Q(0, 0) = B_1$, $Q(1, 0) = B_2$, $Q(1, 1) = B_3$, and $Q(0, 1) = B_4$ (see figure 6.1). Along the boundaries of the plane, the parameter for the four ternary alloys can be defined as $Q(x, 0) = T_{12}(x)$, $Q(1, y) = T_{23}(y)$, $Q(x, 1) = T_{43}(x)$, and $Q(0, y) = T_{14}(y)$. Using the above notation, a linear interpolation of ternary alloy parameters obtained from constituent binary compounds may be expressed as

$$T_{0ij}(x) = (1 - x)B_i + xB_j. \tag{6.1}$$

Although many ternary alloy parameters may be defined using equation (6.1), others may show a nonlinear variation with composition. Thompson and Woolley (67T1) have shown that for the direct band gap, equation (6.1) takes the form

$$T_{ij}(x) = T_{0ij} - \delta T_{ij}, \tag{6.2}$$

where $\delta T_{ij} = C_{ij}x(1 - x)$ and C_{ij} is the bowing parameter for the ternary alloy band gap T_{ij}. The interpolation scheme proposed by Moon et al (74M1) continues by assuming that in a two-dimensional model, the quaternary bowing δQ, is composed of the sum of the bowing contributed by each of the x and y sublattices, i.e. $\delta Q = \delta Q_x + \delta Q_y$. In addition, values of δQ_y at any constant x and δQ_x at any constant y were assumed to be given by linear interpolation between the end values. Referring to figure 6.1, if the value of the bowing parameter at points P_1, P_2, P_3, and P_4 is given by $C_{14}y(1 - y)$, $C_{23}y(1 - y)$, $C_{12}x(1 - x)$, and $C_{34}x(1 - x)$ respectively then

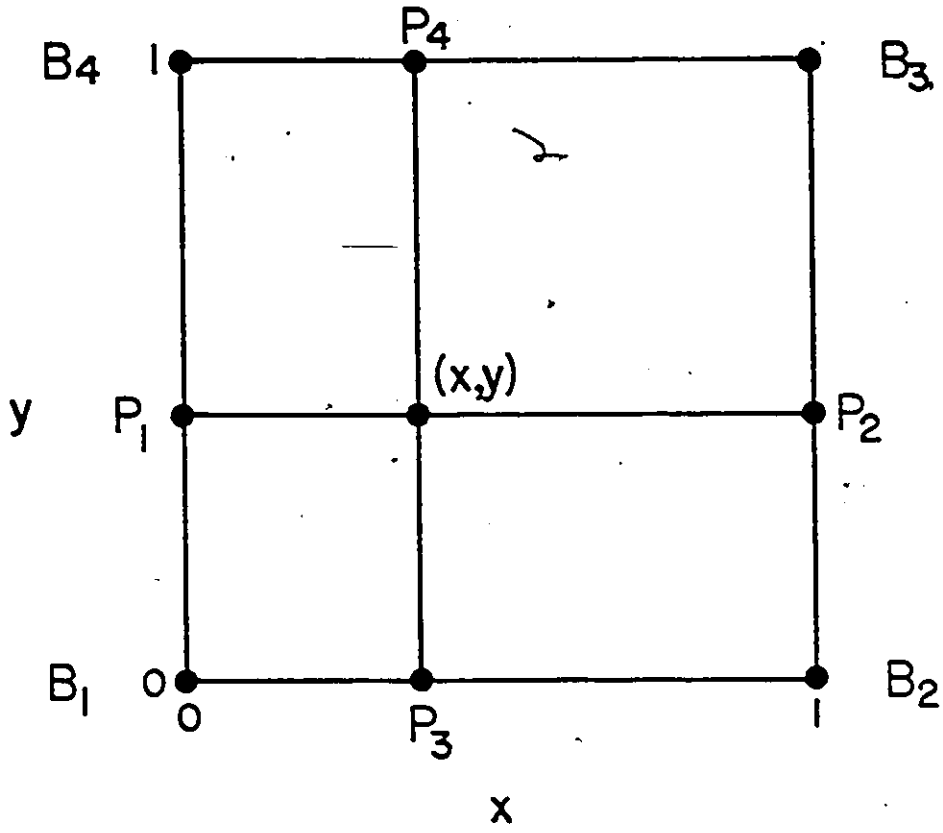

Figure 6.1 . Two dimensional representation of the alloy composition range. The parameter Q for the four binary compounds are given by B_1, B_2, B_3, and B_4 as shown. P_1, P_2, P_3, and P_4 are compositions along the edges of the composition range.

$$\delta Q_y = (1 - x)C_{14}y(1 - y) + xC_{23}y(1 - y) \qquad (6.3)$$

and

$$\delta Q_x = (1 - y)C_{12}x(1 - x) + yC_{34}x(1 - x). \qquad (6.4)$$

Equations (6.3) and (6.4) may be rewritten as

$$\delta Q_y = y(1 - y)[(1 - x)C_{14} + C_{23}] \qquad (6.5)$$

and

$$\delta Q_x = x(1 - x)[(1 - y)C_{12} + yC_{34}], \qquad (6.6)$$

Thus

$$\delta Q = y(1 - y)[(1 - x)C_{14} + xC_{23}] + x(1 - x)[(1 - y)C_{12} + yC_{34}] \qquad (6.7)$$

In the same way as the nonlinear variation (6.2) was written for ternary alloy parameters; Q(x, y), the quaternary alloy parameter, may be expressed as

$$Q(x, y) = Q_o - \delta Q \qquad (6.8)$$

where $Q_o = (1 - x)T_{014}(y) + xT_{023}(y)$. Note that Q_o may equally be expressed as $Q_o = (1 - y)T_{012}(x) + yT_{043}(x)$ and in terms of the corner compounds, both forms lead to the expression

$$Q_o = (1 - x)(1 - y)B_1 + x(1 - y)B_2 + xyB_3 + y(1 - x)B_4. \qquad (6.9)$$

Substituting (6.7) and (6.9) into (6.7) gives the complete expression for Q(x, y) as proposed by Moon et al, i.e.

$$\begin{aligned} Q(x, y) &= (1 - x)(1 - y)B_1 + x(1 - y)B_2 + xyB_3 + y(1 - x)B_4 \\ &= y(1 - y)[(1 - x)C_{14} + xC_{23}] - x(1 - x)[(1 - y)C_{12} + yC_{34}]. \end{aligned} \qquad (6.10)$$

Glisson et al (78Gl) propose that the values of Q(x, y) inside the square are given by

$$Q(x, y) = \frac{x(1-x)[(1-y)T_{12}(x) + yT_{43}(x)] + y(1-y)[(1-x)T_{14}(y) + xT_{23}(y)]}{x(1-x) + y(1-y)} \quad (6.11)$$

This is essentially an ad hoc expression, and, as will be shown in section 6.4, does not give as good a fit as equation (6.10) in the case of the band gap. In the case of the lattice constant, also to be shown later, the two methods give essentially the same result.

An important difference between the two interpolation methods was interpreted by Glisson et al to be associated with the manner in which the bowing parameter, δQ, enters each formulation. In equation (6.11) Glisson states that the ternary bowing effects are included in the T_{ij}'s, whereas with the Moon method, the bowing enters as a separate quaternary bowing parameter term given by equation (6.7). At the centre of the composition square, equation (6.11) gives $\frac{1}{16}(C_{12} + C_{43} + C_{14} + C_{23})$ as the bowing parameter whereas using the Moon method $\frac{1}{8}(C_{12} + C_{43} + C_{14} + C_{23})$ is obtained. Thus at the centre of the composition range, the Moon bowing parameter is twice as large as the Glisson parameter.

The present experimental values can be used to test these interpolation equations and to compare their validity. For the lattice parameter, values of B_i, B_j, and C_{ij} were determined from the experimental values along the edges of the cubic composition range. These were then used to predict values in the interior of the faces and interior of

the cube. The resulting predicted lattice parameter values were compared to the experimental data and the validity of the interpolation equations was assessed.

For the energy gap analysis, data along the edges of the faces was incomplete so that the parameter values along the edges, T_{ij}, could not be determined. Thus, rather than use equations (6.10) and (6.11) for interpolation, they were used instead to fit all the experimental data on the faces. The fitting can be done in two ways for each equation. Either the B values can be assumed known from the compounds and a fit made to the four C parameters, or alternatively both the four B and four C parameters can be determined by fitting. However, because the number of points on the copper face was limited, the former method was used since this involves a fit to only four parameters. An estimate of the validity of the interpolation equations was given by the standard deviation of the fitted points for both the energy gap and lattice parameter analyses.

6.3 Extension of the Moon et al Interpolation Method to Three Dimensions

In the previous section interpolation equations obtained by Moon et al and Glisson et al to determine quaternary alloy band gaps and lattice constants from ternary and binary data were presented. The quaternary alloys in that work were of the general form $A_{1-x}B_xC_{1-y}D_y$ and were thus uniquely represented by the parameters x and y.

The present research programme is the investigation of chalcopyrite alloys of the general form $A_{1-x}B_xC_{1-y}D_y(E_{1-z}F_z)_2$. In the first part of the work, sections with x, y, or z equal to 0 or 1 are

considered, giving a two variable problem to which the Moon et al equations can be applied. However, a further part of the research programme involves alloys in which all three composition parameters are varied. Thus, in order to fit the values of lattice parameter and energy gap obtained in those alloys, a three dimensional interpolation model must be developed.

As will be discussed in detail in section 6.4, results indicate that as far as fitting to the experimental data is concerned, the equations of Moon et al are preferable to those of Glisson et al. Thus, the analysis of the three dimensional case developed here begins from the Moon formulation.

In the three dimensional model, for the general system of the type considered in the present investigation, the square x-y composition range is replaced by a cube having a ternary compound at each of its corners (see figure 6.2). The parameter under study is now described by a parameter P(x, y, z). Along the edges of the cube, as with the sides of the square composition range, P(x, y, z) is assumed to vary parabolically. Referring to figure 6.2, at the corners of the cube the elements $P(0, 0, 0) = B_1$, $P(1, 0, 0) = B_2$, $P(1, 1, 0) = B_3$, etc. are defined.

By analogy with equations (6.2) and (6.8), the alloy parameter at any point (x, y, z) in the middle of the cube may be expressed in terms of P_o, a linear interpolation of the corresponding values of the parameter Q_o obtained on any two opposite faces (points A and D for example on figure 6.2); and, δP, a term accounting for bowing effects. Thus

$$P(x, y, z) = P_o - \delta P \qquad (6.12)$$

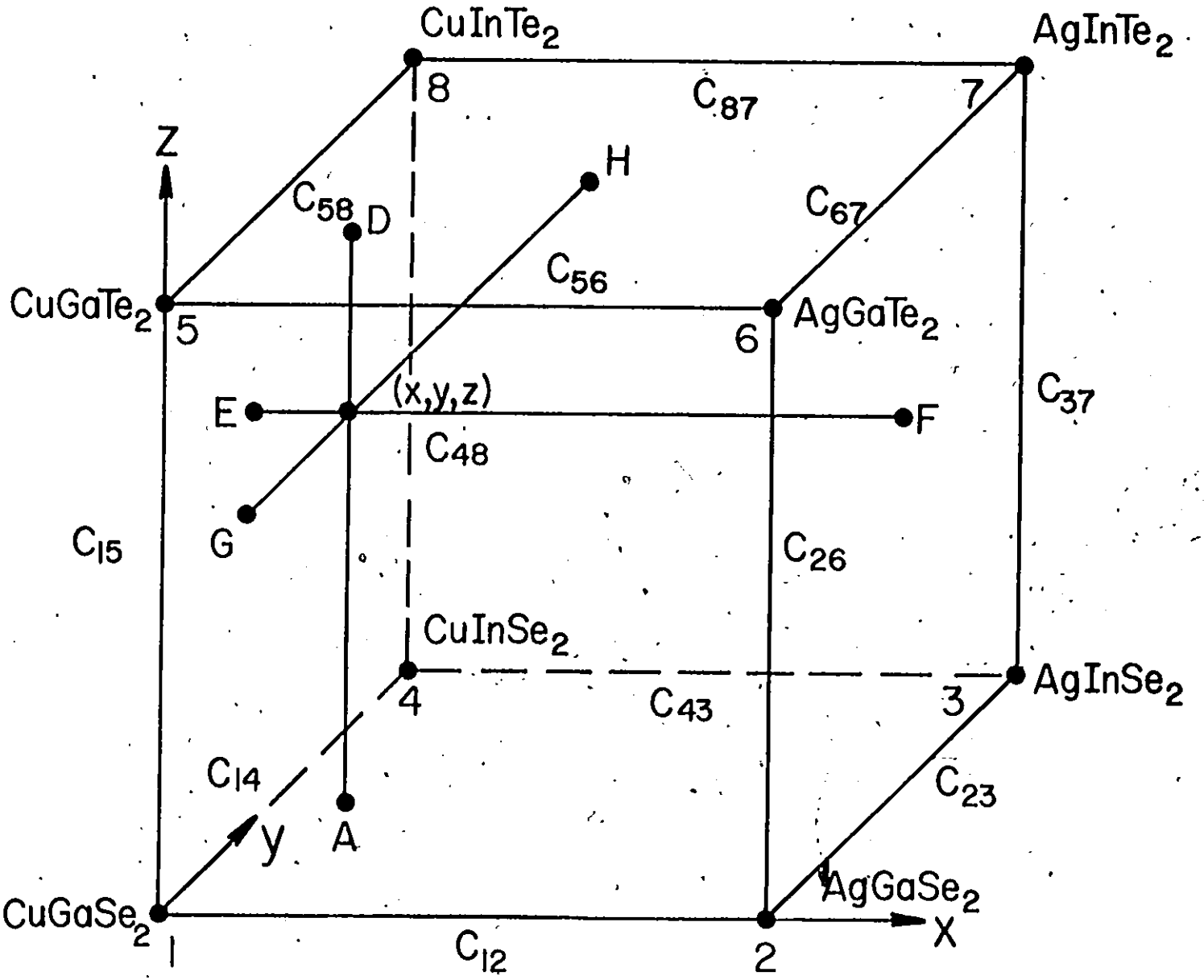

Figure 6.2 The cubic composition range for the three dimensional model. Points A through G are located on the faces of the cube. The bowing parameters C_{ij} are shown along the appropriate cube edge.

and

$$P_o = (1 - z)Q_{oA}(x, y) + z\,Q_{oD}(x, y) \qquad (6.13)$$

Equation (6.13) may equally have been expressed as

$$P_o = (1 - x)Q_{oE}(y, z) + Q_{oF}(y, z) \qquad (6.14)$$

or

$$P_o = (1 - y)Q_{oG}(x, z) + y\,Q_{oH}(x, z) \qquad (6.15)$$

The results obtained by Moon et al given by equation (6.9) may be used to rewrite equation (6.13) as

$$P_o = (1 - z)[(1 - x)(1 - y)B_1 + x(1 - y)B_2 + xyB_3 + y(1 - x)\,B_4]$$

$$+ z[(1 - x)(1 - y)B_5 + x(1 - y)B_6 + xyB_7 + y(1 - x)B_8] \qquad (6.16)$$

Expanding this gives

$$P_o = (1 - x)(1 - y)(1 - z)B_1 + x(1 - y)(1 - z)B_2 + xy(1 - z)B_3$$

$$+ (1 - x)y(1 - z)B_4 + (1 - x)(1 - y)zB_5 + x(1 - y)zB_6$$

$$+ xyzB_7 + (1 - x)yzB_8 \qquad (6.17)$$

Again, by analogy with the two dimensional case, the bowing, δP, is assumed to be given by the sum of the bowing contributions from each of the three sublattices, i.e.

$$\delta P = \delta P_x + \delta P_y + \delta P_z. \qquad (6.18)$$

In addition, δP_x for constant y and z is assumed to vary linearly with x. Similar linear variations are also assumed for δP_y and δP_z. Thus,

$$2\delta P = (1 - x)\delta Q_E(y, z) + x\delta Q_F(y, z) + (1 - y)\delta Q_G(x, z) + y\delta Q_H(x, z)$$

$$+ (1 - z)\delta Q_A(x, y) + z\delta Q_D(x, y) \qquad (6.19)$$

The left hand side of equation (6.19) is $2\delta P$, since in the summation, the effects of each sublattice have been counted twice. Substituting values of δQ as given by equation (6.7) into (6.19) gives

$$\delta P = x(1 - x)(1 - y)(1 - z)C_{12} + xy(1 - y)(1 - z)C_{23} + x(1 - x)y(1 - z)C_{34}$$

$$+ (1 - x)y(1 - y)(1 - z)C_{14} + (1 - x)(1 - y)z(1 - z)C_{15}$$

$$+ (1 - x)y(1 - y)zC_{58} + (1 - x)yz(1 - z)C_{48} + x(1 - y)z(1 - z)C_{26}$$

$$+ xy(1 - y)zC_{67} + xyz(1 - z)C_{37} + x(1 - x)(1 - y)zC_{56}$$

$$+ x(1 - x)yzC_{87} \qquad (6.20)$$

Hence from equations (6.18) and (6.20)

$$P = (1 - x)(1 - y)(1 - z)B_1 + x(1 - y)(1 - z)B_2 + xy(1 - z)B_3$$

$$+ (1 - x)y(1 - z)B_4 + (1 - x)(1 - y)zB_5 + x(1 - y)zB_6$$

$$+ xyzB_7 + (1 - x)yzB_8 - x(1 - x)(1 - y)(1 - z)C_{12}$$

$$+ xy(1 - y)(1 - z)C_{23} - x(1 - x)y(1 - z)C_{34} - (1 - x)y(1 - y)(1 - z)C_{14}$$

$$- (1 - x)(1 - y)z(1 - z)C_{15} - (1 - x)y(1 - y)zC_{58}$$

$$- (1 - x)yz(1 - z)C_{48} - x(1 - y)z(1 - z)C_{26} - xy(1 - y)zC_{67}$$

$$- xyz(1 - z)C_{37} - x(1 - x)(1 - y)zC_{56} - x(1 - x)yzC_{87}. \qquad (6.21)$$

6.4 Application of Glisson et al and Two-Dimensional Moon et al Interpolation Equations

In order to determine values of C_{ij}, B_i, and B_j in the Glisson et al and two-dimensional Moon et al analyses, the edges of the present cubic composition range were fitted to parabolic form, i.e.

$$a = \alpha + \beta u + \gamma u^2 \text{ nm} \qquad (6.22)$$

$$c = \alpha' + \beta' u + \gamma' u^2 \text{ nm} \qquad (6.23)$$

The coefficients α, β, γ, α', β', and γ' for each edge are listed in Table 6.1, with the corners of the cube labelled as shown in figure 6.2 and the appropriate variable indicated.

The parameters B_i and B_j are defined in section 6.2 and correspond to values of the lattice parameter a for u = 0 and u = 1 respectively. Similarly, B_i' and B_j' correspond to the lattice parameter c for u = 0 and u = 1 respectively. Thus B_i and B_j or B_i' and B_j' may be obtained from equations (6.22) and (6.23) using the appropriate coefficients listed in Table 6.1. The parameter C_{ij} is the bowing parameter for the ternary lattice parameter, T_{ij}, defined in equation (6.2). Thus C_{ij} is just the γ coefficient for the lattice parameter a and C_{ij}' is the γ' coefficient for the c lattice parameter.

The values of B_i, B_j, C_{ij}, B_i', B_j', and C_{ij}' for each edge of the cube are also listed in Table 6.1. Since each corner of the cube is common to three edges, the B and B' parameters for each i or j where i = j were determined by independently fitting to equation (6.22) or (6.23) three times. An average of the three values obtained for each B and B' parameter was used in the remaining analysis. The three values that were averaged, together with the mean value for each B_i (or B_j) are listed in Table 6.2. Table 6.3 shows similar data for the B' parameters.

With the values of the B and C parameters determined, equations (6.10) and (6.11), corresponding to the Moon and Glisson interpolation equations respectively, were used to predict lattice parameter values for compositions located inside each of the six faces of the cube. The experimental value, the Moon and Glisson predicted value, and the standard deviation in each case is listed in Tables 6.4 through 6.9 for both the a and c lattice parameters. The experimental points and the values predicted by the Moon and Glisson equations have been plotted for the tellurium face in figure 6.3(a) and 6.3(b) for the lattice parameters a and c respectively. As is

	edge i - j	1 - 2	4 - 3	5 - 6	8 - 7	1 - 4	2 - 3	5 - 8	6 - 7	1 - 5	4 - 8	2 - 6	3 - 7
	u	x	x	x	x	y	y	y	y	z	z	z	z
Lattice parameter a(nm)	α	0.5616	0.5794	0.6027	0.6200	0.5620	0.5974	0.6026	0.6324	0.5619	0.5795	0.5973	0.6104
	β	0.0336	0.0798	0.0167	0.0163	0.0128	0.0156	0.0118	0,0112	0.0073	0.0317	0.0294	0.0154
	γ	0.0019	0.0129	0.0129	0.0089	0.0044	-0.0029	0.0058	0.0016	0.0033	0:0093	0.0056	0.0196
	B_i	0.5616	0.5794	0.6027	0.6200	0.5620	0.5974	0.6025	0.6324	0.5619	0.5795	0.5973	0.6104
	B_j	0.5972	0.6103	0.6323	0.6452	0.5793	0.6101	0.6201	0.6452	0.6025	0.6204	0.6323	0.0645
	C_{ij}	0.0019	0.0129	0.0129	0.0089	0.0044	-0.0029	0.0058	0.0016	0.0033	0.0093	0.0056	0.0196
Lattice parameter c(nm)	α'	1.1031	1.1575	1.1937	1.2374	1.1020	1.0946	1.1934	1.1990	1.1021	1.1572	1.0936	1.1711
	β'	0.0026	0.0530	0.0181	0.0493	0.0747	0.0577	0.0511	0.0705	0.0892	0.0725	0.0606	0.0622
	γ'	-0.0113	-0.0395	-0.0130	-0.0226	-0.0193	0.0195	-0.0145	-0.0058	0.0024	0.0088	0.0465	0.0303
	B_i'	1.1031	1.1575	1.1937	1.2374	1.1020	1.0946	1.1934	1.1990	1.1021	1.1572	1.0936	1.1711
	B_j'	1.0945	1.1710	1.1988	1.2640	1.1575	1.1719	1.2380	1.2636	1.1937	1.2386	1.2077	1.2636
	C_{ij}'	-0.0113	-0.0395	-0.0130	-0.0226	-0.0193	0.0195	-0.0145	-0.0058	0.0024	0.0088	0.0465	0.0303

Table 6.1 The coefficients α, β, γ, α', β', and γ' determined by fitting the experimental points along each cube edge, i - j, to parabolic form. The corresponding values of lattice parameter for the compounds, B_i, B_j, B_i', and B_j' and the bowing parameters C_{ij} and C_{ij}' are also listed.

parameter / $B_{i=j}$	Averaged B_i's or B_j's for i = j (nm)			Mean (nm)
B_1	0.5620	0.5616	0.5619	0.5618
B_2	0.5972	0.5974	0.5973	0.5973
B_3	0.6103	0.6104	0.6101	0.6103
B_4	0.5793	0.5794	0.5795	0.5794
B_5	0.6027	0.6025	0.6025	0.6026
B_6	0.6323	0.6323	0.6324	0.6323
B_7	0.6454	0.6452	0.6452	0.6453
B_8	0.6200	0.6201	0.6204	0.6202

Table 6.2 Averaged values of B_i's or B_j's for each i = j corresponding to the lattice parameter, a.

parameter / $B_{i'=j}$	Averaged B_i''s or B_j''s for i = j (nm)			Mean (nm)
B_1'	1.1020	1.1031	1.1021	1.1024
B_2'	1.0945	1.0945	1.0936	1.0942
B_3'	1.1710	1.1711	1.1719	1.1713
B_4'	1.1575	1.1575	1.1574	1.1575
B_5'	1.1937	1.1937	1.1934	1.1936
B_6'	1.2007	1.1988	1.1990	1.1995
B_7'	1.2636	1.2640	1.2636	1.2637
B_8'	1.2374	1.2380	1.2386	1.2380

Table 6.3 Averaged values of B_i''s or B_j''s for each i = j , corresponding to the lattice parameter c.

Composition	Experimental Value		Moon et al Prediction		Glisson et al Prediction	
	a(nm)	c(nm)	a(nm)	c(nm)	a(nm)	c(nm)
002525	0.5759	1.1395	0.5746	1.1409	0.5755	1.1396
002550	0.5862	1.1626	0.5844	1.1626	0.5855	1.1612
002575	0.5957	1.1842	0.5949	1.1848	0.5958	1.1837
005025	0.5790	1.1595	0.5784	1.1549	0.5796	1.1535
005050	0.5900	1.1806	0.5882	1.1757	0.5896	1.1743
005075	0.6008	1.1984	0.5987	1.1972	0.5999	1.1961
007525	0.5841	1.1680	0.5829	1.1666	0.5840	1.1655
007550	0.5947	1.1893	0.5925	1.1867	0.5939	1.1856
007575	0.6052	1.2056	0.6031	1.2077	0.6044	1.2069
σ (nm)			0.0017	0.0026	0.0006	0.0034

Table 6.4 Experimental values and Moon et al and Glisson et al predicted values of the a and c lattice parameter for compositions in the interior of the copper face (x = 0). The standard deviation, σ, for the Moon and Glisson interpolation equations are also given.

Composition	Experimental Value		Moon et al Prediction		Glisson et al Prediction	
	a(nm)	c(nm)	a(nm)	c(nm)	a(nm)	c(nm)
102575	0.6241	1.1829	0.6250	1.1820	0.6259	1.1860
105050	0.6186	1.1734	1.6183	1.1709	0.6198	1.1765
105075	0.6255	1.1990	0.6276	1.1996	0.6290	1.2037
107550	0.6220	1.1974	0.6206	1.1900	0.6223	1.1944
107575	0.6288	1.2185	0.6302	1.2172	0.6317	1.2205
σ (nm)			0.0013	0.0036	0.0022	0.0033

Table 6.5 Experimental values and Moon et al and Glisson et al predicted values of the a and c lattice parameter for single phase compositions in the interior of the silver face (x = 1). The standard deviation, σ, for the Moon and Glisson interpolation equations are also given.

Composition	Experimental Value		Moon et al Prediction		Glisson et al Prediction	
	a(nm)	c(nm)	a(nm)	c(nm)	a(nm)	c(nm)
250075	0.5955	1.1705	0.5976	1.1712	0.5989	1.1713
500075	0.6028	1.1719	0.6046	1.1705	0.6062	1.1718
750050	0.6021	1.1470	0.6040	1.1405	0.6053	1.1430
750075	0.6127	1.1726	0.6129	1.1682	0.6143	1.1704
σ (nm)			0.0017	0.0040	0.0030	0.0023

Table 6.6 Experimental values and Moon et al and Glisson et al predicted values of the a and c lattice parameter for single phase compositions in the interior of the gallium face (y=0). The standard deviation, σ, for the Moon and Glisson interpolation equations are also given.

Composition	Experimental Value		Moon et al prediction		Glisson et al Prediction	
	a(nm)	c(nm)	a(nm)	c(nm)	a(nm)	c(nm)
251025	0.5918	1.1848	0.5925	1.1858	0.5947	1.1838
251050	0.6040	1.2082	0.6018	1.2050	0.6042	1.2032
251075	0.6145	1.2292	0.6126	1.2259	0.6146	1.2247
501025	0.6026	1.1935	0.5986	1.1912	0.6015	1.1895
501050	0.6087	1.2143	0.6075	1.2105	0.6106	1.2091
501075	0.6202	1.2402	0.6181	1.2323	0.6207	1.2315
751025	0.6101	1.1960	0.6063	1.1922	0.6090	1.1912
751050	0.6152	1.2124	0.6145	1.2122	0.6175	1.2116
751075	0.6259	1.2392	0.6249	1.2353	0.6274	1.2351
σ (nm)			0.0023	0.0039	0.0016	0.0048

Table 6.7 Experimental values and Moon et al and Glisson et al predicted values of the a and c lattice parameter for compositions in the interior of the indium face (y = 1.0). The standard deviation, σ, for the Moon and Glisson interpolation equations are also given.

Composition	Experimental Value		Moon et al Prediction		Glisson et al Prediction	
	a(nm)	c(nm)	a(nm)	c(nm)	a(nm)	c(nm)
252500	0.5719	1.1187	0.5734	1.1207	0.5741	1.1181
752500	0.5902	1.1143	0.5913	1.1158	0.5916	1.1150
755000	0.5935	1.1356	0.5944	1.1344	0.5951	1.1327
757500	0.5973	1.1545	0.5973	1.1542	0.5982	1.1521
σ (nm)			0.0014	0.0035	0.0021	0.0043

Table 6.8 Experimental values and Moon et al and Glisson et al predicted values of the a and c lattice parameter for compositions in the interior of the selenium face ($z = 0$). The standard deviation, σ, for the Moon and Glisson interpolation equations are also given.

Composition	Experimental Value		Moon et al Prediction		Glisson et al Prediction	
	a(nm)	c(nm)	a(nm)	c(nm)	a(nm)	c(nm)
252510	0.6119	1.2078	0.6110	1.2126	0.6126	1.2100
255010	0.6169	1.2252	0.6150	1.2262	0.6167	1.2229
257510	0.6196	1.2392	0.6196	1.2382	0.6210	1.2351
502510	0.6177	1.2129	0.6176	1.2159	0.6193	1.2131
505010	0.6223	1.2309	0.6214	1.2307	0.6233	1.2272
507510	0.6268	1.2440	0.6258	1.2442	0.6272	1.2410
752510	0.6265	1.2160	0.6257	1.2172	0.6271	1.2150
755010	0.6296	1.2336	0.6292	1.2330	0.6307	1.2302
757510	0.6336	1.2497	0.6331	1.2478	0.6343	1.2451
σ (nm)			0.0009	0.0021	0.0009	0.0030

Table 6.9 Experimental values and Moon et al and Glisson et al predicted values of the a and c lattice parameter for compositions in the interior of the tellurium face ($z = 1.0$). The standard deviation, σ, for the Moon and Glisson interpolation equations are also given.

indicated by the standard deviations in Tables 6.4 - 6.9 and the tellurium curves in figure 6.3, both the Moon and Glisson equations fit the experimental data within the limits of experimental error. The difference between the two formulations is limited since the bowing is small for all variations of the lattice parameter with composition. As discussed in section 6.2 the difference between the two interpolation methods is associated with the manner in which the bowing parameter Q, enters each formulation.

It was not possible to obtain accurate C values for the energy gap analysis since data along the edges was incomplete and less accurate than the lattice parameter data. Thus, in order to test the interpolation equations for energy gaps, a fit was done to all the points on the copper and indium faces, except at the four corner compositions. This was done assuming the B parameters known, and the C's were determined by the least squares method indicated in the appendix. The B parameters used in the analysis of the copper and indium energy gap values are listed below in Table 6.10. The energy gap

B_i	Compound	Energy Gap (eV)
B_1	$CuGaSe_2$	1.51
B_3	$AgInSe_2$	1.110
B_4	$CuInSe_2$	0.954
B_5	$CuGaTe_2$	1.25*
B_7	$AgInTe_2$	0.938
B_8	$CuInTe_2$	0.928

Table 6.10 B parameters used in the analysis of the copper and indium energy gap values.

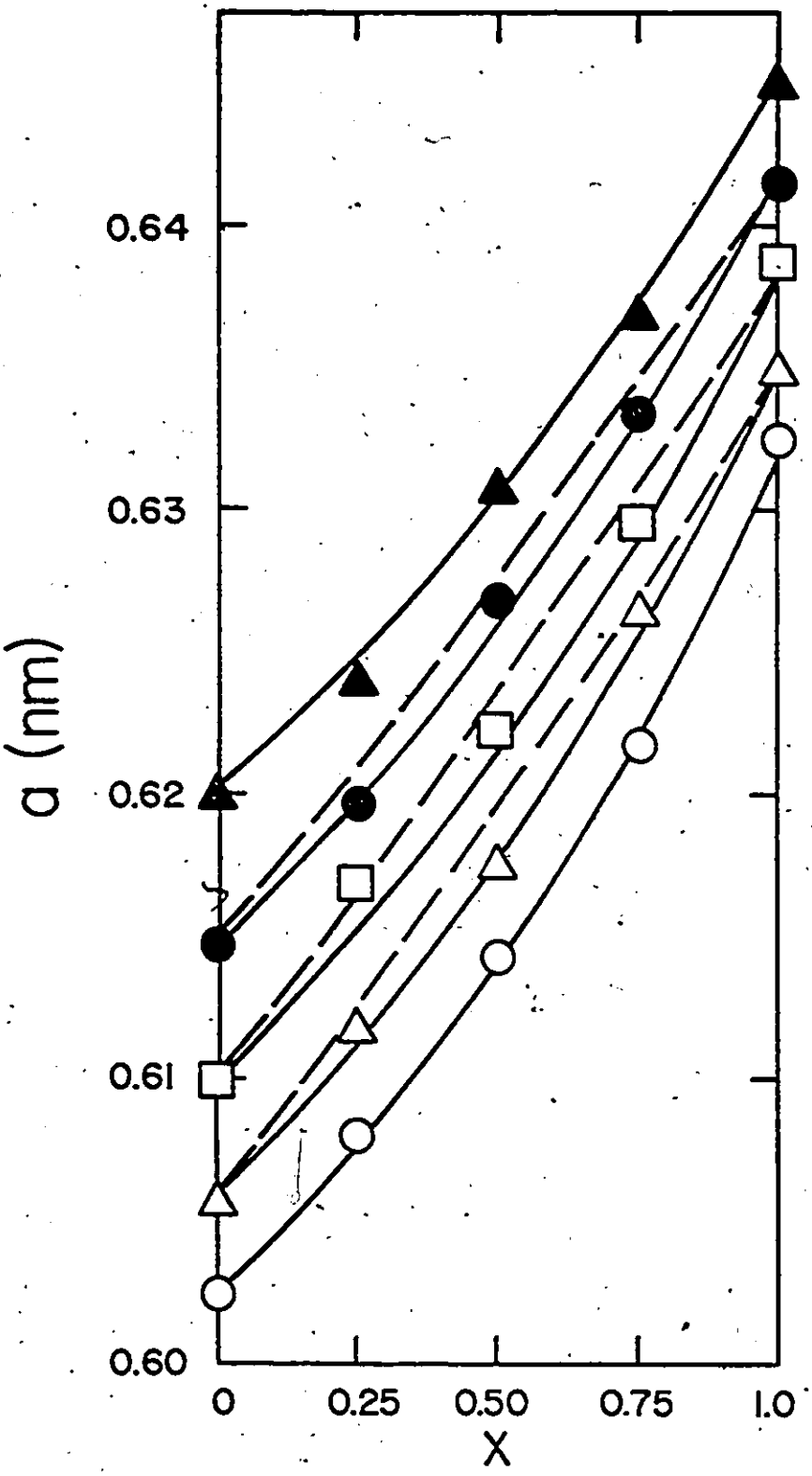

Figure 6.3(a) Variation of lattice parameter a for the Te face as a function of x at various constant values of y. Solid curves correspond to the variation predicted by the Moon et al interpolation equation. Dashed curves correspond to the variations predicted by the Glisson et al interpolation equation.
y = 0 ○ , y = 0.25 △ , y = 0.50 □ , y = 0.75 ● , y = 1.0 ▲

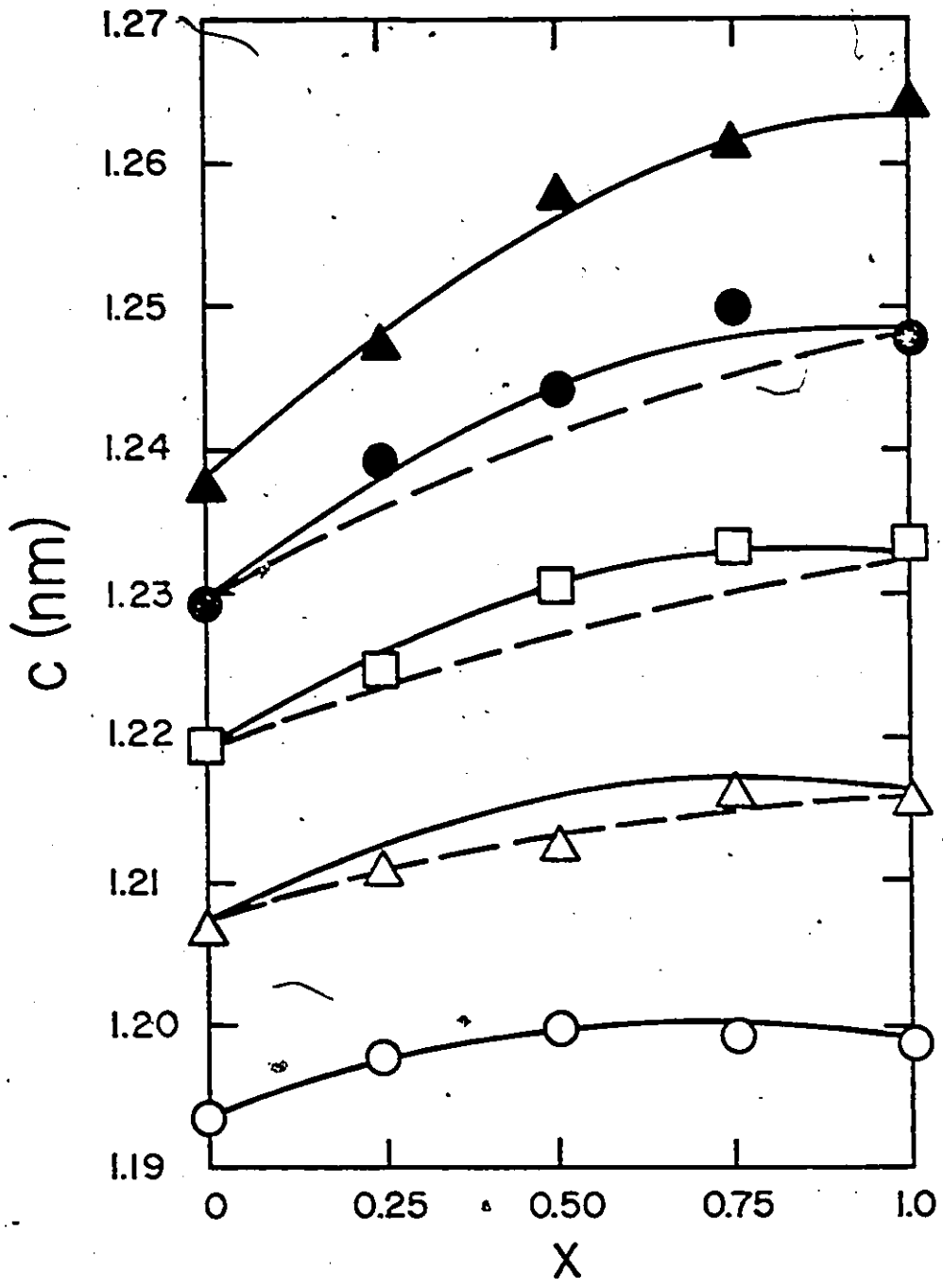

Figure 6.3(b) Variation of lattice patameter c for the Te face as a function of x at various constant values of y. Solid curves correspond to the variation predicted by the Moon et al equation. Dashed curves correspond to the variation predicted by the Glisson et al interpolation equation.
y = 0 ○, y = 0.25 △, y = 0.50 □, y = 0.75 ●, y = 1.0 ▲

indicated with an asterisk was taken from the literature (79P1).

The C parameter values obtained for the Glisson and Moon equations are given in Table 6.11 for the copper face and in Table 6.12 for the indium face. Also listed in these tables are the C parameters that could be determined using the edge fitting method used for the lattice parameters. The standard deviation between the experimental points on the faces, (excluding the four corner points) and the values predicted by the Moon & Glisson formulations using the data listed in Table 6.10 and the calculated C parameters, are also given. Tables 6.13 and 6.14 compare the experimental energy gap values and the Moon and Glisson values. These are plotted for the copper face in figure 6.4.

C_{ij}	Moon Fit	Glisson Fit	Edge Fit
C_{14}	0.017	0.141	-0.046
C_{58}	0.115	0.584	no value
C_{15}	0.317	0.460	0.298
C_{48}	0.427	0.515	0.392
σ (eV)	0.015	0.030	

Table 6.11 C parameters determined by fitting to the Moon and Glisson interpolation equations for energy gap values on the copper face. Also indicated are the standard deviations, σ, and, when possible the C's obtained by fitting the edge values.

C_{ij}	Moon fit	Glisson fit	Edge Fit
C_{14}	0.142	0.356	0.123
C_{58}	0.070	0.243	0.003
C_{15}	0.426	0.574	0.392
C_{48}	0.361	0.582	0.331
σ (eV)	0.018	0.043	

Table 6.12 C parameters determined by fitting to the Moon and Glisson interpolation equations for energy gap values on the indium face. Also indicated are the standard deviations, σ, and the C's obtained by fitting the edge values.

Although deviations from the Moon and Glisson fits are within the limits of experimental error for the lattice parameter, the bowing is larger for energy gaps and the difference between the two formulations is accentuated. As seen through the standard deviation and comparison of the Moon and Glisson C values to those obtained by fitting to the edges, the Moon equation gives consistently better results. The Moon fit is good for both the copper and indium faces whereas the Glisson fit is much worse for the indium face characterized by the minimum in E_g in its interior.

Composition	Experimental	Moon	Glisson
000025	1.395	1.384	1.357
000075	1.264	1.253	1.226
002500	1.384	1.367	1.344
002525	1.230	1.247	1.252
002550	1.178	1.170	1.172
005000	1.239	1.227	1.196
005025	1.088	1.115	1.120
005050	1.044	1.050	1.053
005075	1.040	1.031	1.017
007500	1.106	1.090	1.066
007525	0.977	0.989	1.001
007550	0.926	0.938	0.949
007575	0.957	0.937	0.938
001025	0.854	0.868	0.851
001050	0.846	0.834	0.812
001075	0.875	0.855	0.838

Table 6.13 Energy gap values (eV) for the copper face determined experimentally, and using the Moon and Glisson equations obtained by fitting to the C parameters.

Composition	Experimental	Moon	Glisson
001025	0.854	0.868	0.840
001050	0.846	0.835	0.797
001075	0.875	0.855	0.826
251000	0.966	0.966	0.926
251025	0.859	0.877	0.893
251075	0.870	0.852	0.867
251010	0.927	0.917	0.885
501000	1.032	0.996	0.943
501025	0.898	0.902	0.914
501050	0.845	0.858	0.873
501075	0.859	0.862	0.872
501010	0.916	0.915	0.872
751025	0.912	0.943	0.952
751050	0.893	0.889	0.896
751075	0.872	0.882	0.890
751010	0.930	0.922	0.890
101025	1.040	0.999	0.958
101050	0.933	0.934	0.878

Table 6.14 Energy gap values (eV) for the indium face determined experimentally, and using the Moon and Glisson equations obtained by fitting to the C parameters.

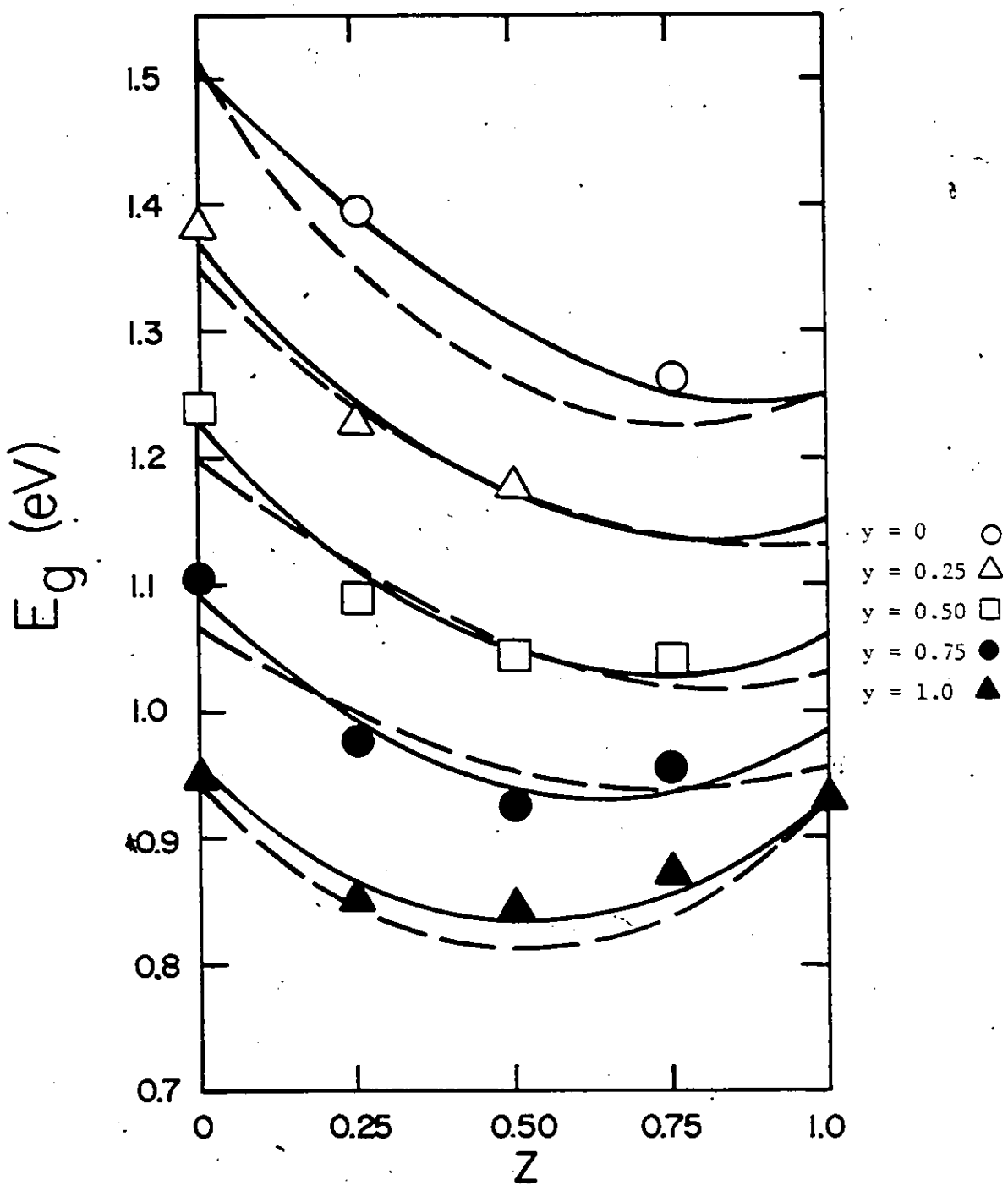

Figure 6.4 Variation of energy gap, E_g, for the Cu face as a function of z at various constant values of y. Solid curves correspond to the variations predicted by the Moon et al equation. Dashed curves correspond to the variations predicted by the Glisson et al interpolation equation.

6.5 Application of the Three Dimensional Analysis Developed from the Moon et al Interpolation Equations

Using the three-dimensional interpolation equation (6.21) and the values of the B and C parameters listed in Tables 6.2 and 6.1 respectively, values of the lattice parameter a were predicted for compositions in the interior of the cube. The same procedure was followed for the c lattice parameter using the B' and C' parameters given in Tables 6.3 and 6.1 respectively. All data predicted in this way is shown in Table 6.15 and is compared to the appropriate experimental values. Graphs have been plotted showing the experimental points and curves predicted from the three dimensional analysis extended from the Moon formulation. These are shown for the $x = 0.25$, $y = 0.75$, and $z = 0.75$ planes in figures 4.15, 4.16, and 4.17 respectively by the dashed line and can be compared to the 26 parameter power series fit indicated by the solid line on the same figures. From these figures it can be seen that the accuracy of the prediction appears to be about the same as in the case of the 26 term average parameter fit. This can also be seen by comparison of the standard deviation of the predicted points corresponding to each analysis. For the power series fit to the interior points $\sigma = 0.0029$nm and $\sigma = 0.0059$nm for the lattice parameters a and c respectively. These figures can be compared to $\sigma = 0.0028$ nm and $\sigma = 0.0046$nm corresponding to the a and c lattice parameters predicted from the three dimensional Moon analysis. Thus the a and c predictions for the interior points are equally good for the power series and extended Moon formulation, showing that the three-dimensional analysis is acceptable.

Composition	Experimental		3D Analysis	
	a(nm)	c(nm)	a(nm)	c(nm)
252525	0.5764	1.1338	0.5817	1.1412
252575	0.5973	1.1784	0.6005	1.1871
255025	0.5838	1.1514	0.5849	1.1573
255050	0.5938	1.1780	0.5939	1.1785
255075	0.6084	1.2144	0.6040	1.2015
257525	0.5859	1.1716	0.5885	1.1722
257550	0.6002	1.1965	0.5977	1.1924
257575	0.6139	1.2146	0.6080	1.2144
502575	0.6055	1.1857	0.6074	1.1874
505075	0.6112	1.2040	0.6106	1.2033
507525	0.5908	1.1706	0.5945	1.1741
507550	0.6054	1.1960	0.6041	1.1949
507575	0.6157	1.2191	0.6142	1.2183
752575	0.6153	1.1880	0.6156	1.1857
755050	0.6052	1.1743	0.6091	1.1761
755075	0.6189	1.2036	0.6185	1.2027
757550	0.6089	1.1909	0.6117	1.1941
757575	0.6224	1.2202	0.6216	1.2192
σ (nm)			0.0028	0.0046

Table 6.15 Experimental data and predicted lattice parameter values for interior compositions using the 3-dimensional extension of the Moon formulation.

The standard deviation of all the experimental points from the three-dimensional extension of the Moon formulation was calculated to be σ = 0.0016nm and σ = 0.0043nm for the a and c lattice parameters respectively. These figures can be compared to σ = 0.0015nm and σ = 0.0023nm for the a and c parameters respectively, determined similarly using the 26 term power series expression. The power series predictions are better, especially for the c parameter. This is expected since the power series expression was developed by fitting to all 6 faces, leaving only some 18 points to be predicted. In the Moon case, fits were made only to the cube edges to predict values on the faces and in the interior the cube.

6.6 Summary

Two separate interpolation equations to estimate the band gap and lattice parameter values for alloys of the general form $A_{1-x}B_xC_{1-y}D_y$ have been developed by Moon et al (74M1) and Glisson et al (78G1). These are given in terms of the values for the ternary compounds, ABC, ABD, etc., in equations (6.10) and (6.11) respectively. The two formulations differ by the manner in which a bowing parameter enters each analysis, the bowing being two times larger at the centre of the composition range in the Moon analysis.

The lattice parameter data was used to test these interpolation equations by comparing the experimental values in the interior of the faces to those predicted by Moon and Glisson. Both of the interpolation equations were found to give values within the limits of experimental error, with the bowing parameter being small for all variations of lattice parameter with composition.

For the energy gap analysis the interpolation equations (6.10) and (6.11) were used to fit all of the experimental data on the faces. Since the bowing is larger for the energy gaps, the difference between the two methods was greater, and the Moon fit gave consistently better results.

In order to fit the values of lattice parameter for alloys of the form $A_{1-x}B_xC_{1-y}D_y(E_{1-z}F_z)_2$, a three dimensional interpolation equation was developed from the Moon formulation. This is given by equation (6.21) and was used to predict values of the lattice parameter for compositions in the interior of the cube. Graphs were plotted showing the experimental points and predicted curves for the $x = 0.25$, $y = 0.75$, and $z = 0.75$ planes. The accuracy of the prediction was found to be the same as in the case of the 26 term average parameter fit done in Chapter IV. When all the points were considered together, however, the power series predictions were found to be more accurate.

CHAPTER VII – c/a RATIO AND ELECTRONEGATIVITY VALUES

7.1 Introduction

With ideal ordering, the chalcopyrite structure should have c/a = 2. However, interaction between the ordered cations and the anion sublattice causes the positions of the atoms to be changed to some extent from the ideal positions and this change results in tetragonal distortion which can be most easily observed in the deviation of the c/a ratio from 2. Thus, the value of $(2-c/a) = \Delta$ can be taken as a measure of this tetragonal distortion, and in almost all cases for chalcopyrite materials, $\Delta \geq 0$.

One of the factors which influence the tetragonal distortion is the electronegativity values of the atoms (75S1). Various attempts have been made to relate the values of Δ to the electronegativity values of the atoms in various I-III-VI_2 compounds. Thus Phillips (73P1) has proposed that for a I-III-VI_2 compound the relation

$$\Delta = -0.60X_A + 0.25X_B + 0.15X_C + 0.01 \qquad (7.1)$$

should apply, where X_A, X_B, and X_C are the electronegativity values of the I, III, and VI atoms respectively. However, Weaire and Noolandi (75W1) have indicated for a group of I-III-VI_2 compounds with a given A (i.e. I atom), Δ obeys the relation

$$\Delta \propto (X_A - X_B)^2. \qquad (7.2)$$

No analysis of this type has as yet been applied to alloys of these materials and so it is of interest to determine values of Δ for the

present alloy system and to use these to test equations (7.1) and (7.2).

7.2 c/a Ratios and Test of the Phillips and Weaire & Noolandi Equations

Various values of electronegativity have been proposed at different times but both Phillips and Weaire & Noolandi make use of the electronegativity values given by Phillips (73P2). Thus these values will be used here and are listed in Table 7.1.

Atom	Electronegativity
Cu	0.79
Ag	0.57
Ga	1.13
In	0.99
Se	1.79
Te	1.47

Table 7.1 Electronegativity values proposed by Phillips (73P2)

Since the Phillips equation contains X_C while the equation of Weaire and Noolandi does not, an initial analysis was carried out for the results of the tellurium and selenium faces since in each of these two sets, any contribution from the VI atoms might be expected to be constant. It is assumed that since the copper and silver atoms are at random on the I sublattice and the gallium and indium atoms are

at random on the III sublattice, it is reasonable to replace X_A by $(1 - x)X_{Cu} + xX_{Ag}$ and X_B by $(1 - y)X_{Ga} + yX_{In}$. When this is done, in the case of the Te face, the Phillips equation takes the form

$$\Delta = -0.60\{(1 - x)X_{Cu} + xX_{Ag}\} + 0.25\{(1 - y)X_{Ga} + yX_{In}\}$$

$$+ 0.15X_{Te} + 0.01 \qquad (7.3)$$

while the Weaire and Noolandi relation can be written as

$$\Delta = K^2\{(1 - x)X_{Cu} + xX_{Ag} - (1 - y)X_{Ga} - yX_{In}\}^2$$

$$= K^2\{X_{Cu} - X_{Ga} + x(X_{Ag} - X_{Cu}) - y(X_{In} - X_{Ga})\}^2$$

or

$$\Delta^{\frac{1}{2}} = \mu = P + Qx + Ry, \qquad (7.4)$$

where

$$P = K(X_{Cu} - X_{Ga}), \quad Q = K(X_{Ag} - X_{Cu}), \quad \text{and} \quad R = -K(X_{In} - X_{Ga}).$$

Graphs of Δ against x at constant y and against y at constant x were found to be definitely non-linear, indicating that the present results do not fit the Phillips equation (equation (7.3)). However, graphs $\Delta^{\frac{1}{2}}$ ($= \mu$) plotted in a similar fashion were good straight lines as is seen from figure 7.1. This indicates that equation (7.4) is satisfied by the present experimental data. Also, as is seen from the expression for Q and R, the lines in each set should be parallel and this is observed in the graphs.

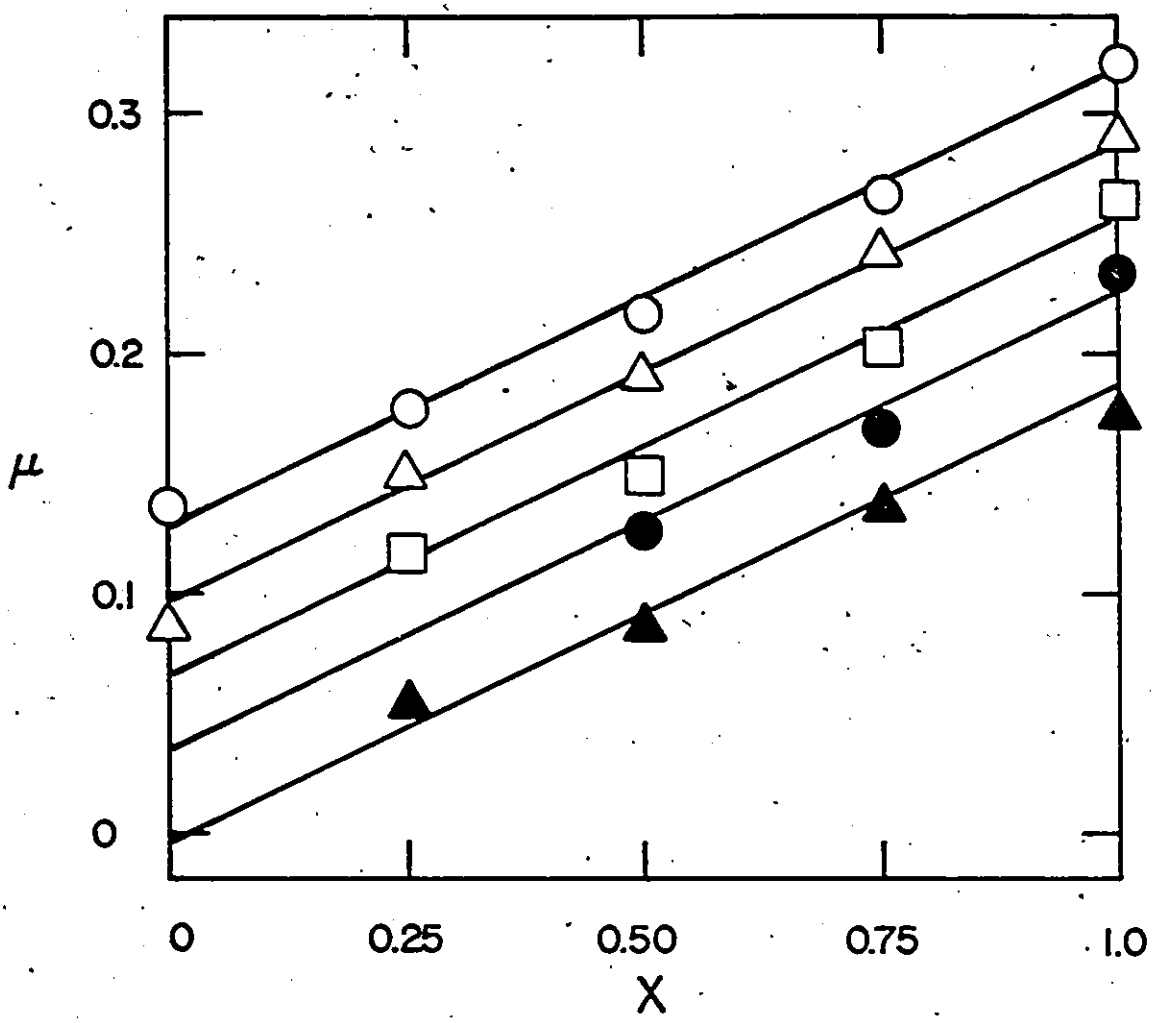

Figure 7.1(a) Variations of μ for the Te face as a function of x at various constant values of y.
y = 0 ○, y = 0.25 △, y = 0.50 □, y = 0.75 ●, y = 1.0 ▲

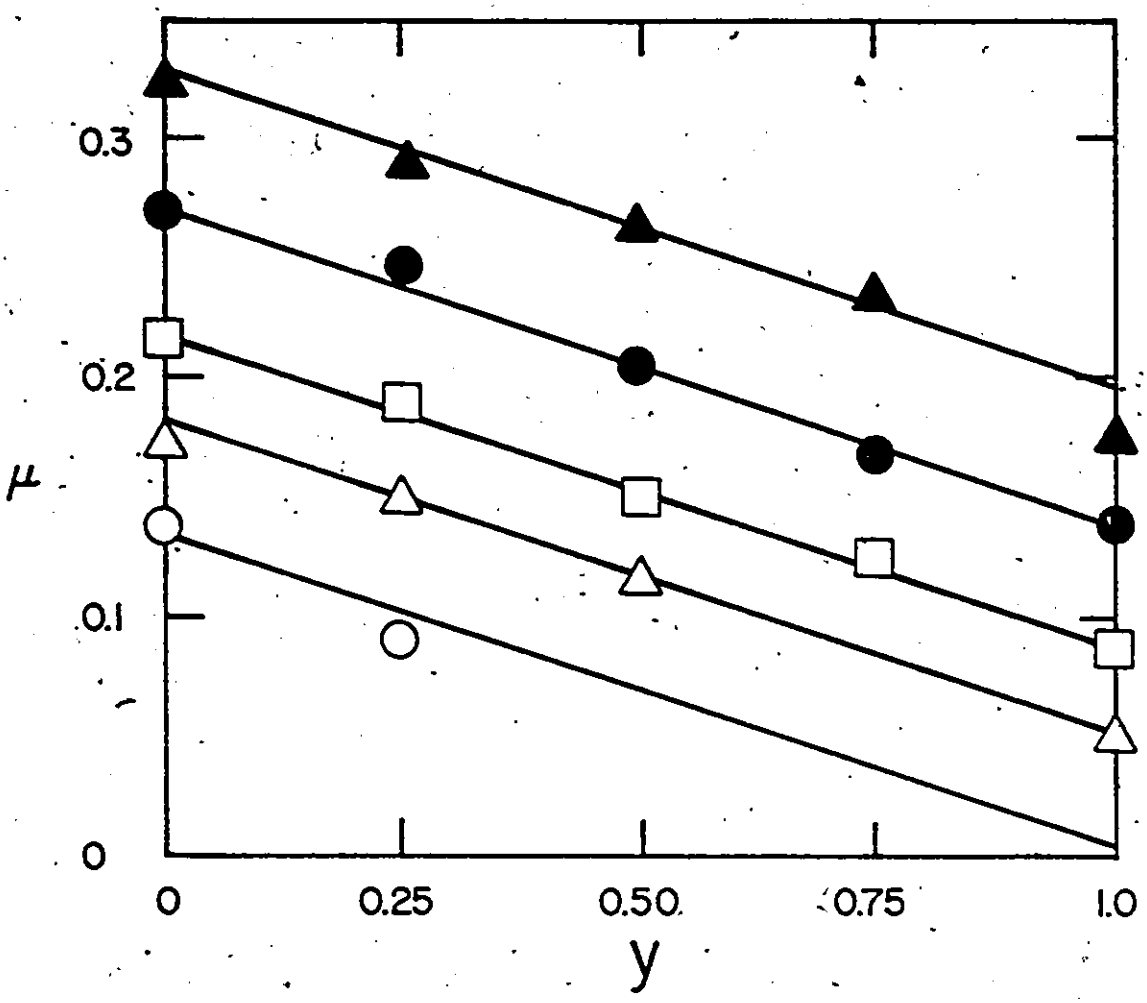

Figure 7.1(b) Variations of μ for the Te face as a function of y at various constant values of x.
x = 0 ○, x = 0.25 △, x = 0.50 □, x = 0.75 ●, x = 1.0 ▲

The value of K is not known, but from equation (7.4), the ratios of the coefficients, e.g. Q/R etc., should be related to the electronegativity values given in Table 7.1. All the values of μ for the Te face were fitted to equation (7.4) using the usual least squares fit (see appendix) and values obtained for the parameters viz. P = 0.178, Q = 0.205, and R = -0.130. Thus the ratio of -Q/R = 1.58 in this case.

A similar analysis was carried out for all of the points of the Se face and the resulting parameter values were P = 0.178, Q = 0.260, and R = -0.167 giving -Q/R = 1.55.

From the definitions of Q and R,

$$-\frac{Q}{R} = \frac{X_{Ag} - X_{Cu}}{X_{In} - X_{Ga}}$$

and using values of Phillips electronegativity in Table 7.1 this gives -Q/R = 1.57 which is in very good agreement with the values determined above from the present experimental data.

However if ratios involving P are considered, the agreement is less satisfactory. For the Te face, the experimental value of Q/P is 1.75 while that for the Se face is 1.45. In comparison,

$$\frac{Q}{P} = \frac{X_{Ag} - X_{Cu}}{X_{Cu} - X_{Ga}} = 0.65$$

from the Phillips values in Table 7.1. But as was indicated by Phillips (73P1), the effect of the VI atoms should not be zero as is implied by equations (7.2) and (7.4). Thus, in the cases of both the Te face and Se face, there may be a constant contribution from X_{Te} or X_{Se} and this would affect the value of P in the analysis.

In an attempt to allow for the effect of the VI atom, equation (7.2) has been modified to

$$\Delta = \mu^2 = K^2(X_A - X_B + qX_c)^2 \qquad (7.5)$$

where q is a fractional value to be determined. In the case of the Te face, this leads to

$$\mu = K\,(X_{Cu} - X_{Ga} + qX_{Te}) + x(X_{Ag} - X_{Cu}) - y(X_{In} - X_{Ga}) \qquad (7.6)$$

i.e. P now has the value $K(X_{Cu} - X_{Ga} + qX_{Te})$

and

$$\frac{Q}{P} = \frac{X_{Ag} - X_{Cu}}{X_{Cu} - X_{Ga} + qX_{Te}}$$

Using the experimental value of Q/P = 1.75 and the Phillips values of Table 7.1, this gives q = 0.14. A similar use of the values for the Se face gives q = 0.11. Thus the data for the Te and Se faces can be reasonably well fitted by equation (7.6) if a value of q of the order 0.1 is assumed. It is to be noted from equation (7.1) that Phillips proposed a lesser contribution from the Te and Se atoms than from the others in the compounds.

This analysis can now be extended to the other faces of the cube and to the alloys inside the cube by replacing equation (7.4) by

$$\mu = K\,\{(1 - x)X_{Cu} + xX_{Ag} - (1 - y)X_{Ga} - yX_{In} + q(1 - z)X_{Se} + qzX_{Te}\}$$

$$= K\{X_{Cu} - X_{Ga} + qX_{Se} + x(X_{Ag} - X_{Cu}) - y(X_{In} - X_{Ga}) + qz(X_{Te} - X_{Se})\} \qquad (7.7)$$

$$= P + Qx + Ry + Sz$$

where

$$P = K(X_{Cu} - X_{Ga} + qX_{Se}), \quad Q = K(X_{Ag} - X_{Cu}), \tag{7.8}$$

$$R = -K(X_{In} - X_{Ga}), \quad \text{and} \quad S = qK(X_{Te} - X_{Se}).$$

If the four other faces are considered separately the appropriate equations become

Cu face ($x = 0$)	$\mu = P + Ry + Sz$	(7.9)
Ag face ($x = 1$)	$\mu = (P + Q) + Ry + Sz$	(7.10)
Ga face ($y = 0$)	$\mu = P + Qx + Sz$	(7.11)
In face ($y = 1$)	$\mu = (P + R) + Qx + Sz.$	(7.12)

For each face, the experimental values were fitted by a least squares fit and parameter values determined. These are listed below.

Cu face	$P = 0.179$	$R = -0.137$	$S = -0.046$
Ag face	$(P + Q) = 0.422$	$R = -0.131$	$S = -0.093$
Ga face	$P = 0.190$	$Q = 0.237$	$S = -0.073$
In face	$(P + R) = 0.051$	$Q = 0.203$	$S = -0.063$

Considering first the values of P, Q, and R, these are quite consistent within the limits of experimental error. If equations (7.8) to (7.12) are used with the values of X in Table 7.1, ratios involving P, Q and R but not S for the various faces can be used to give values of q. The values obtained are given in Table 7.2.

face	q
Cu	0.09
Ag	0.06
Ga	0.09
In	0.08

Table 7.2 Values of q for the Cu, Ag, Ga, and In faces calculated using the Phillips electronegativities.

These values again indicate that a reasonable fit to the experimental data needs a value of q of the order 0.1.

Turning to the values of S determined above, it is seen that there is rough agreement between these, and that they are all negative. However, it is found that if these negative values are used in ratios with P, Q, or R, in each case negative values of q are obtained. Thus the values determined from S, the coefficient of z in equation (7.7), appear to be anomolous. One explanation that can be suggested is that q is not constant but differs somewhat from one VI element to another. If this were the case then q itself would be a function of z and in equation (7.7) this would have a small effect on the parameter P but could greatly affect the value of S. Also, for the analyses of the separate Te and Se faces, z would be constant in each case so that the positive values of q given above, in those cases, would appear to be the valid ones. However, a more detailed analysis making q a function of z would not be justified with the present experimental data.

One parameter not considered so far is K. Weaire and Noolandi indicate that this parameter may depend to some extent on the elements present in the compound considered, but give no final form for K. In the above analysis, since q occurs only in the expressions for P and S, values of K can be determined by using the experimental values of Q and R with the X values of Table 7.1. The values of K so obtained are given in Table 7.3.

face	K
Cu	-0.98
Ag	-0.94
Ga	-1.07
In	-0.92
Se	-1.19
Te	-0.93

Table 7.3 Values of K for all faces of the cube determined from experimental values of Q and R and the Phillips electronegativities.

(The negative sign for the K values is of no significance, since equation (7.6) is the square root of equation (7.5) and either sign could be taken). These values seem to indicate that the elements of larger electronegativity give larger values of K.

If equation (7.5) is applied to all of the available experimental data, the fit is only an approximate one and mean

values of q and K are obtained. However since the variations of q and K with composition do not appear to be very large, it is perhaps useful to obtain these mean values. Equation (7.7) can be written in the form

$$\mu = K\{(1-x)X_{Cu} + xX_{Ag} - (1-y)X_{Ga} - yX_{In}\} + Kq\{(1-z)X_{Se} + zX_{Te}\}$$

i.e. $$\mu = K\alpha + Kq\beta \qquad (7.13)$$

where for each sample α and β can be determined from values in Table 7.1. Equation (7.13) was fitted to all the 102 alloys values which had been considered to be single phase, and values of K and Kq determined by a least squares fit (appendix). The resulting values are K = 0.90 and q = 0.105.

7.3 Summary

Separate equations have been proposed by Phillips (73P1) and Weaire and Noolandi (75W1) to relate the tetragonal distortion, $\Delta = 2 - \frac{c}{a}$, to the electronegativity values in various I-III-VI_2, compounds. The relationship proposed by Phillips gives Δ as a linear function of all the electronegativities, whereas the Weaire and Noolandi equation shows $\Delta^{\frac{1}{2}}$ proportional to the electronegativities of the I and III atoms only.

Graphs of Δ against x at constant y and against y at constant x were plotted for the tellurium face and were found to be non-linear. Graphs of $\Delta^{\frac{1}{2}}$ plotted similarly were found to give good, straight, parallel lines. This indicates that the Weaire and Noolandi

proposal is satisfied by the present experimental data.

With μ defined as $\mu = \Delta^{\frac{1}{2}}$, all the values of μ for the Te and Se faces were fitted to the Weaire and Noolandi equation. The parameters, P, Q, and R, functions of the electronegativities of the atoms and some constant, K, only, were determined for each face from the fitting. (P, Q, and R are defined in equation (7.4)). A ratio of the Q and R parameters, thus obtained were compared to a Q/R value determined only from the electronegativities of the atoms. These ratios were found to agree quite well for both the Te and Se face. Similarly, the ratio of the Q and P parameters was also calculated for each of the Se and Te faces. These were found to be quite different from the values calculated from the electronegativities of the atoms since the effect of the VI atom is not zero as suggested by Noolandi and Weaire.

The Weaire and Noolandi equation was modified in order to allow for the effects of the VI atom by making $\Delta^{\frac{1}{2}}$ a function of some fractional value, q, of the VI atom electronegativities. The data for the Te and Se faces was found to fit reasonably well to the new equation if a value of q of the order of 0.1 was assumed. The experimental data for each of the faces was fitted to the modified equation and the parameters determined in each case. These were found to be consistent within the limits of experimental error.

Values of the constant K in the modified Weaire et al equation were determined using the experimental values of Q and R with the electronegativities for each face. The resulting K values seem to indicate that elements of larger electronegativity give larger values of K. Average values of q and K were obtained by applying the new equation to all of the available experimental data. The resulting values are K = 0.90 and q = 0.105.

APPENDIX

Least Squares Fit to N Parameters

The various equations which had to be fitted to the experimental points could, in every case, be reduced to a power series of the form

$$Aa + Bb + Cc + Dd + Ee + \ldots = t, \qquad (A.1)$$

where a, b, c, etc. and t are variables characteristic of a given alloy sample and are functions of the composition variables x, y, and z. A, B, C, etc. are coefficients to be determined under the conditions that the number of available experimental points, n, is greater than the number of variables, N. One standard method of least squares fitting to determine the coefficients is as follows.

A set of equations is obtained by multiplying equation (A.1) by each of the variables, a, b, c, etc., and in turn summing each of the resulting equations over all of the experimental points. This gives equations of the form

$$\begin{aligned} A\Sigma a^2 + B\Sigma ab + C\Sigma ac + \ldots &= \Sigma at \\ A\Sigma ba + B\Sigma b^2 + C\Sigma bc + \ldots &= \Sigma bt \\ A\Sigma ca + B\Sigma cb + C\Sigma c^2 + \ldots &= \Sigma ct \end{aligned} \qquad (A.2)$$

Values of the coefficients A, B, C, etc. can be obtained by simultaneously solving the N equations (A.2). When $N \leq 3$, this gives a simple form which can easily be calculated. In the present work the largest value of N used is N = 9, and in this case standard computer programs are available to evaluate the determinant involved.

REFERENCES

45N1 Nelson, J.B., and Riley, D.P., 1945a, Proc. Phys. Soc., 57, 160; 1945b, Proc. Phys. Soc., 57, 477.

64P1 Pamplin, B.R., J. Phys. and Chem. Solids, 25, 675 (1964).

67J1 Johnson, E.J., Semiconductors and Semimetals, Vol. 3. Edited by Willardson, R.K., and Beer, A.C., Academic Press, New York, (1967), p. 153.

67T1 Thompson, A.G., and Woolley, J.C., Can. J. Phys. 45, 255 (1967).

73P1 Phillips, J.C., J. Phys. Chem. Solids, 35, 1205 (1974).

73P2 Phillips, J.C., Bonds and Bands in Semiconductors, Academic Press, p. 54 (1973).

73P3 Parker, J.G., Appl. Opt., 12, 2974 (1973).

73R1 Robbins, M. and Lambrecht, V.G., Jr., J. Solid State Chem. 6, 402 (1973).

73R2 Robbins, M., Phillips, J.C., and Lambrecht, V.G., Jr., J. Phys. Chem. Solids, 34, 405 (1973).

74M1 Moon, R.L., Antypas, G.A., and James, L.W., J. Electronic Mat., 3, No. 3, 635 (1974).

74P1 Phillips, J.C., J. Phys. Chem. Solids, 35, 1205 (1974).

75S1 Shay and Wernick, Ternary Chalcopyrite Semiconductors: Growth, Electronic Properties and Applications, Pergamon, New York (1975).

75W1 Weaire, D. and Noolandi, J., Journal de Physique, 36, C3-27 (1975).

76B1 Bennet, H.S. and Forman, R.A., Appl. Opt., 15, 2405 (1976).

77A1 Aamodt, L.C., Murphys, J.C., and Parker, J.G., J. Appl. Phys., 48, 927 (1977).

77W1 Wetsel, G.C., Jr. and McDonald, F.A., Appl. Phys. Lett., 30, 252 (1977).

77W2 Wetsel, G.C., Jr. and McDonald, F.A., Bull. Am. Phys. Soc., 22; 295 (1977).

78G1 Glisson, T.H., Hauser, J.R., Littlejohn, M.A., Williams, C.K., J. Electronic Mat., 7, No. 1 (1978).

79C1 Chapman, G.H., Shewchun, J., Loferski, J.J., Garside, B.K., and Beaulieu, R., Sol. Energy Mat., 1, 451 (1979).

79C2 Chapman, G.H., Shewchun, J., Loferski, J.J., Garside, B.K., and Beaulieu, R., Appl. Phys. Lett., 34, 735 (1979).

79P1 Pamplin, B.R., Kiyosawa, T., and Masumoto, K., Prog. Cryst. Growth and Charact., 1, 331 (1979).

80R1 Rosencwaig, A., Photoacoustics and Photoacoustic Spectroscopy, John Wiley and Sons, New York, (1980).

80S1 Shah, J.S., Prog. Cryst. Growth and Charact. 3, 333 (1980).

81A1 Avon, J.E., Woolley, J.C., Asbjornsen, A., Chatraphorn, S., Ratanathammapan, K., and Yoodee, K., J. Appl. Phys. 52, 6423 (1981).

82G1 Goodchild, R.G., Hughes, O.H., Lopez-Rivera, S.A., Woolley, J.C., Can. J. Phys., 60, 1096 (1982).

ABSTRACT

Polycrystalline samples of the alloy system $(Cu_{1-x}Ag_x)(Ga_{1-y}In_y)(Se_{1-z}Te_z)_2$ were prepared from the elements by the standard melt and anneal technique. A total of 125 different alloy compositions having values of x, y, and z of 0, 0.25, 0.50, 0.75, and 1.0 were made. Debye-Scherrer x-ray powder photographs were obtained for each of the alloys to check for homogenenity and the range of solid solution. Single phase solid solution was found throughout the Cu (x = 0), In (x = 1), and Te (z = 1) faces of the cubic composition range. The Ga (y = 0), Ag (x = 1) and Se (z = 0) faces, were found to show some multiphase behavior.

X-ray powder photographs were analyzed in order to determine values of the lattice parameters, a and c, and these were plotted as a function of composition for each face. Fitting was done using a nine term power series expression and the resulting equations were used to draw contours of constant a and c. In a general three-dimensional analysis, the power series fits to each face were used to determine the coefficients of a 26 term power series using an averaging method. The accuracy of the resulting equation was checked by predicting lattice parameter values throughout the entire composition range and calculating the standard deviation of the predicted values from the experimental values.

Energy gap values, E_g, were investigated using either absorption or photoacoustic techniques for all samples found to be single phase. Measurements were not always successful, complete energy gap data being determined for the Cu and In faces only. Values of E_g for these faces were plotted as a function of composition and fitted to a

power series expression. Contours of constant E_g were drawn.

Nearly complete E_g data was obtained for the $x = 0.25$ and $z = 0.75$ planes. These values were plotted as a function of the variables z and x for the $x = 0.25$ and $z = 0.75$ planes respectively. Curves of constant y were fitted to parabolic form.

Two separate interpolation equations estimating the band gap and lattice parameter values in two-variable systems of alloys were tested using the data from the faces. Both equations gave values within the limits of experimental error for the lattice parameter. For energy gap data, one equation gave consistently better results. This equation was used to develop a three-dimensional model to predict lattice parameter values in the interior of the cube. The accuracy of the predictions was found to be comparible to that of the 26 term power series expression.

The tetragonal distortion, $\Delta = 2 - c/a$, was calculated for each of the alloys. Various relationships having been proposed relating Δ to the electronegativities of the atoms, were checked using the present experimental data. The equations were modified in order to obtain better agreement between experimental values and the predicted values. Fitting was done to each face separately and to all compositions together in order to obtain unknown parameter values in the modified equation.

UNIVERSITÉ D'OTTAWA
UNIVERSITY OF OTTAWA